
VULNERABILITY OF SPACE STATION FREEDOM MODULES-
A Study of the Effects of Module Perforation on Crew &
Equipment

Volume I - Experimental Program

By : J. Serrano, D. Gala, D.J. Liquornik & R. A. Hayami
University of Alabama in Huntsville
and
Joel Williamsen,
Structural Development Branch
NASA, Marshall Space Flight Center
Huntsville AL

Final Report, Vol. I: Contract NCC8-28
Period 09 September 1993 - 14 March 1995

Prepared for: NASA Marshall Space Flight Center
Huntsville, AL 35812



UNIVERSITY OF ALABAMA IN HUNTSVILLE
AEROPHYSICS RESEARCH CENTER
P.O. BOX 999, HUNTSVILLE, AL 35899

TABLE OF CONTENTS

SECTION	DESCRIPTION	PAGE NO.
1.0	INTRODUCTION	1
2.0	REPORT FORMAT	1
3.0	EXPERIMENTAL SET-UP	1
3.1	Facility	1
3.2	Target Chamber	2
3.3	Test Conditions	2
3.4	Instrumentation Set-up	2
3.5	Data Acquisition	7
3.6	Spacecraft Shield Targets	7
4.0	TEST RESULTS AND OBSERVATIONS	9
4.1	Test Results	9
4.2	Environmental Effects on Crew	16
5.0	CONCLUSIONS	18
6.0	REFERENCES	18
	APPENDICES	19

LIST OF ILLUSTRATIONS

Figure No.	Description	Page No.
Figure 1	Photograph of the UAH 108 mm Gun Test Chamber used in this Test Series	3
Figure 2	Photographic View of Impact Chamber Interior Without Equipment Rack Simulant	4
Figure 3	Photographic View of Impact Chamber Interior With Equipment Rack Simulant	4
Figure 4	Cross Sectional Top Down View of the Test Chamber - Without Equipment Racks	5
Figure 5	Cross Sectional Top Down View of the Test Chamber - With Equipment Racks	6
Figure 6	Photograph of the Digital Data Acquisition System	6
Figure 7	Sketch of the Three Types of Space Craft Shields Targets used in the Test Series	7
Figure 8a	Photographs of the Target Chamber for Test 5 Viewing Toward the Shield Target	8
Figure 8b	Photographs of the Target Chamber for Test 5 Viewing Away From the Shield Target	8
Figure 9	Typical Overpressure Profile at Sensor Position 1 (No Internal Equipment Simulant)	13
Figure 10	Typical Overpressure Profile at Sensor Position 3 (No Internal Equipment Simulant)	13
Figure 11	Typical Temperature Profile at Position 1 (No Internal Equipment Simulant)	14
Figure 12	Typical Temperature Profile at Position 3 (No Internal Equipment Simulant)	14
Figure 13	Typical Witness Plate Motion as Measured	15

LIST OF ILLUSTRATIONS (CONT.)
APPENDIX A

Figure no.	Description	Page No.
Figure A1	Target Plate Photographs - Test #1	A1
Figure A2	Pressure Profiles - Test #1	A2
Figure A3	Temperature Profiles - Test #1	A3
Figure A4	Radiometric Data - Test #1	A4
Figure A5	Target Plate Photographs - Test #2	A5
Figure A6	Pressure Profiles - Test #2	A6
Figure A7	Temperature Profiles - Test #2	A7
Figure A8	Target Plate Photographs - Test #3	A8
Figure A9	Pressure Profiles - Test #3	A9
Figure A10	Temperature Profiles - Test #3	A10
Figure A11	Radiometric Data - Test #3	A11
Figure A12	Target Plate Photographs - Test #5	A12
Figure A13	Pressure Profiles - Test #5	A13
Figure A14	Temperature Profiles - Test #5	A14
Figure A15	Radiometric Data - Test #5	A15
Figure A16	Target Plate Photographs - Test #6	A16
Figure A17	Pressure Profiles - Test #6	A17
Figure A18	Temperature Profiles - Test #6	A18
Figure A19	Radiometric Data - Test #6	A19
Figure A20	Target Plate Photographs - Test #8	A20
Figure A21	Pressure Profiles - Test #8	A21
Figure A22	Temperature Profiles - Test #8	A22
Figure A23	Radiometric Data - Test #8	A23
Figure A24	Target Plate Photographs - Test #9	A24
Figure A25	Pressure Profiles - Test #9	A25
Figure A26	Temperature Profiles - Test #9	A26
Figure A27	Radiometric Data - Test #9	A27
Figure A28	Target Plate Photographs - Test #10	A28
Figure A29	Pressure Profiles - Test #10	A29
Figure A30	Temperature Profiles - Test #10	A30
Figure A31	Radiometric Data - Test #10	A31
Figure A32	Target Plate Photographs - Test #11	A32
Figure A33	Pressure Profiles - Test #11	A33
Figure A34	Temperature Profiles - Test #11	A34
Figure A35	Radiometric Data - Test #11	A35
Figure A36	Target Plate Photographs - Test #13	A36
Figure A37	Pressure Profiles - Test #13	A37
Figure A38	Temperature Profiles - Test #13	A38
Figure A39	Pressure Plate Deflection Measurement	A39

APPENDIX B

Figure no.	Description	Page No.
Figure B1	X-Ray Photograph Particle Size Calibration	B1
Figure B2	X-ray Photograph of Debris Cloud, Test #01 X-Ray #1	B2
Figure B3	X-ray Photograph of Debris Cloud, Test #01 X-Ray #2	B3
Figure B4	X-ray Photograph of Debris Cloud, Test #03 X-Ray #1	B4
Figure B5	X-ray Photograph of Debris Cloud, Test #05 X-Ray #1	B5
Figure B6	X-ray Photograph of Debris Cloud, Test #06 X-Ray #1	B6
Figure B7	X-ray Photograph of Debris Cloud, Test #09 X-Ray #1	B7
Figure B8	X-ray Photograph of Debris Cloud, Test #10 X-Ray #1	B8
Figure B9	X-ray Photograph of Debris Cloud, Test #11 X-Ray #1	B9
Figure B10	X-ray Photograph of Debris Cloud, Test #13 X-Ray #1	B10

APPENDIX C

Distribution List	C1
-------------------	----

LIST OF TABLES

TABLE NO.	DESCRIPTION	PAGE NO.
1	Over Pressure Results	10
2	Temperature Test Results	11
3	Radiometric & Hole Results	12

PREFACE

The effort described in this report was supported by the Structural Development Branch, NASA Marshall Space Flight Center, Huntsville AL. The Contracting Officer's Technical Representative for this program was Dr. Joel Williamsen. The experimental work was performed at the Aerophysics Research Center of the University of Alabama in Huntsville AL.

This report which covers the experimental aspect of the effort performed on this program is titled "Vulnerability of Space Station Freedom Modules- A Study of the Penetration Effects on Crew & Equipment Volume I , Experiment ". A report under separate cover describing the analysis of the environmental effects of the module penetration on crew survival titled ""Vulnerability of Space Station Freedom Modules- A Study of the Penetration Effects on Crew & Equipment Volume II, Analysis" is being prepared by Dr. Wm. Schonberg of the Civil and Environmental Engineering Department of the University of Alabama in Huntsville.

ABSTRACT

Orbital debris penetration of manned spacecraft is accompanied by a number of atmospheric effects that can pose a serious hazard to spacecraft and crew survival. These atmospheric effects can include overpressure, light flash and temperature rise as hot particles from the penetration process impinge into the atmosphere of a manned spacecraft. This paper reports the results from a series of tests sponsored by the Marshall Space Flight Center and recently completed at the University of Alabama in Huntsville Aerophysics Research Center to study these effects.

In these tests, a light gas gun was used to fire orbital debris particle simulants from 0.375" to 0.625" in diameter through target simulants into a large test chamber simulating the interior cabin of a spacecraft at 1 atmosphere. The test chamber was instrumented with pressure transducers, light sensors, and temperature gauges to measure the level of blast hazard associated with differing target and penetrator conditions at various distances from the target site. The mitigating effects of interior equipment racks and spall blankets were also measured. This report discusses the relationship between observed overpressure, light, and temperature effects and the hazard level that would be expected to cause crew injury.

Keywords: kinetic energy penetration, hypervelocity penetration, blast pressure, air blast, light flash, spacecraft interior, orbital debris, meteoroid

1. INTRODUCTION

Studies by Kessler¹ and others indicate that the likelihood of orbital debris penetration increases with increased spacecraft size and time of exposure in low Earth orbit. With this increased likelihood of debris impact comes a responsibility on the part of the manned spacecraft designer to (1) provide effective shielding to prevent the likelihood of penetration to the maximum practical extent, and (2) to reduce the hazardous effects on the crew should a penetration occur. The latter responsibility requires detailed information on the magnitude of the atmospheric hazard associated with orbital debris penetration and the effects of such factors as internal equipment and crew proximity on increasing the likelihood of their survival following a penetration.

The primary objective of this study was to establish through experimentation the level of spacecraft cabin over pressure, light, and temperature that accompanies penetration of typical orbital debris shielding as a function of distance from the source of penetration. A secondary objective was to examine the effectiveness of internal equipment and/or spall blankets in reducing the levels of these hazardous effects on the crew. The data from these experiments will be used in future research efforts to establish a model for the level of hazardous internal effects as a function of orbital debris impact parameters (debris diameter and velocity), spacecraft shield design, and crew distance from the point of penetration. The availability of such a model for predicting the magnitude of atmospheric hazard levels following the remote likelihood of a penetration allows the spacecraft designer to adapt his design to improve the survivability of spacecraft occupants from these hazards should they occur.

2.0 REPORT FORMAT

This report consists of the main body which describes the experiments and summarizes the results obtained plus Appendices which presents all of the processed data from each of the tests performed on this program. Appendix A includes the Target Plate photographs, the test chamber temperature profiles, the test chamber pressure profiles, and the UV and visible band radiometric data. Appendix B includes the available flash X-Ray photographs for the test series.

As mentioned in the preface, this document comprises Volume I, Experimental Program portion of the Final Report "Vulnerability of Space Station Freedom Modules, A Study of the Effects of Perforation on Crew and Equipment" for this contract. Volume II, Analytical Modeling of Internal Debris Cloud Effects of the Final Report "Vulnerability of Space Station Freedom Modules, A Study of the Effects of Perforation on Crew and Equipment" by Dr. Wm. P. Schonberg is available under separate cover.

3.0. EXPERIMENTAL SETUP

3.1 FACILITY

In order to meet these objectives, the Marshall Space Flight Center (MSFC) and the University of Alabama in Huntsville (UAH) conducted a series of hypervelocity impact tests at the UAH Aerophysics Research Center (ARC), located on Redstone Arsenal near Huntsville, Alabama. The ARC features a variety of light gas gun systems capable of accelerating projectiles to speeds in excess of 7.5 km/sec. The particular gun chosen for this test series features a launch tube capable of firing particles up to 3.0 cm in size at near 7 km/s and a target chamber approximately 2 meters in diameter and 4 meters in length.

3.2 TARGET CHAMBER

Figure 1 shows a photograph of the external view of the target chamber looking at the chamber from the North West side. The pulser for the flash X-ray and the 17 GHz Doppler radar can be seen in the foreground. Figure 2 shows a photograph of the internal arrangement of the target chamber for Test # 1 without the equipment Rack Simulant and Test #5 with the equipment rack simulant. Note that the internal surfaces of the chamber were lined with 1 cm polyurethane foam panels. These panels reduced the "noise" in the over pressure readings considerably when compared to several checkout tests without the foam liners, and so were utilized through the tests reported here. Note also the presence of a square fiberboard witness panel hung from the chamber ceiling approximately 2.6 meters downrange of the point of penetration in order to characterize the mass characteristics within the debris cloud from the penetrating particle and shield target assembly.

3.3 TEST CONDITIONS

Prior to the test, the target chamber was carefully sealed with a ballistic test article simulating a "typical" orbital debris shield in order to maintain an approximate 1 atm internal (absolute) pressure as the test chamber upstream of the impact tank was pumped down to a near vacuum condition. The bumper shield plate and enhancer materials were held on frames in the two feet diameter tube which served as a mount for the bumper shields and the hull plate. The hull plate provided the seal for the test chamber at ambient atmosphere from the vacuum on the gun side of the hull plate. The range chamber uprange of the hull plate was connected to a 8' diameter by ~200' long chamber which was pumped down to act as a large vacuum dump, thereby simulating the infinite vacuum of space as the hull plate was perforated. In this fashion, the penetrating projectile simulates the passage of a space debris particle from the vacuum of space into a crew cabin. All hypervelocity impact tests within this series were conducted using 7075 Al spheres moving at approximately 6.5 km/sec.

3.4 INSTRUMENTATION SET UP

Figures 4 and 5 show cross-sectional top views of the test chamber for the cases without and with the simulated internal equipment cabinets respectively. Pressure and temperature sensors were paired in six positions within the target tank, three pairs along each side. For most tests, pressure and temperature sensors 1E and 1W were located on the east and west walls (respectively) of the tank at an approximate "line of sight" distance of 62 cm from the pressure bearing surface (pressure wall) of the shield target. Sensors 2E and 2W were approximately 136 cm from the pressure wall of the shield target; sensors 3E and 3W were approximately 253 cm from the target pressure wall. Notable exceptions to these general sensor locations included (1) the position of temperature sensor 3W, which was lengthened subsequent to Test 1 to measure the temperature directly along the centerline of the test chamber, and (2) the position of temperature and pressure sensors 1W in Tests 10 and 13, which were also extended to measure the over pressure inside an equipment rack mockup very near the point of penetration (see Figure 2). A low speed video camera (30 frames/sec) was trained at the target plate through a Plexiglas window and mirror arrangement at the roof of the target chamber.

The pressure sensor used was a Dytran Model 2200V1, with a frequency response of 500 kHz and capable of measuring a peak output level of 100 psi (690 kPa) with a resolution of approximately 0.01 psi (0.07 kPa). The temperature sensor used was an Omega Type E thermocouple with a frequency response of 2 msec and capable of measuring a peak output level of 600 degrees C with a resolution of approximately 0.1 degrees C.

Three UDT Model UV50 radiometers that were used to measure the magnitude of (1) visible light when directly facing the penetration point, (2) ultraviolet (UV) light when directly facing the penetration point, and (3) visible light when facing 90 degrees away from the penetration point. The visible light detector bandwidth was set at 400 to 750 nm and the UV detector bandwidth was set at 250 to 360 nm. The sensors were located from 155 to 190 cm from the point of penetration.

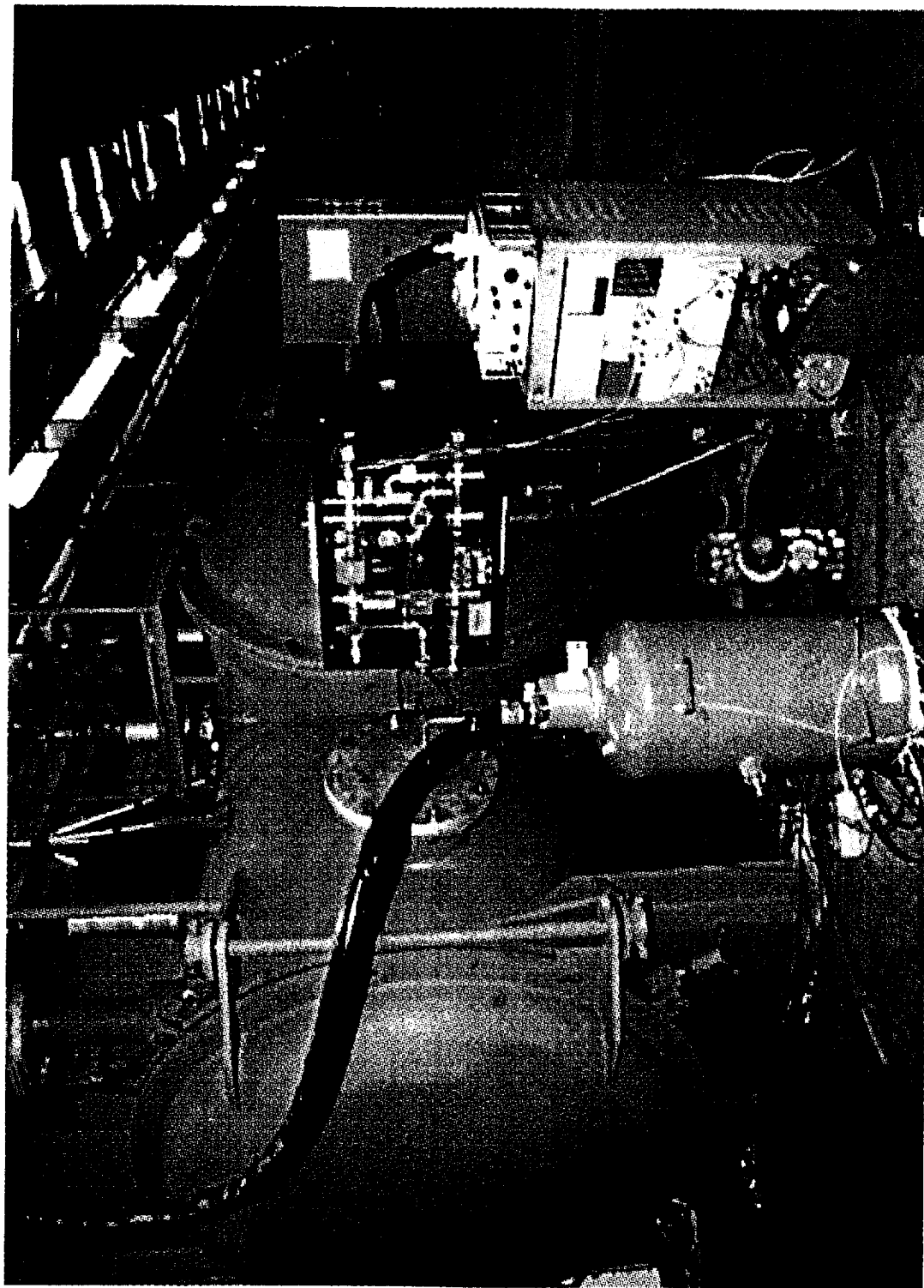


Figure 1 Photograph of the UAH Target Chamber for the 108 mm Gun System used in this Test Series

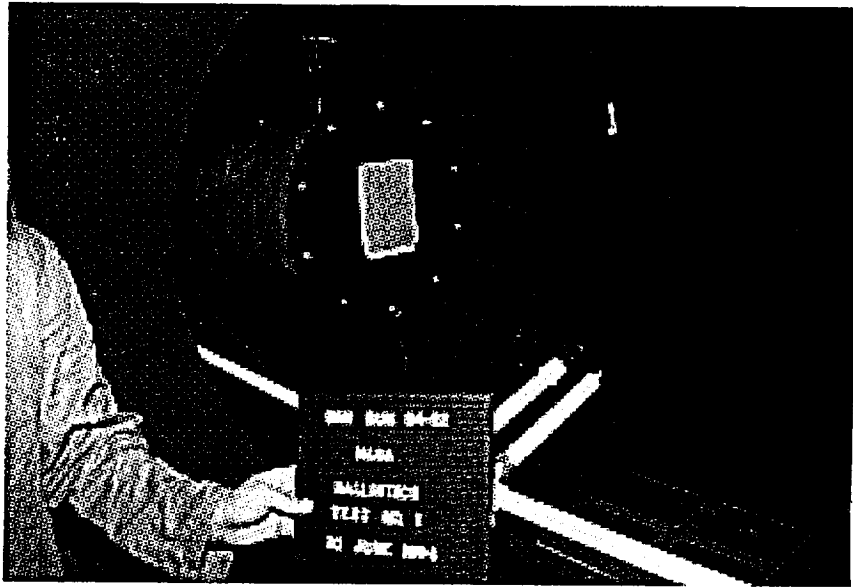


Figure 2 View of Impact Chamber Interior Without Equipment Rack Simulant

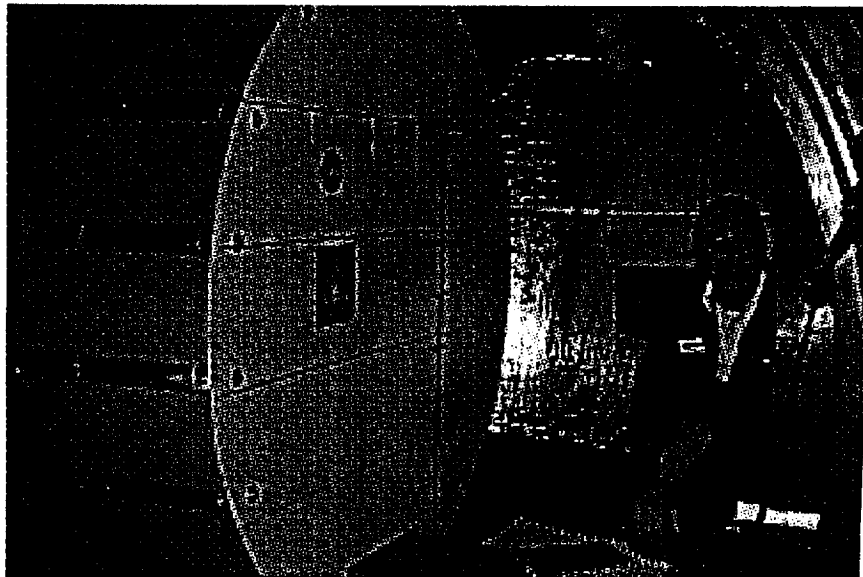


Figure 3 View of Impact Chamber Interior With Equipment Rack Simulant

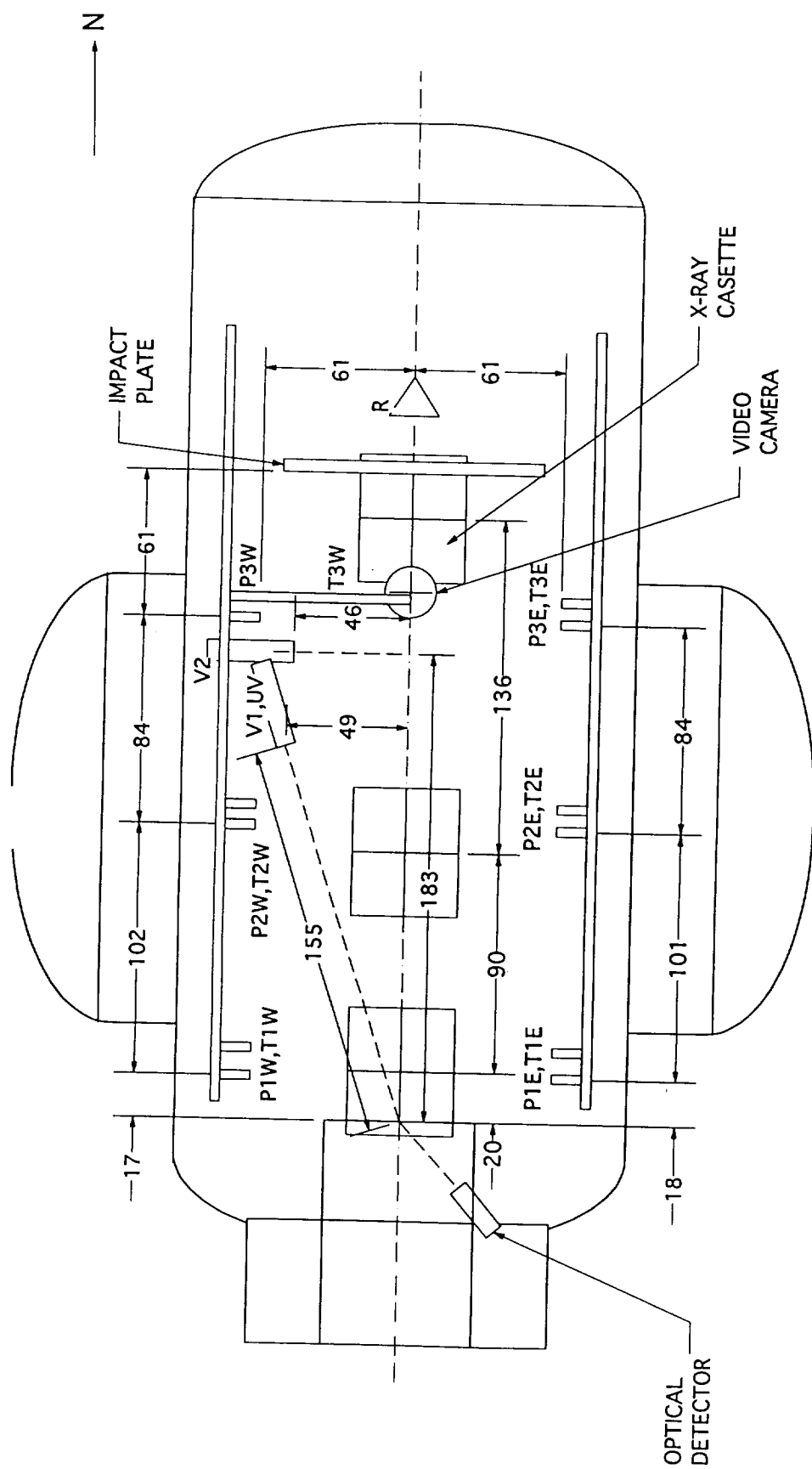


Figure 4 Cross Sectional Top Down View of Test Chamber Without Equipment Rack Simulant

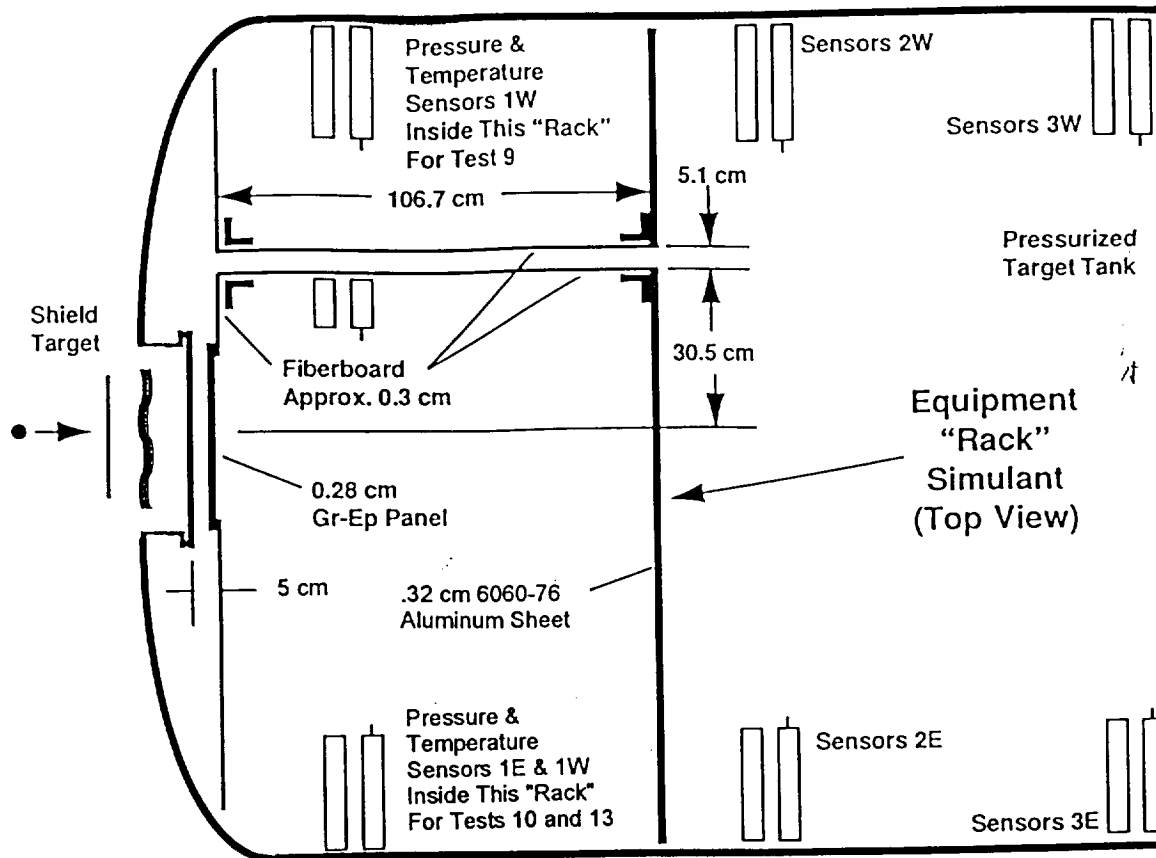


Figure 5 Cross Sectional Top Down View of Test Chamber With Equipment Rack Simulant

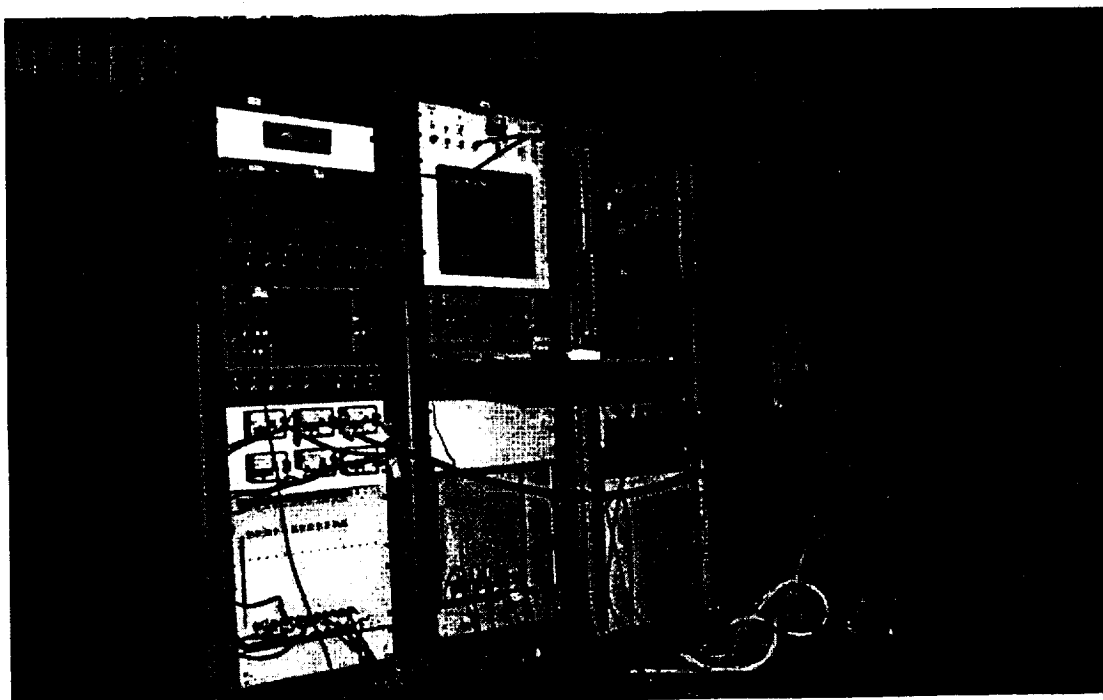


Figure 6 Photograph of Digital Acquisition System

In order to obtain a measure of the residual energy in the debris cloud from the penetration of the target plate, a 17 GHz Doppler radar was installed to view the motion of the witness plate during the tests. This data is presented in Figure 13.

The deflection of the pressure hull plate was measured using a Doppler radar operating at 17 GHz in an interferometric mode as the uprange side was pumped down to < 0.01 Torr with atmospheric pressure in the test chamber. This plate deflection data is shown in A39 of Appendix A

Flash X-rays were obtained on most tests. The available flash X-ray data are presented in Appendix B

3.5 DATA ACQUISITION

Data acquired by the various sensors were recorded on a Nicolet Digital Data Acquisition system which has a maximum sampling rate of 10 MSamples/s, 12 bit resolution and 1 Mbyte memory per channel. The actual sampling rate was adjusted depending on the expected data recording time. The instrumentation rack which contains the data acquisition system is shown in Figure 6.

3.6 SPACECRAFT SHIELD TARGETS

Figure 7 shows a sketch of the three types of spacecraft shield targets that were featured in this test series. Shield target 1 is essentially a simple two-wall bumper shield, with the second wall acting as the pressure bearing surface of the spacecraft. The ballistic limit (size of aluminum sphere that will marginally penetrate this type of target) for shield target 1 is approximately 1.0 cm (at 6.5 km/sec). Shield target 2 is an enhanced orbital debris shield that features intermediate layers of Nextel, Kevlar, and graphite between the outer bumper and rear pressure wall. These layers increase the ballistic limit of this shield package to approximately 1.35 cm (at 6.5 km/sec). Shield target 3 is a simple single pressure wall with no bumpers. The ballistic limit of this target is very low, requiring only a 0.1 cm spherical aluminum particle to penetrate this shield target.

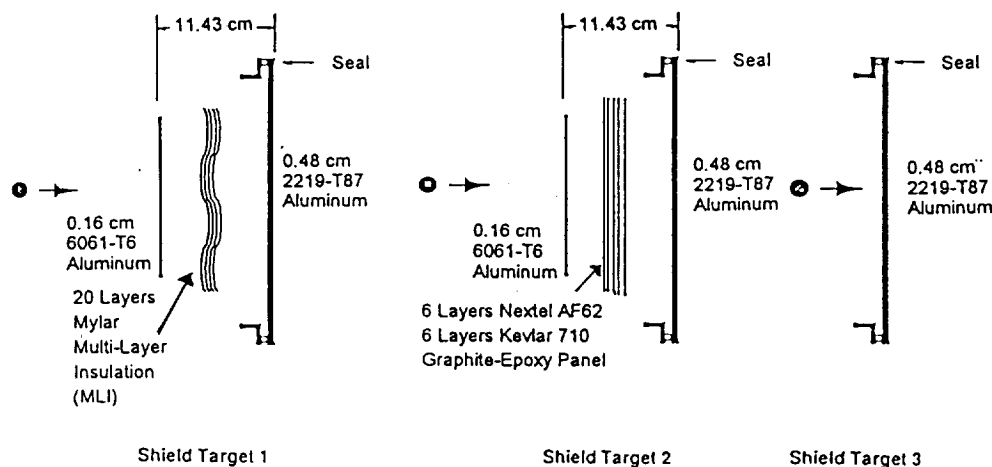


Figure 7 Sketch of Three Space Craft Shield Targets

Figure 8 shows photographs of the internal arrangement of the target chamber for Test 5. Note that the internal surfaces of the chamber were lined with 1 cm thick polyurethane acoustic attenuating foam panels. These panels reduced the "noise" in the over pressure readings considerably compared to several checkout shots without the foam liners, and so were utilized through the tests reported here. Note also the presence of a square fiberboard witness plate hung from the chamber ceiling approximately 2.6 meters downrange the point of penetration in order to determine the mass characteristics within the debris cloud from the penetrating particle and shield assembly.

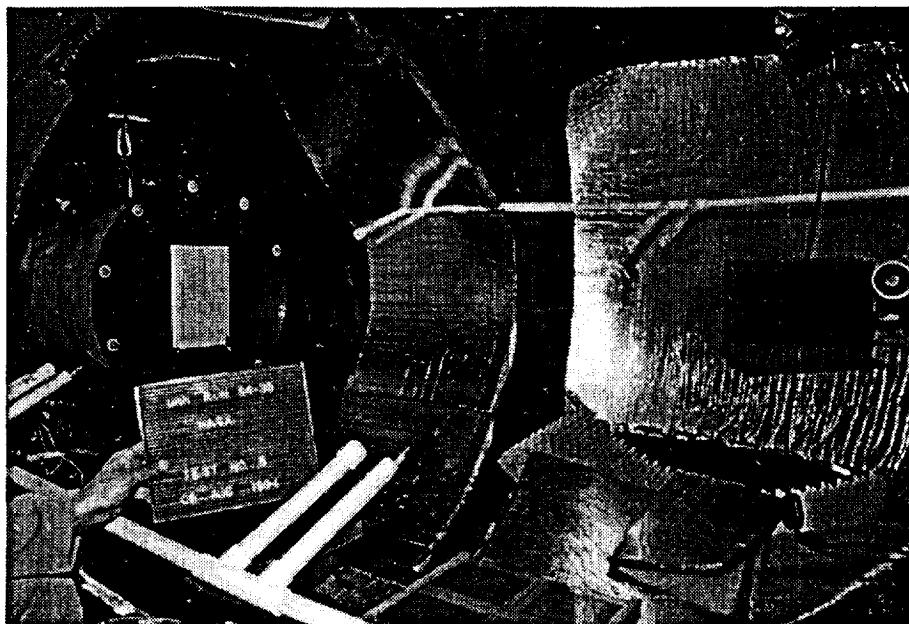


Figure 8a Photograph of Target Chamber for Test 5 - View Towards Shield Target

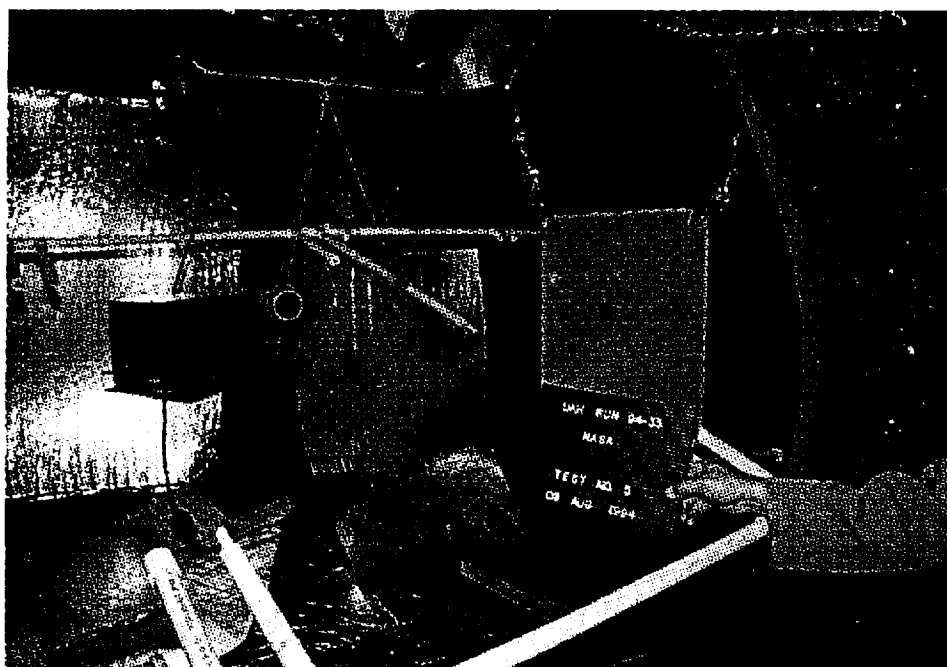


Figure 8b Photograph of Target Chamber for Test 5 - View Away from Shield Target (Downrange)

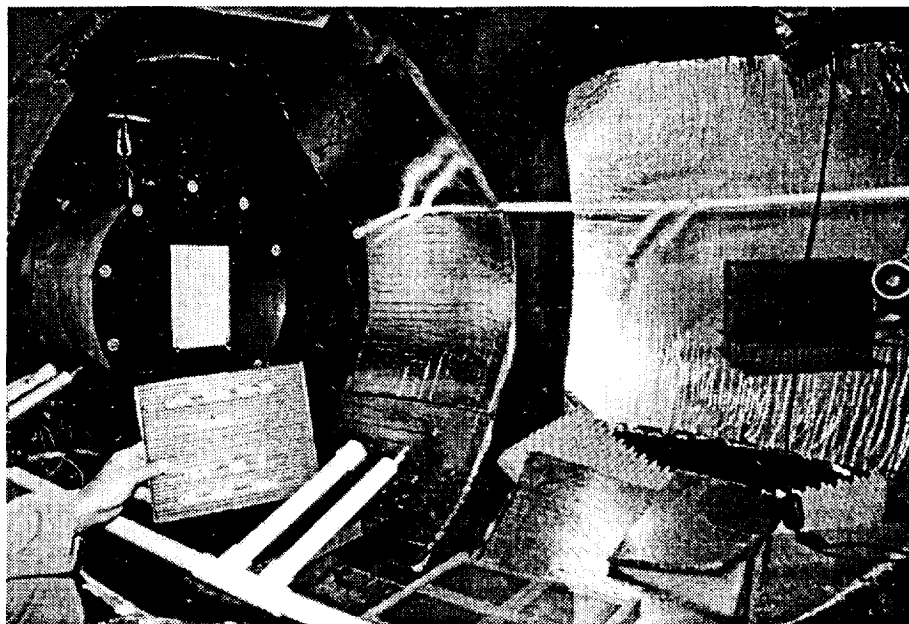


Figure 8a Photograph of Target Chamber for Test 5 - View Towards Shield Target

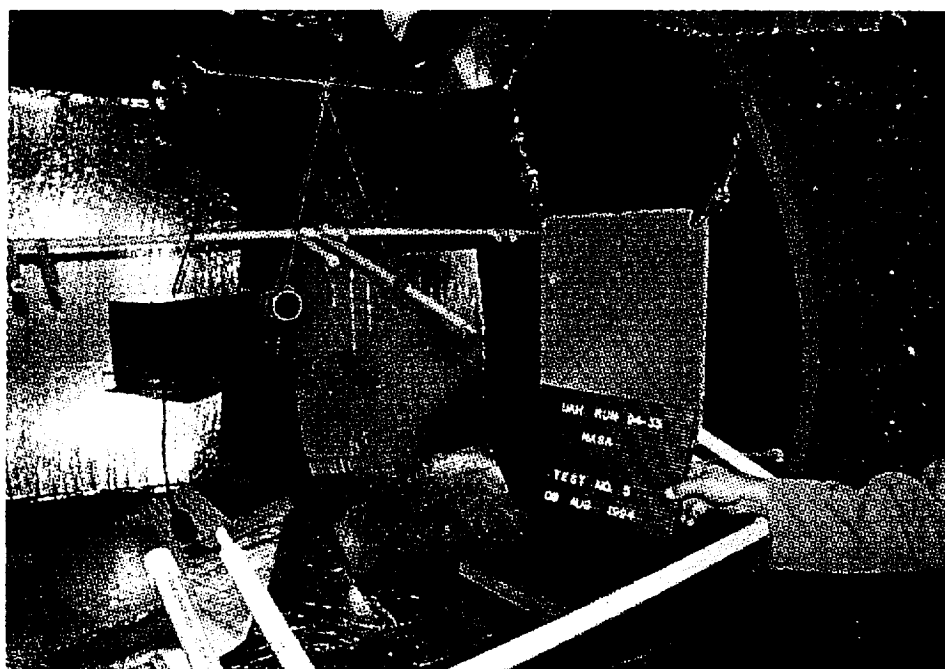


Figure 8b Photograph of Target Chamber for Test 5 - View Away from Shield Target (Downrange)

Table 1. Over pressure Test Results

Test Number		1	1	1	2	3	1 +Blanket	1 + Rack	2+ Rack	2+ Rack
		1	3	6	5	8	11	10	9	13
Projectile Diameter		1.27 cm .500 in	1.59 cm .625 in	1.59 cm .625 in	1.59 cm .625 in	0.95 cm .375 in	1.27 cm .500 in	1.59 cm .625 in	1.59 cm .625 in	1.59 cm .625 in
Velocity (k/s)		6.70	6.42	6.50	6.58	6.64	6.46	6.63	6.21	6.52
Sensor 1E	Peak Over pressure	117 kPa 17 psi	141 kPa 20.5 psi	110 kPa 16.0 psi	234 kPa 34.0 psi	262 kPa 38.0 psi	38 kPa 5.5 psi	55 kPa 8.0 psi	-	145 kPa 21.0 psi
	Duration of Peak	0.35 ms	0.50 ms	0.45 ms	0.45 ms	0.35 ms	0.20 ms	0.10 ms	-	0.10 ms
Sensor 1W	Peak Over pressure	121 kPa 17.5 psi	148 kPa 21.5 psi	214 kPa 31.0 psi	276 kPa 40.0 psi	193 kPa 28.0 psi	-	97 kPa 14.0 psi	3 kPa * 0.4 psi	207 kPa 30.0 psi
	Duration of Peak	0.35 msec	0.50 msec	0.40 msec	0.40 msec	0.40 msec	-	0.10 msec	0.10 * msec	0.10 msec
Sensor 2E	Peak Over pressure	31 kPa 4.5 psi	117 kPa 17.0 psi	103 kPa 15.0 psi	69 kPa 10.0 psi	48 kPa 7.0 psi	-	9 kPa 1.3 psi	5 kPa 0.7 psi	10 kPa 1.4 psi
Sensor 2W	Peak Over pressure	41 kPa 6.0 psi	145 kPa 21.0 psi	97 kPa 14.0 psi	103 kPa 15.0 psi	45 kPa 6.5 psi	124 kPa 18.0 psi	9 kPa 1.3 kPa	3 kPa 0.5 psi	6kPa 0.9 psi
Sensor 3E	Peak Over pressure	21 kPa 3.0 psi	55 kPa 8.0 psi	83 kPa 12.0 psi	21 kPa 3.0 psi	7 kPa 1.0 psi	34 kPa 5.0 psi	9 kPa 1.3 psi	10 kPa 1.5 psi	8 kPa 1.2 psi
Sensor 3W	Peak Over pressure	17 kPa 2.5 psi	55 kPa 8.0 psi	48 kPa 7.0 psi	28 kPa 4.0 psi	7 kPa 1.0 psi	21 kPa 3.0 psi	9 kPa 1.3 psi	3 kPa 0.5 psi	4 kPa 0.6 psi

* Pressure sensor located in adjacent rack (see Figure 2)

Table 2. Temperature Test Results

Target		1	1	1	2	3	1 + Blanket	1 + Rack	2 + Rack	2 + Rack
Test Number		1	3	6	5	8	11	10	9	13
Projectile Diameter		1.27 cm .500 in	1.59 cm .625 in	1.59 cm .625 in	1.59 cm .625 in	0.95 cm .375 in	1.27 cm .500 in	1.59 cm .625 in	1.59 cm .625 in	1.59 cm .625 in
Velocity (km/s)		6.70	6.42	6.50	6.58	6.64	6.46	6.63	6.21	6.52
Sensor 1E	Peak delta temp. (deg C)	25	105	20	65	20	40	280+	--	--
	Time to peak temp. (msec)	15	10	20	15	10	20	400	--	--
	Temp x time (deg C - secs)	0.4	7.0	3.0	3.0	1.0	3.0	380.0	--	--
Sensor 1W	Peak delta temp. (deg C)	30	115	65	55	15	15	--	5 *	280+
	Time to peak temp. (msec)	20	15	25	20	10	20	--	20 *	1800
	Temp x time (deg C - secs)	0.5	4.5	3.5	4.5	0.9	1.0	--	5 *	330.0
Sensor 2E	Peak delta temp. (deg C)	25	140	50	35	15	75	15	0	5
	Time to peak temp. (msec)	20	10	90	20	12	70	20	--	20
	Temp x time (deg C - secs)	0.7	16.0	5.1	2.0	0.9	4.1	1.5	0	0.5
Sensor 2W	Peak delta temp. (deg C)	20	95	65	220	10	--	20	0	5
	Time to peak temp. (msec)	20	10	50	250	20	--	20	--	20
	Temp x time (deg C - secs)	0.6	11.3	4.5	23.0	0.5	--	4.0	0	0.5
Sensor 3E	Peak delta temp. (deg C)	45	--	280+	10	10	280+	--	0	5
	Time to peak temp. (msec)	1200	--	250	20	270	180	--	--	20
	Temp x time (deg C - secs)	46.3	--	185.0	1.1	9.0	122.0	--	0	0.5
Sensor 3W	Peak delta temp. (deg C)	45+	270	--	25	70	280+	5	10	15
	Time to peak temp. (msec)	300	300	--	20	200	200	1.5	3000	3000
	Temp x time (deg C - secs)	66.5+	131.5	--	1.5	45.0	155	6.0	3.0	4.5

Notes: - All temperatures reported to nearest 5 deg C. interval.
- All times reported to nearest 5 millisecond interval
* Sensors located in adjacent equipment rack (see Figure 3).

Table 3 Radiometric Results and Hole Characteristics

Target	1	1	1	2	3	1 + Blanket	1 + Rack	2+ Rack	2 + Rack
Test Number	1	3	6	5	8	11	10	9	13
Projectile Diameter	1.27 cm .500 in	1.59 cm .625 in	1.59 cm .625 in	1.59 cm .625 in	0.95 cm .375 in	1.27 cm .500 in	1.59 cm .625 in	1.59 cm .625 in	1.59 cm .625 in
Velocity (k/s)	6.70	6.42	6.50	6.58	6.64	6.46	6.63	6.21	6.52
Direct Visible Light (Watts per Steradian)	–	--	40,000	48,000	–	40,000	Lower *	Lower *	Lower *
Indirect Visible Light, 90 deg. from Direct (Watts per Steradian)	30	–	17	14	–	13	–	–	–
Direct Ultraviolet Light (Watts per Steradian)	26	58	--	–	--33	42	8	0.3	–
Effective Pressure Wall Hole Diameter	5.9 cm 2.3 in	6.1 cm 2.4 in	6.3 cm 2.5 in	12.2 cm 4.8 in	3.2 cm 1.3 in	6.1 cm 2.4 in	6.6 cm 2.6 in	8.1 cm 3.3 in	7.1 cm 2.8 in
Maximum Tip-to-tip Crack Length	15.3 cm 6.0 in	8.7 cm 3.4 in	14.2 cm 5.6 in	24.9 cm 9.8 in	No Crack	7.9 cm 3.1 in	9.7 cm 3.8 in	22.6 cm 8.9 in	25.1 cm 9.9 in
Mass Removed from Pressure Wall	37 g	39 g	42 g	–	12 g	42 g	52 g	6 g	7 g

* Radiometer data not available, but video tape indicates that direct light flash levels were severely reduced.

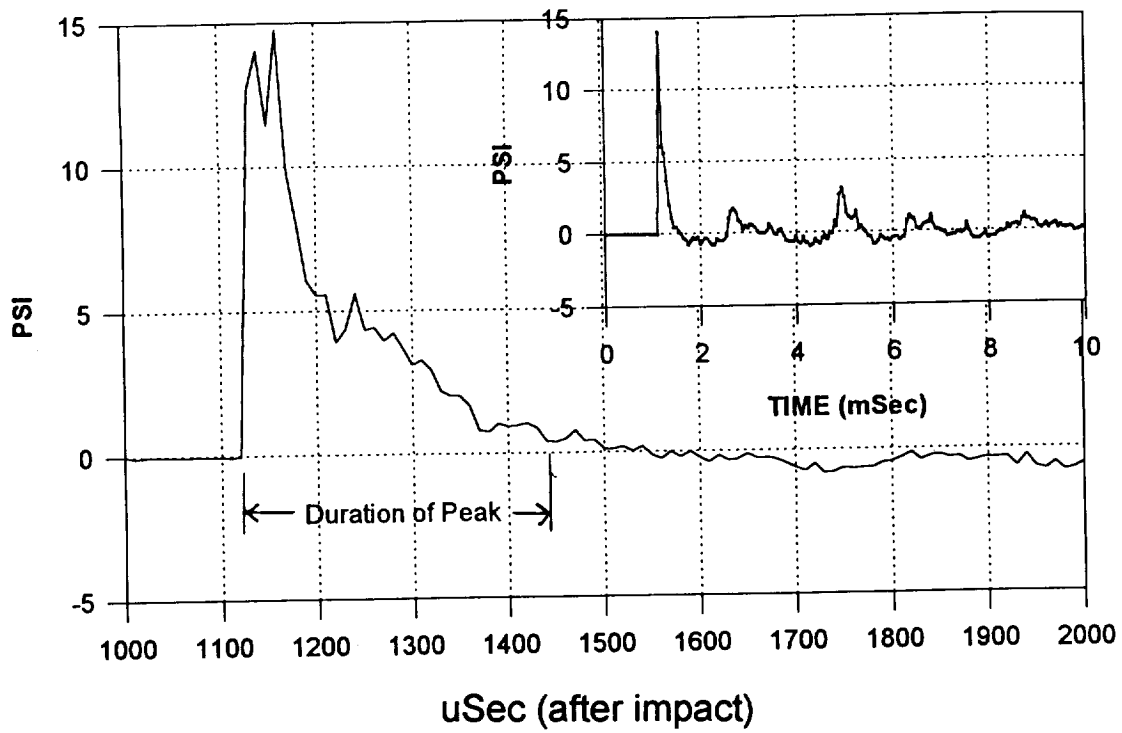


Figure 9 Typical Over Pressure Profiles from Sensor Position 1 (No Internal Equipment Simulant)

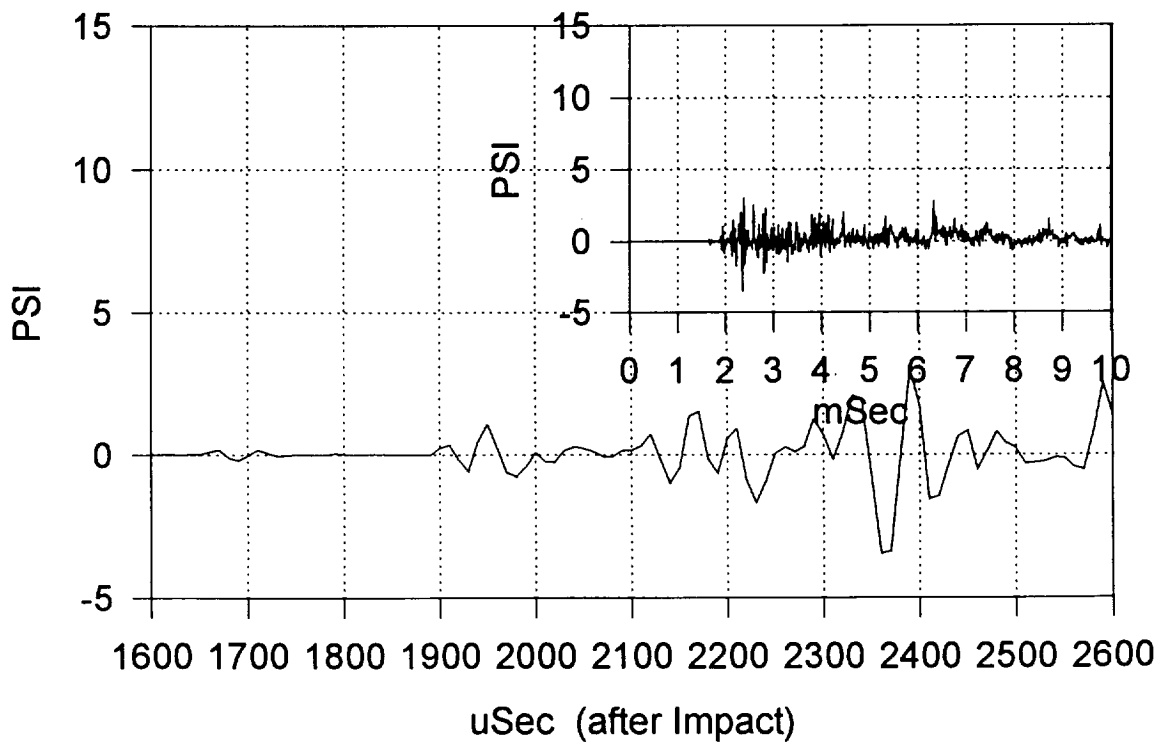


Figure 10 Typical Over Pressure Profiles from Sensor Position 3 (No Internal Equipment Simulant)

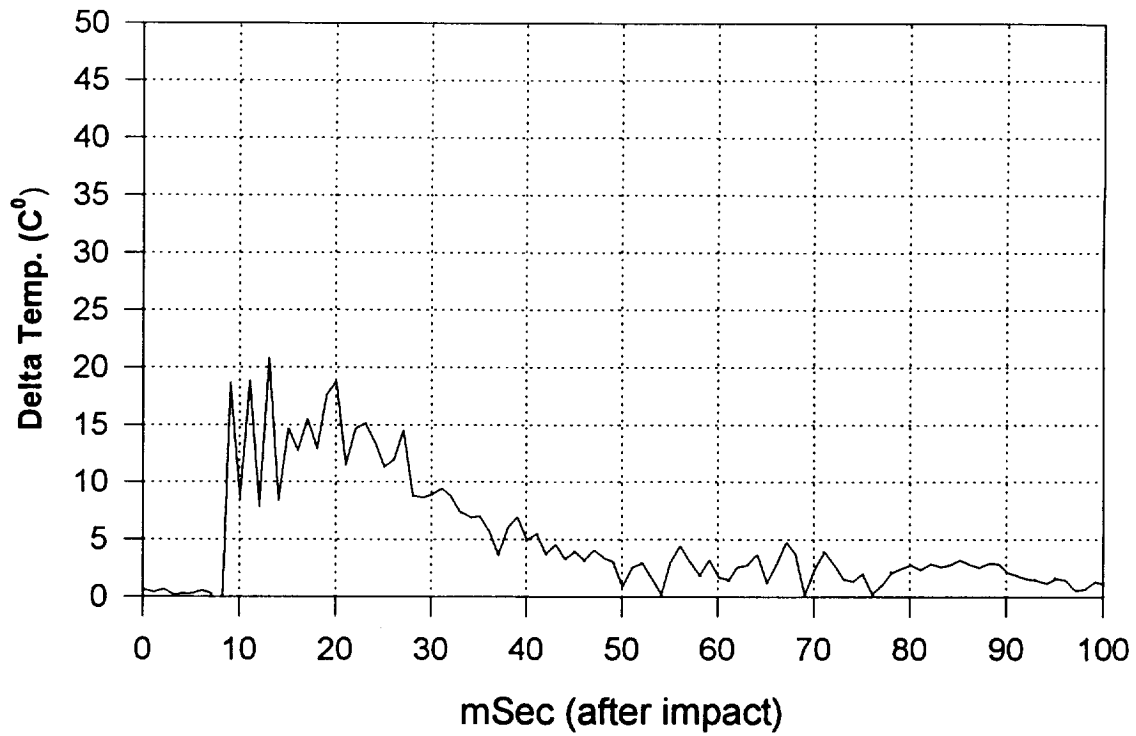


Figure 11 Typical Temperature Profiles from Sensor Position 1 (No Internal Equipment Simulant)

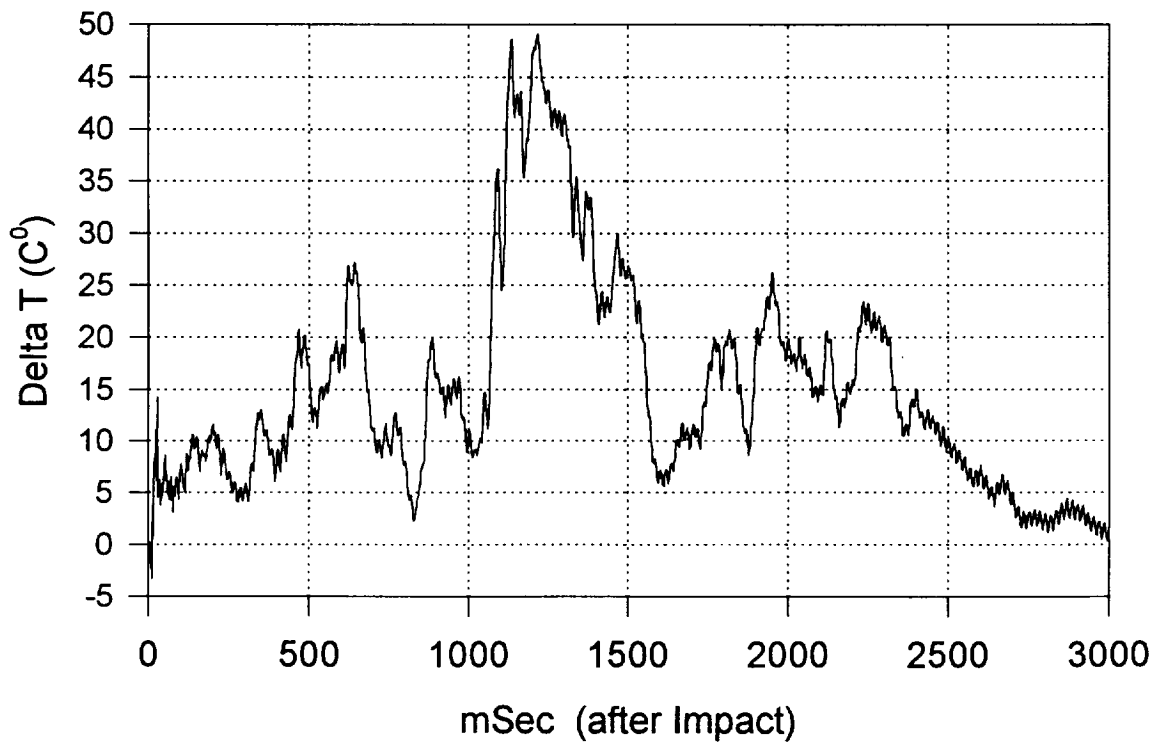


Figure 12 Typical Temperature Profiles from Sensor Position 3 (No Internal Equipment Simulant)

approximately 40 grams (also true for all tests of shield type 2). Despite this large amount of initial mass in the debris cloud, the one meter square fiberboard witness panel (weighing 2700 gms) located at 2.7 meters from the impact point was relatively undamaged, with one small (< 0.1 gram) particle imbedded within it. This lack of mass in the witness panel was curious, and consistent throughout the tests of all target types. This observation is supported by the Doppler radar measurement of the witness plate motion. The projectile mass was 3.0 gms and actual velocity was 6.69 km/s, resulting in projectile momentum of 2×10^6 gm-cm /s. The witness plate mass was 2702 gms and measured velocity was 20 cm/s, resulting in momentum of 67,550 gm-cm/s. The target momentum measurement presented in Figure 13 shows very low ($\sim 3.3\%$ of the projectile momentum) momentum transfer to the witness plate.

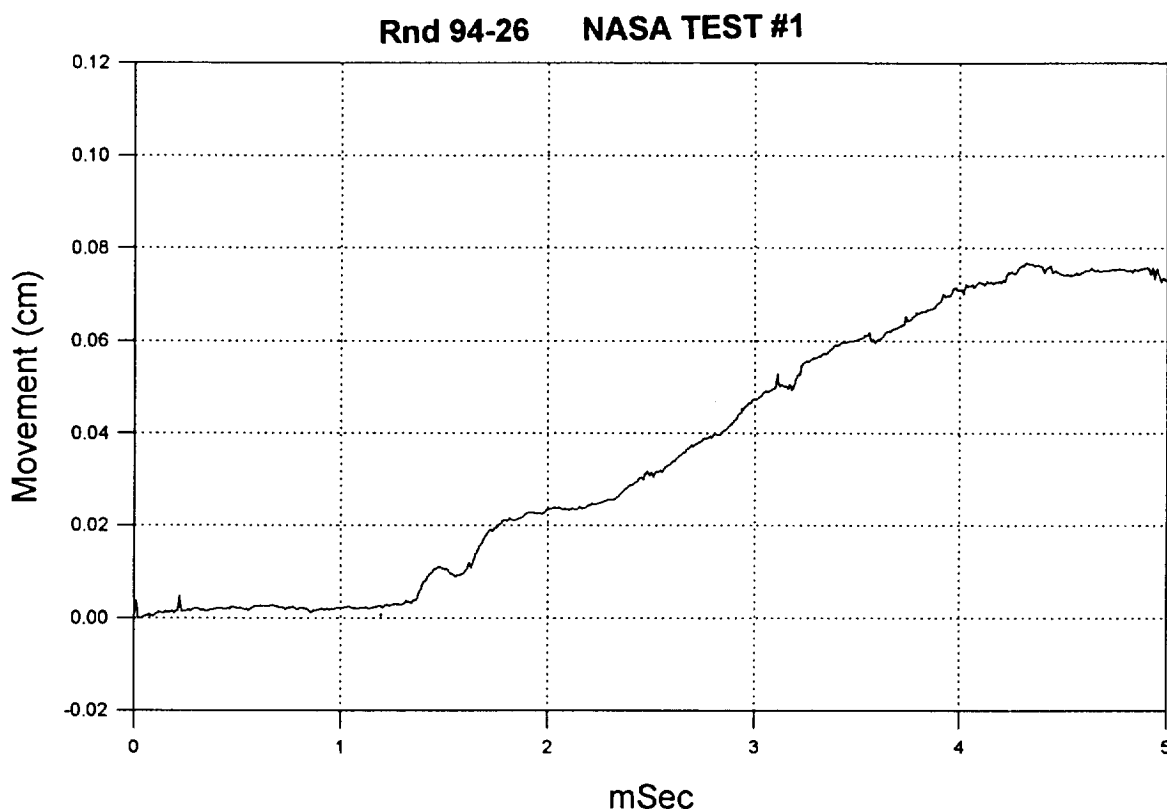


Figure 13 Doppler Radar data on Witness Plate Motion

One possible explanation for this apparent lack of post-test debris mass downrange might be that the debris cloud had a high radial component to its velocity vector--that is, the debris "spread out" quickly to the sides of the chamber and did not proceed directly along the centerline of the target chamber where the witness plate was located. It is difficult to discount this explanation without better flash X-ray characterization of the debris cloud and/or witness plates located along the inner walls of the test chamber; however, relatively little debris was noted to be imbedded within the polyurethane foam lining the chamber walls following the tests. A low speed (30 frames/second) video from these tests indicated a roughly even radial distribution of visible debris fragments particles emerging from the target into the 1 meter field of view of the camera (downrange). Another interesting possibility is that the fine debris cloud particles "burned up" as well slowed down

through drag deceleration in flying through the ambient air atmosphere of the target chamber at high velocity, and only rarely reached the witness plate. This explanation is attractive because of the highly exothermic reaction of hot aluminum particles with oxygen in the air atmosphere generating ~400 kilo-calories per mole of reacting aluminum. This is manifested by the over pressure, temperature, and light energy data witnessed in the tests. MSFC is sponsoring additional flash X-ray characterization tests to better typify the mass distribution within debris clouds traveling in a vacuum versus those traveling through a spacecraft interior atmosphere.

Another interesting observation concerning the effect of debris cloud mass on overpressure level may be drawn from comparing the low levels of overpressure at sensor position 3 in Test 5 (shield target 2) and Test 8 (shield target 3) to higher overpressure levels for sensor position 3 in Tests 1, 3 and 6 (shield target 1). Table 3 shows that even though the effective hole size is larger in shield type 2 due to its larger petals (see Figure 4), the amount of mass lost in the wall (and thus the amount of mass in the debris cloud) is an order of magnitude lower in shield type 2 than in shield type 1. The same is true for Test 8, where the mass missing from the pressure wall is very low compared to Tests 1, 3 and 6 (shield type 1). Thus, the lower overpressure downrange for Test 5 and for Test 8 (shield types 2 and 3 respectively) validates our reasoning that overpressure may be directly related to debris cloud mass.

Why the higher overpressure for these tests (5 and 8) at sensor position 1 compared to Tests 1, 3 and 5 (shield target 1)? One may theorize that these higher overpressures near the target are occurring for different reasons, unrelated to debris cloud mass. In Test 5, the formation and motion of large petals attached to the pressure wall may be causing a short range multiplying effect on the over pressure level near the wall (note the severely reduced overpressure at sensor position 2. In Test 6, the initial velocity of the debris cloud was much higher--approximately 6 km/sec (velocity of the impacting particle). This higher velocity led to a stronger air shock to be induced near the pressure wall, though its effects dissipated quickly.

4.2 ENVIRONMENT EFFECTS ON CREW

Overpressure levels of the magnitudes shown in Table 1 (ranging from 10 to 270 kPa) can have varying affects on incapacitating crew members (i.e., rendering crew incapable of rescuing themselves from the depressurizing spacecraft). While none of these overpressure levels appeared to be of sufficient duration to cause damage to lungs or other internal organs, they are of sufficiently high magnitude and duration to cause serious damage to the eardrum, inner ear, and cranium.²

Table 2 shows that for tests performed without simulated internal equipment racks, the peak air temperature at sensor position 2 reached generally higher levels than those at sensor position 1, with highest values recorded at sensor position 3. Air temperature peaks at sensor 1 generally occurred at around 20 milliseconds (ms) after pressure wall penetration; temperature peaks at sensor position 2 occurred at approximately 50 ms; they occurred at sensor position 3 at approximately 250 ms. These temperature and time readings indicate that the heated, shocked air from upstream (nearest the target) appeared to move downstream more slowly than the debris cloud (10 m/s, versus 1000 m/s for the debris cloud). As it moves downstream, this slower moving mass of heated air combines with additionally shocked air (downstream) to reach increasingly high overall air temperatures (280+ deg C in some cases). However, the highest observed product of air temperature x duration observed (185 deg C-secs for sensor position 3 in Test 6) did not exceed the air temperature levels that might reasonably be expected to induce second degree burns (1200 deg C-secs).³

Table 3 shows that the light levels for the tests without the internal equipment rack varied strongly with viewing angle. Visible light levels exceeded 40Kwatts per steradian (27.2 million candles) when directly viewing the target. UV light levels were much lower; the light flash phenomenon appears to be occurring primarily in the visible regime. This direct visible light level is roughly equivalent to that from the Sun as viewed from outside the Earth's atmosphere, and is certainly

sufficient to cause temporary blindness and other incapacitating effects⁴. However, the level of light as viewed from 90 degrees (i.e., from the side) is on the order of 20 watts per steradian (14,000 candles)--three orders of magnitude less than a direct view of the penetration event, and well within safe levels. Of course, the actual level of "off-axis" light flash observed will probably vary from case to case, depending on the reflectivity of the surrounding spacecraft cabin interior surfaces. Nevertheless, these results point to the dramatic relevance of viewing angle on observed light flash levels following a penetration.

In Test 11, a spall blanket consisting of 12 layers of Kevlar 120 was placed directly on the inboard (target chamber) side of the pressure wall using a two inch Velcro strip (one layer sewn to the spall blanket, the other glued to the pressure wall). The spall blanket in Test 11 was penetrated, creating a two inch hole in the Kevlar and separating the blanket from the wall. Remarkably, both layers of Velcro were still attached to the pressure wall; the joint failure occurred in the nylon thread used to attach the Kevlar blanket to the Velcro strip. Because the spall blanket was penetrated, the overpressure, temperature, and light levels were little effected, with one notable exception--little overpressure was measured at sensor position 1. This could have been caused by the considerable amount of aluminum debris from the pressure wall that was trapped in the spall blanket. With this mass trapped in the blanket, it was unavailable to cause large overpressure (shock waves) as it moved through the air near the target wall.

The presence of the internal equipment rack simulant in Tests 9, 10, and 13 had a large effect on reducing overpressure, temperature, and light flash levels at sensor positions 2 and 3 (outside the equipment rack). Of these tests, the only equipment rack completely penetrated was in Test 13, where a single 0.5 cm hole was induced in the outboard surface of the equipment rack. Once again, reducing the mass of the debris cloud within the target chamber (in this case, to nearly zero) has led to a reduced overpressure and temperature downrange. Note also that the magnitude of the overpressure inside the penetrated equipment rack is lower than that produced had there been no equipment rack (Test 5). In this case, even though penetrated, the rear wall of the equipment rack has reduced the velocity (and probably the mass) of the debris cloud impinging into the equipment rack, reducing the overpressure.

The close proximity of the pressure wall to the graphite epoxy panel on the rear face of the rack simulant (5 cm) also produced a limiting effect on effective hole size in the pressure wall for Tests 9 and 13 (shield target 2). Following these tests, the petals from the pressure wall were imbedded and actually curled around the interior circumference of the hole in the graphite panel (it was very difficult to separate the pressure wall from the rear surface of the equipment rack simulant following the tests). This same contact constrained the formation of petals in the pressure wall for Tests 9 and 13, forcing the effective hole diameters to be 30 percent smaller in these tests than in Test 5. This result is significant--it indicates that equipment racks located behind spacecraft shields similar to target 2 will hinder hole growth (and decompression losses) in spacecraft using these designs. However, repair of the pressure wall in these modules following penetration will be severely hindered by an impaired ability to separate the equipment racks from the pressure wall due to the petalling of the pressure wall around the hole in the back of the equipment rack.

Note however that the temperature at sensor position 1 (within the equipment rack) is considerably larger than in previous tests without the rack. By containing the debris cloud, the equipment rack has contained most of the heat transferred from the kinetic energy of the penetrating particle and debris cloud. Because the volume of the equipment rack is considerably smaller than the target tank, the product of total temperature x duration at sensor position 1 is approximately twice as high as measured for previous tests at sensor position 3 (without the equipment rack).

Unfortunately, light flash measurements from the visible radiometers are unavailable for tests with the equipment rack in place. However, the levels of direct UV light measured were considerably

lower than for tests without equipment racks in place, and the video taped results of these tests provide convincing evidence that far less light flash passed outside of the equipment rack than was seen in tests without the equipment rack.

5. CONCLUSIONS

This series of internal effects tests was successful in meeting its primary and secondary objectives: (1) to establish through experimentation the level of spacecraft cabin overpressure, light, and temperature that accompanies penetration of typical orbital debris shielding as a function of distance from the source of penetration, and (2) to examine the effectiveness of internal equipment in reducing the levels of these hazardous effects on the crew. In addition, the tests led to valuable observations on how debris cloud mass and velocity (and other penetration parameters) affect the levels of overpressure and temperature within a spacecraft atmosphere following orbital debris penetration. This information will be used by MSFC and UAH to formulate a first order relationship between penetration parameters (projectile energy, shielding type, hole size, etc.) and the levels of temperature and overpressure hazards resulting at a given distance from the penetration event.

6. REFERENCES

1. D. Kessler, "Orbital Debris Environment for Spacecraft Designed to Operate in Low Earth Orbit," NASA Technical Memorandum 100-471, 1989.
2. G. Weibull, "A Proposal for Blast Incapacitation Criteria Concerning Soldiers Inside Armoured Vehicles", Proceedings of the Ninth International Symposium on Ballistics, Shrivenham, U.K., May 1986.
3. B. Lawton and M. Laird, "Assessment of Skin Burns Behind Defeated Armour," Proceedings on the Fourteenth International Symposium on Ballistics, Quebec, Canada, September 1993.
4. A. R. Coronado, et al, "Space Station Integrated Wall Design and Penetration Damage Control", Final Report, NASA Contract NAS8-36426, July 1987.
5. Joel Williamsen & John Serrano, "Atmospheric Effects in Spacecraft Interiors Following Orbital Debris Penetration" presented in the Space Environmental, Legal and Safety Session of the Aero-Sense 95 Symposium sponsored by the Society of Photographic Instrumentation Engineers at Orlando FL on 17-18 April 1995. Published in SPIE Proceedings Volume 2483, Paper #2483-06

APPENDICES

APPENDIX A

Test Data

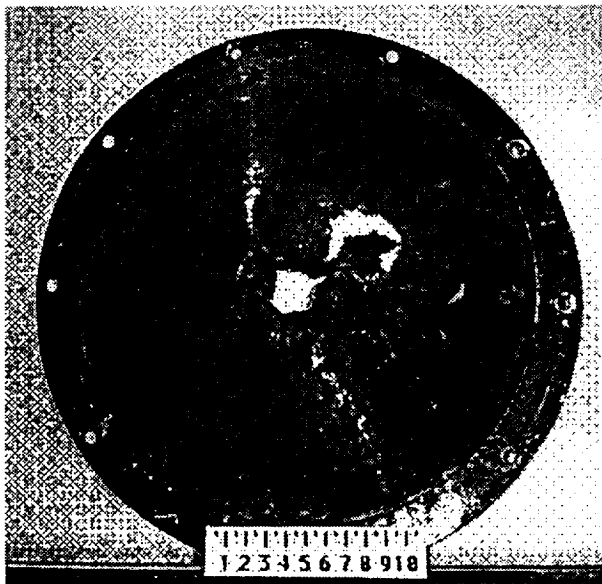
- TARGET PLATE PHOTOGRAPHS
- TEMPERATURE PROFILES
- PRESSURE PROFILES
- UV AND VISIBLE BAND RADIANT INTENSITY

APPENDIX B

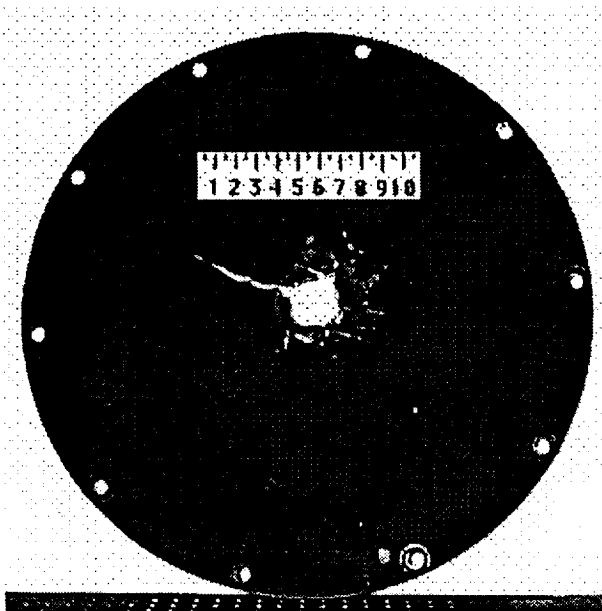
- FLASH X-RAY PHOTOGRAPHS

APPENDIX C

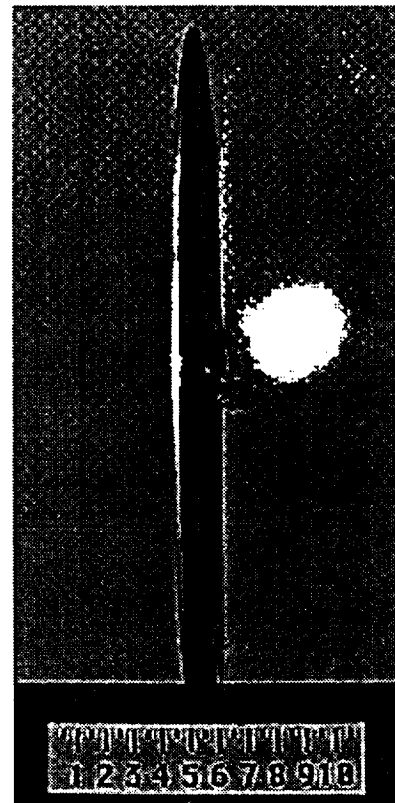
- DISTRIBUTION LIST



Target Plate Front

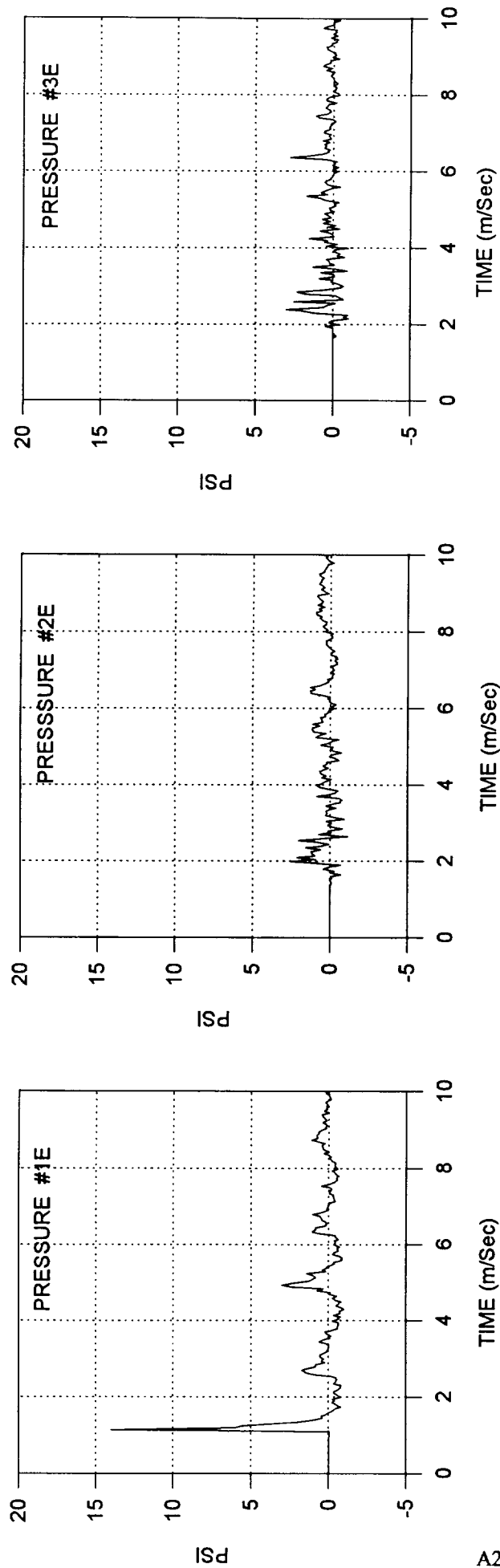


Target Plate Back



Target Plate Side

Figure A1 Target Plate Photographs - Test #1



A2

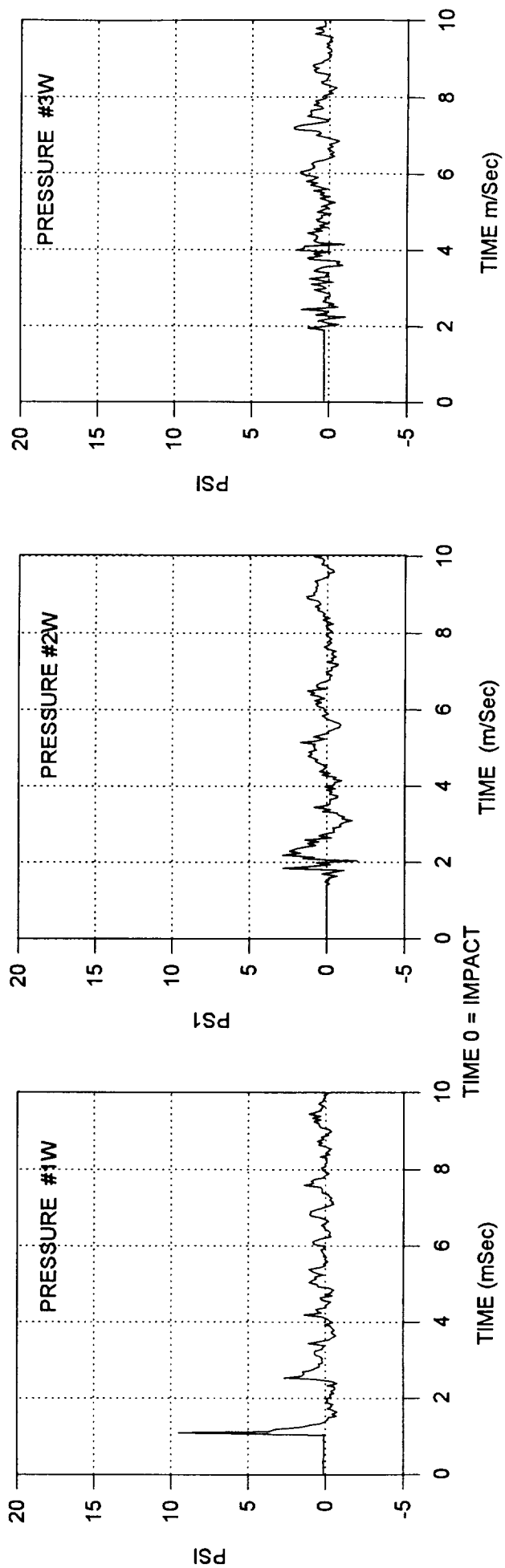


Figure A2 Pressure Profiles - Test #1

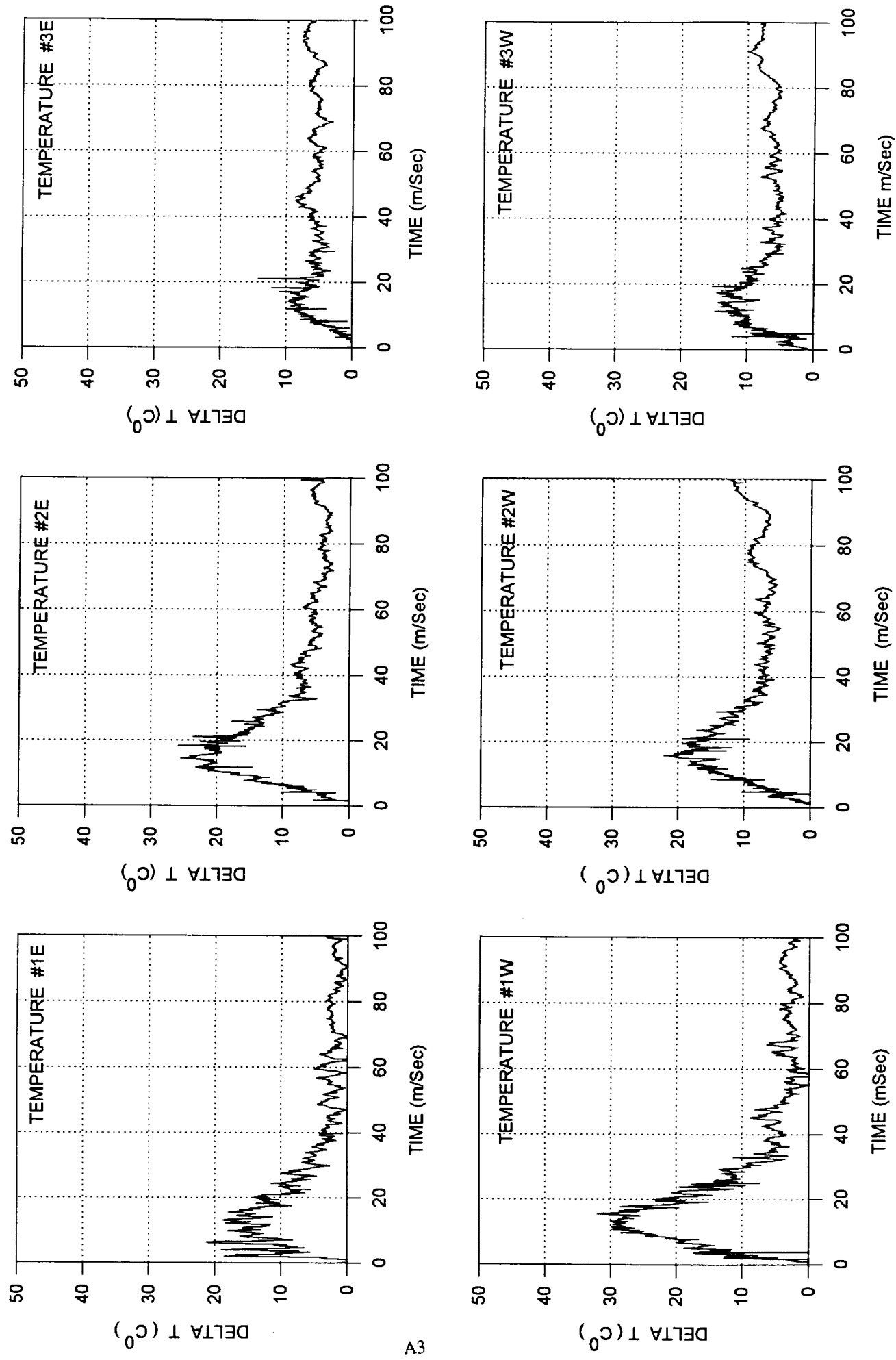


Figure A3 Temperature Profiles - Test #1

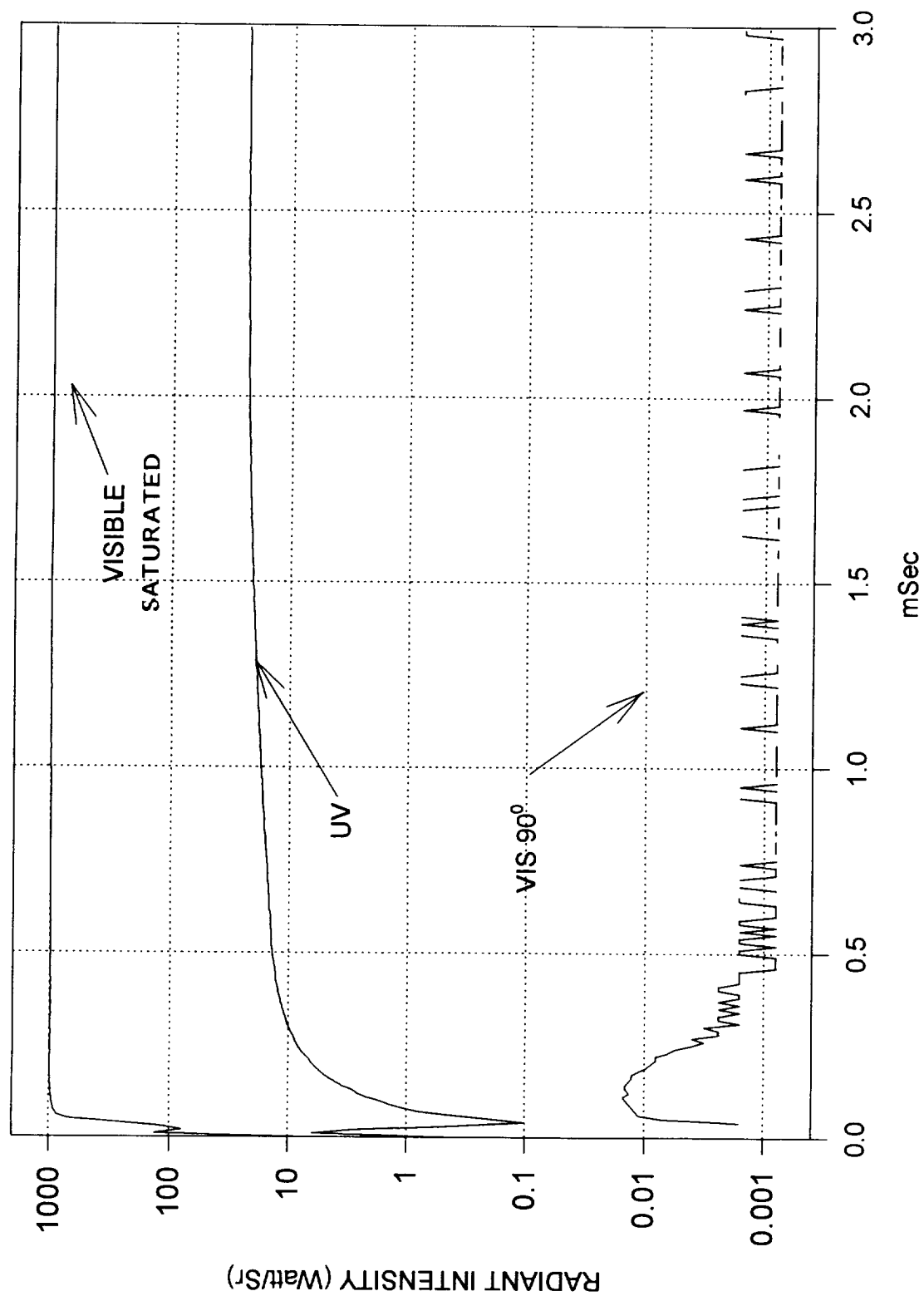
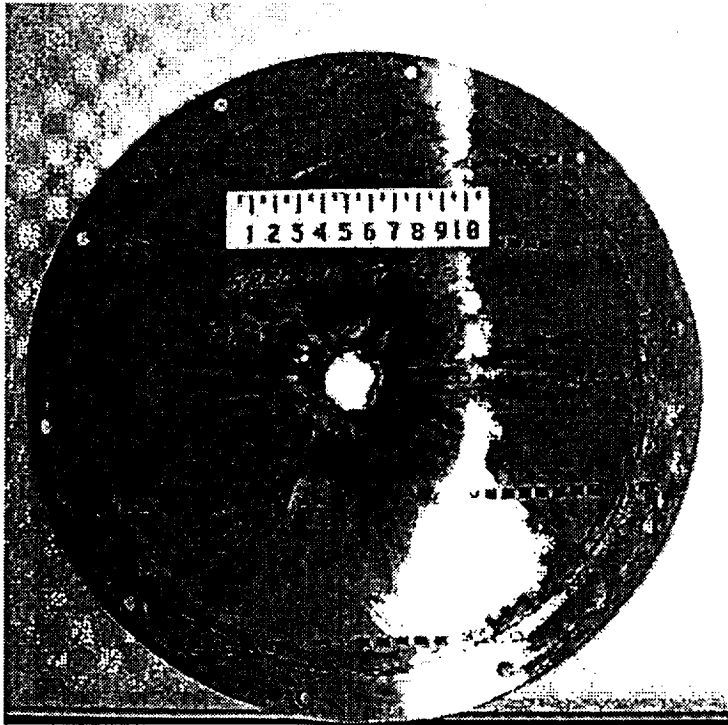
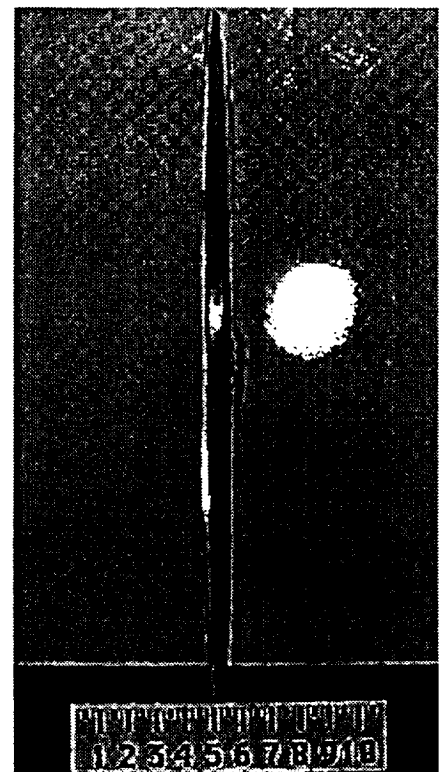


Figure A4 Radiometric Data - Test #1



Target Plate Front



Target Plate Side



Target Plate Back

Figure A5 Target Plate Photographs - Test #2

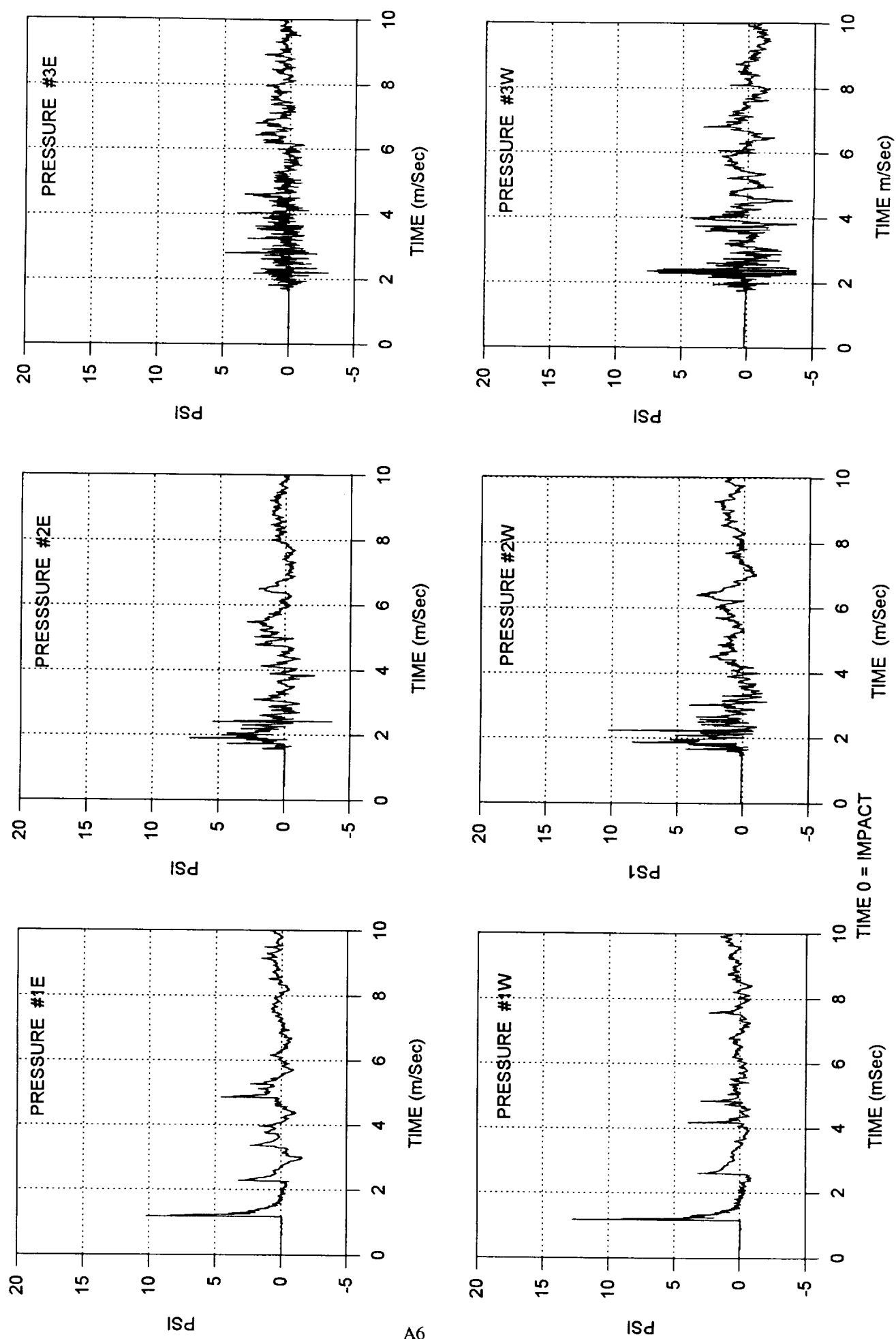


Figure A6 Pressure Profiles - Test #2

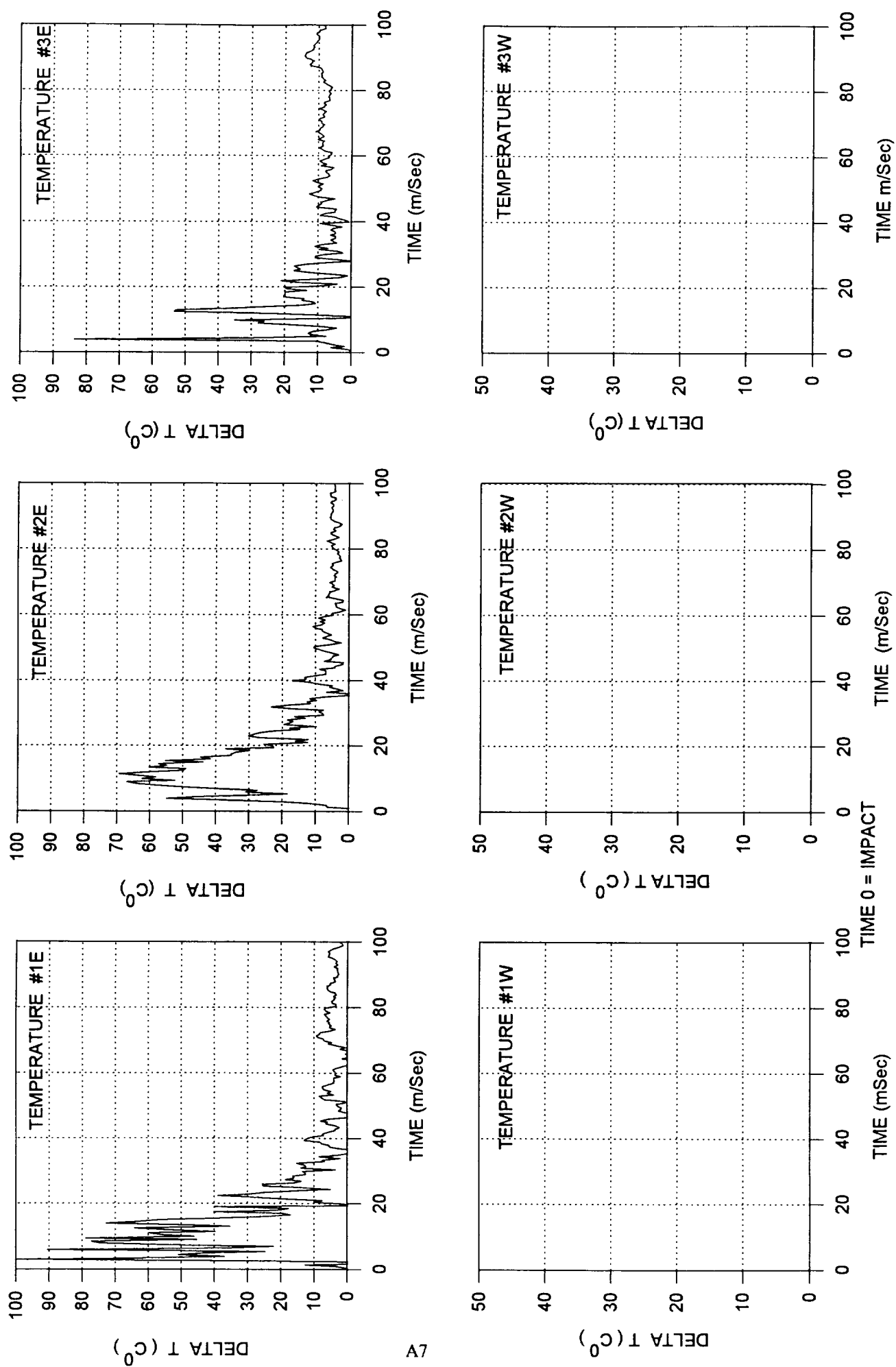
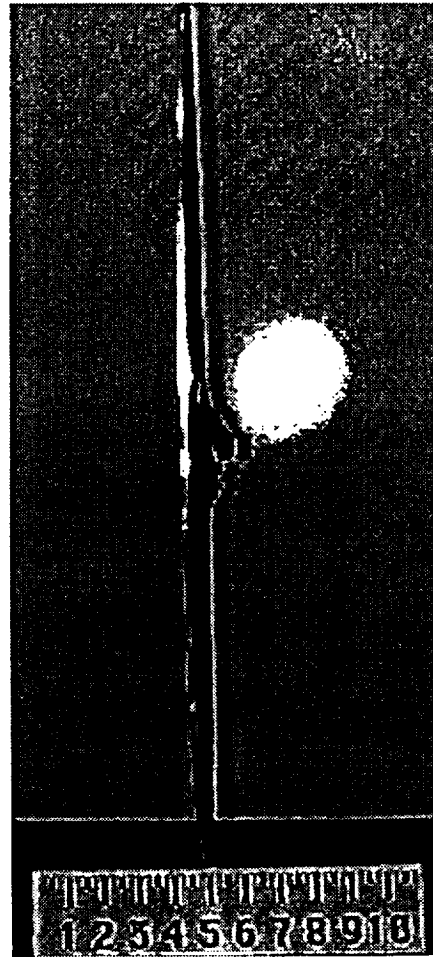


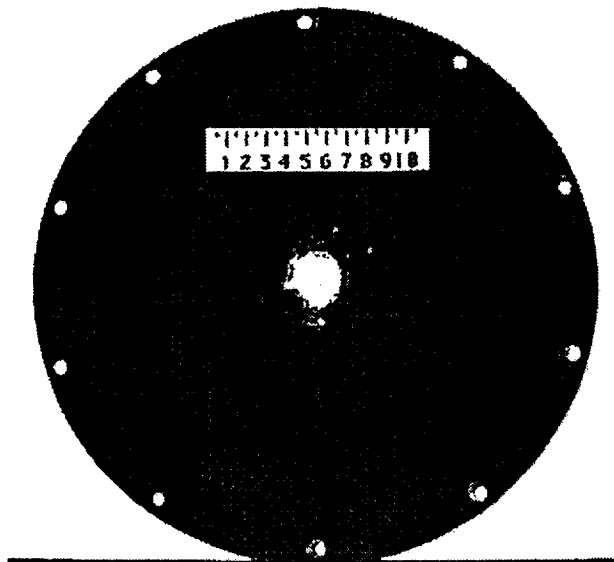
Figure A7 Temperature Profiles - Test #2



Target Plate Front



Target Plate Side



Target Plate Back

Figure A8

Target Plate Photographs - Test #3

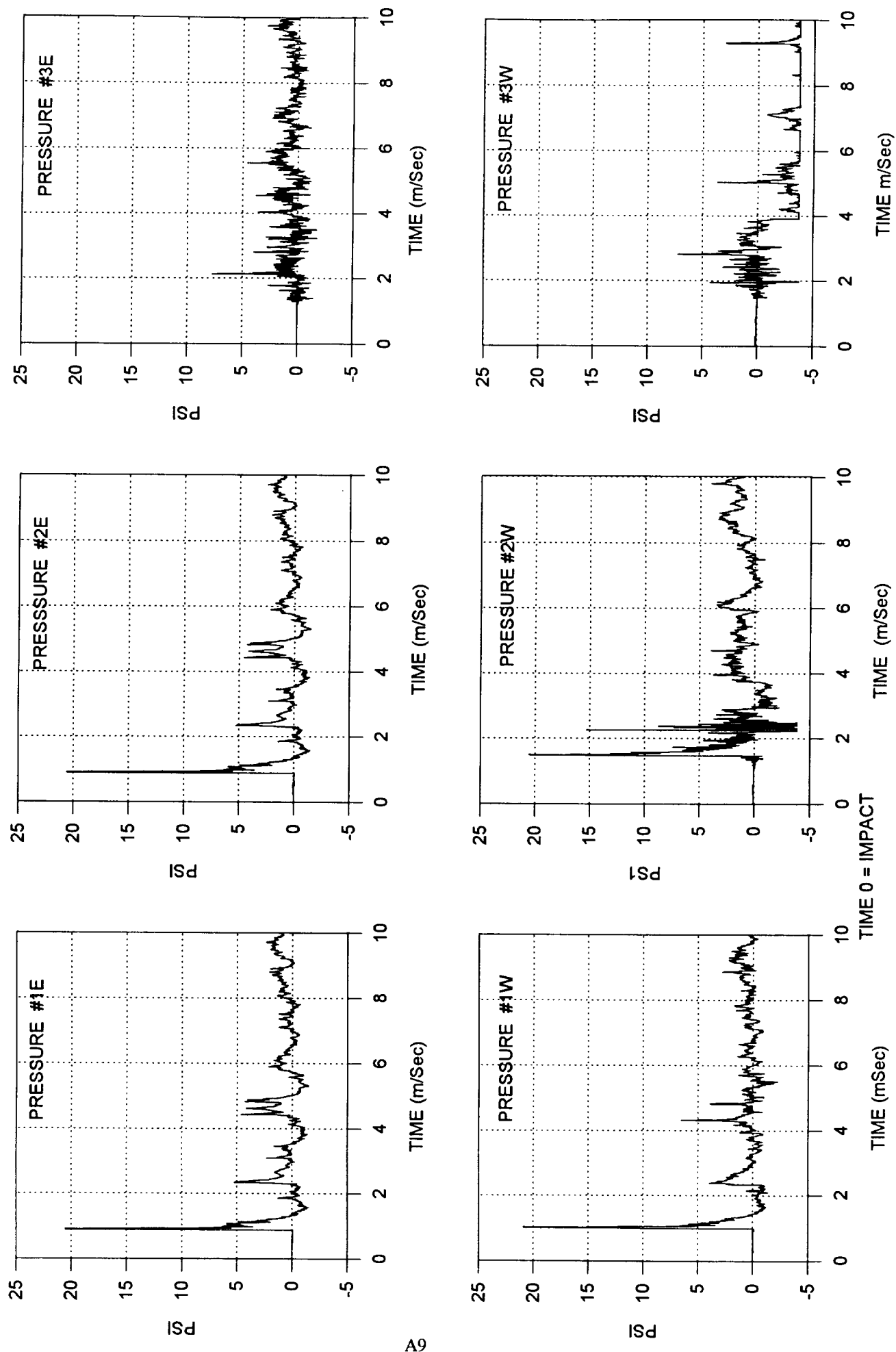


Figure A9 Pressure Profiles - Test #3

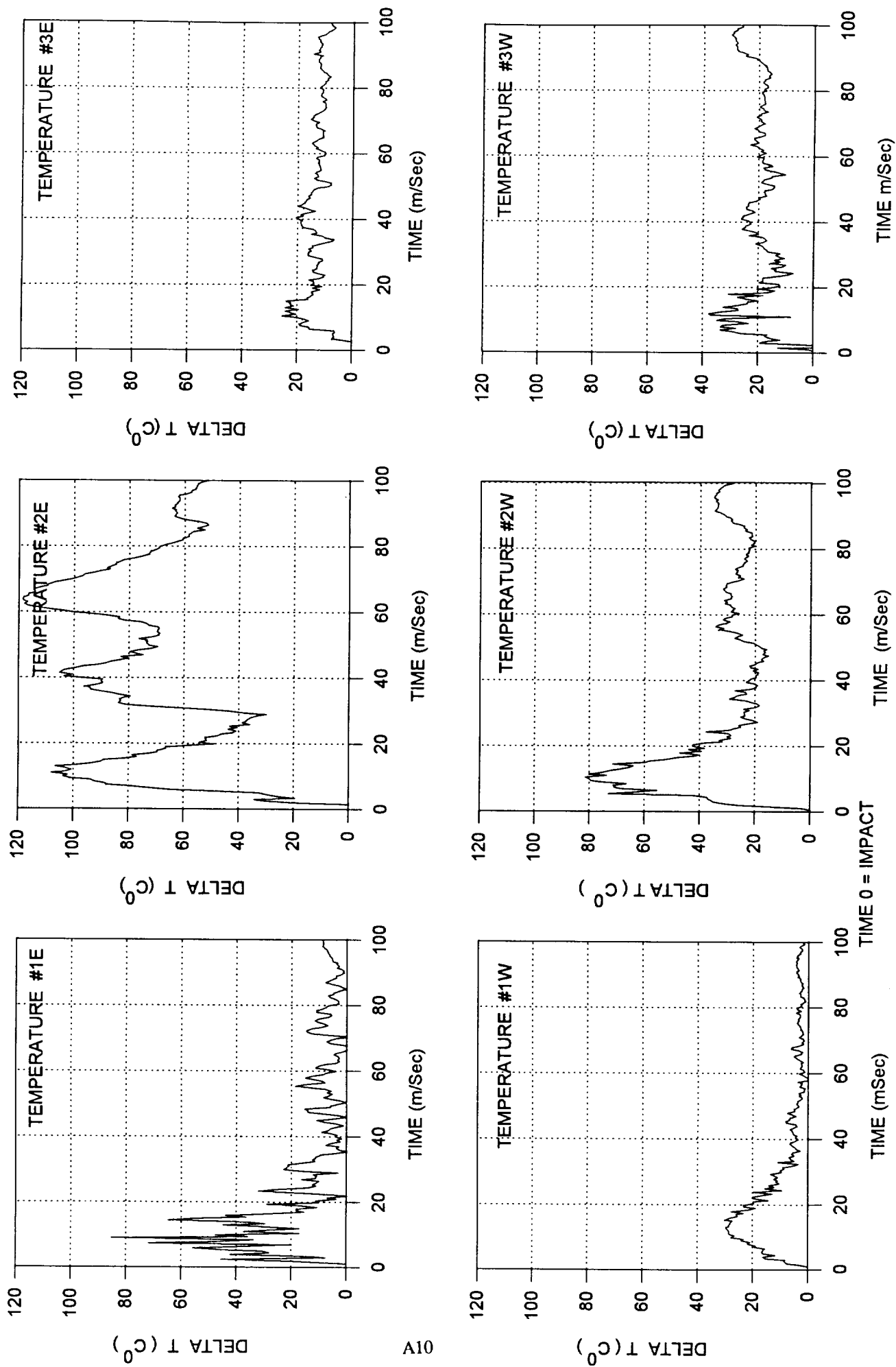


Figure A10 Temperature Profiles - Test #3

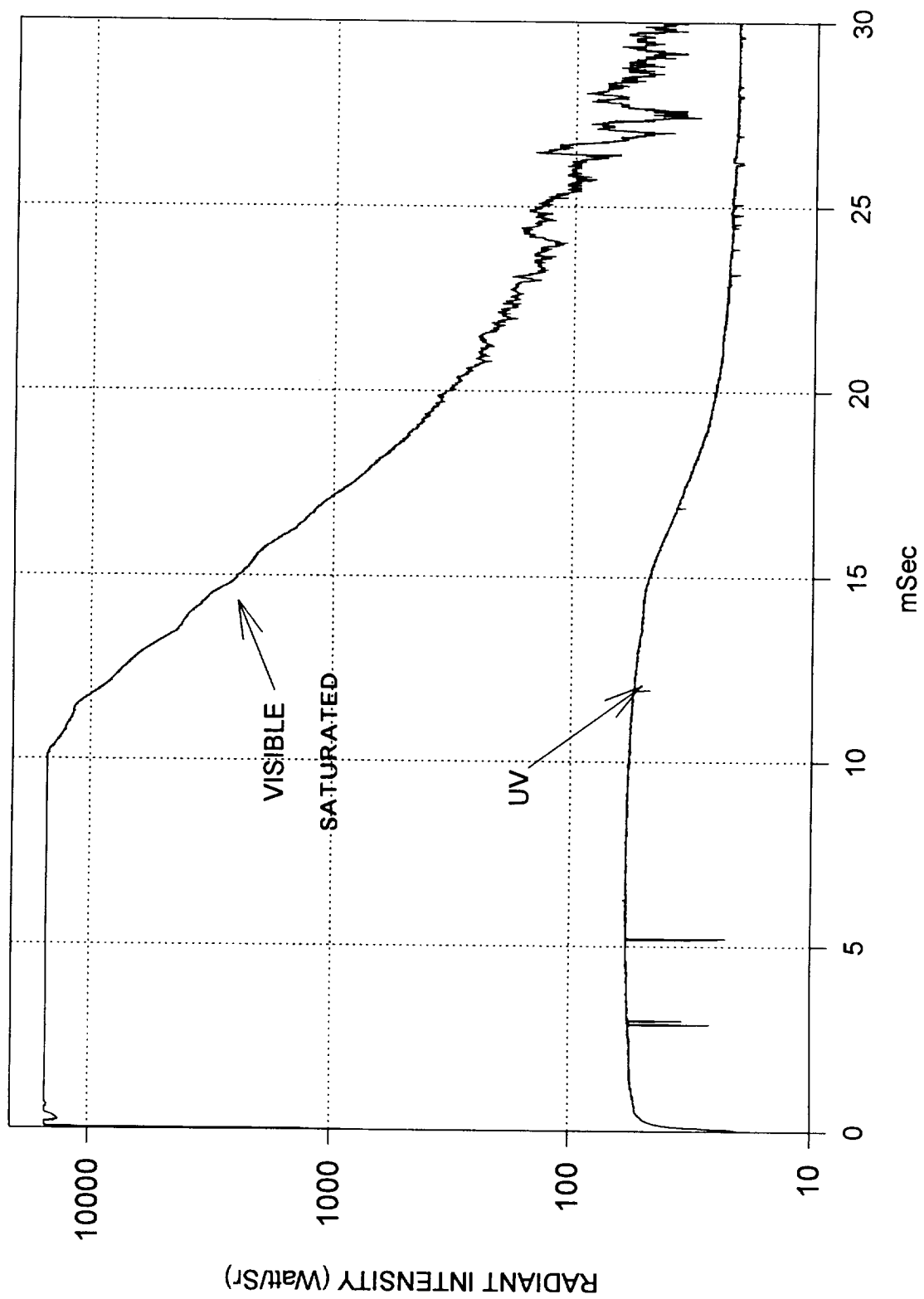
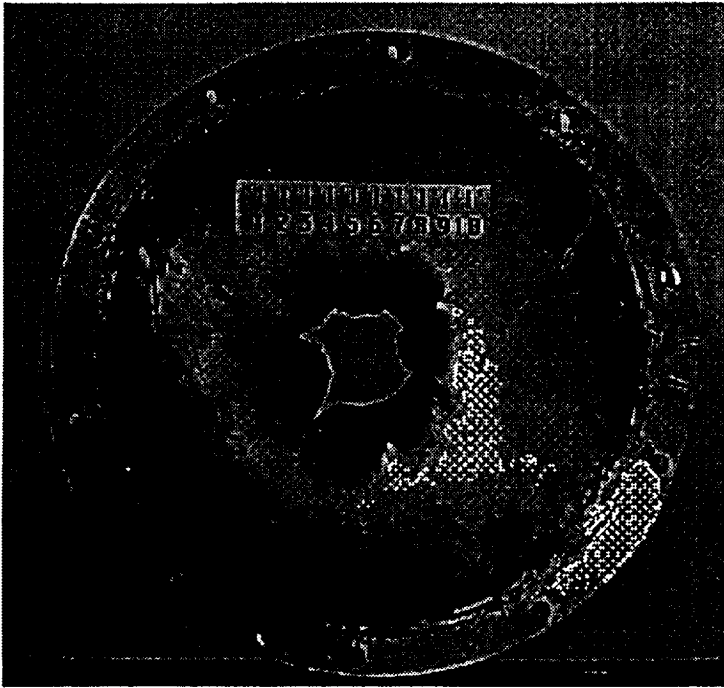
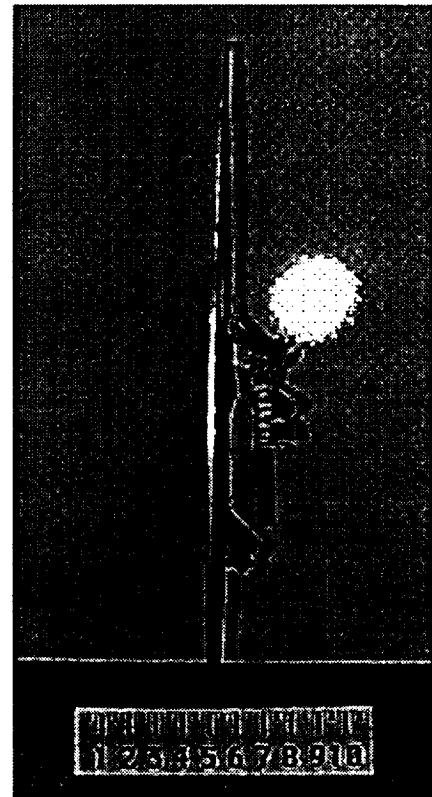


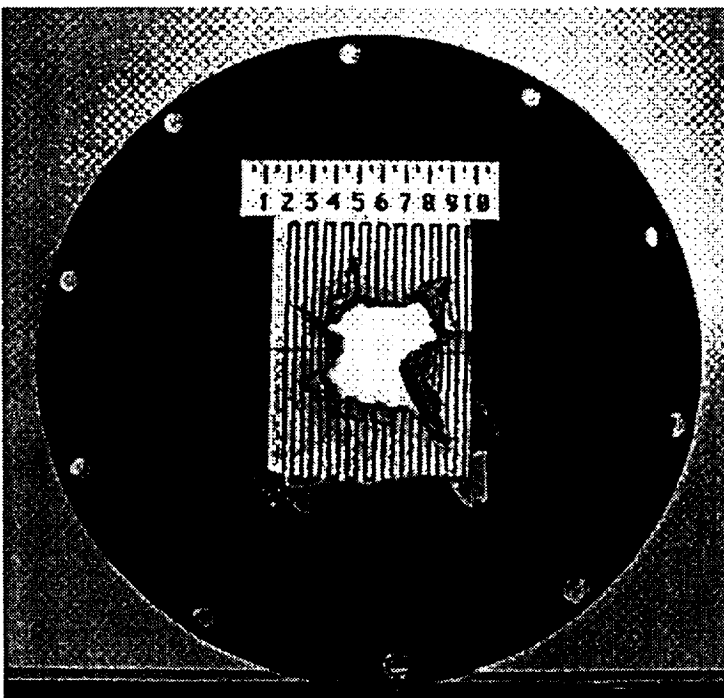
Figure A11 Radiometric Data - Test #3



Target Plate Front



Target Plate Side



Target Plate Back

Figure A12 Target Plate Photographs - Test #5

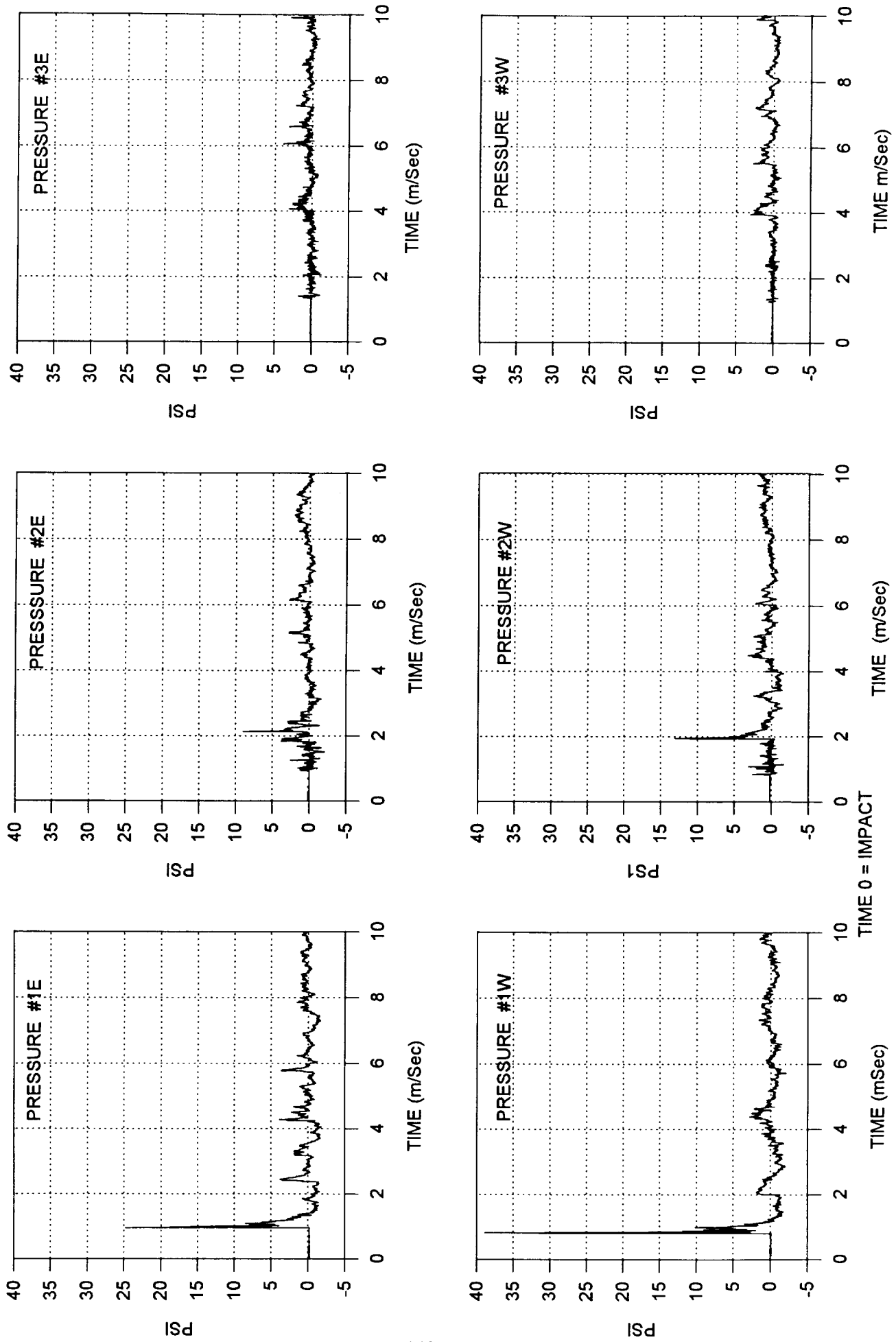


Figure A13 Pressure Profiles - Test #5

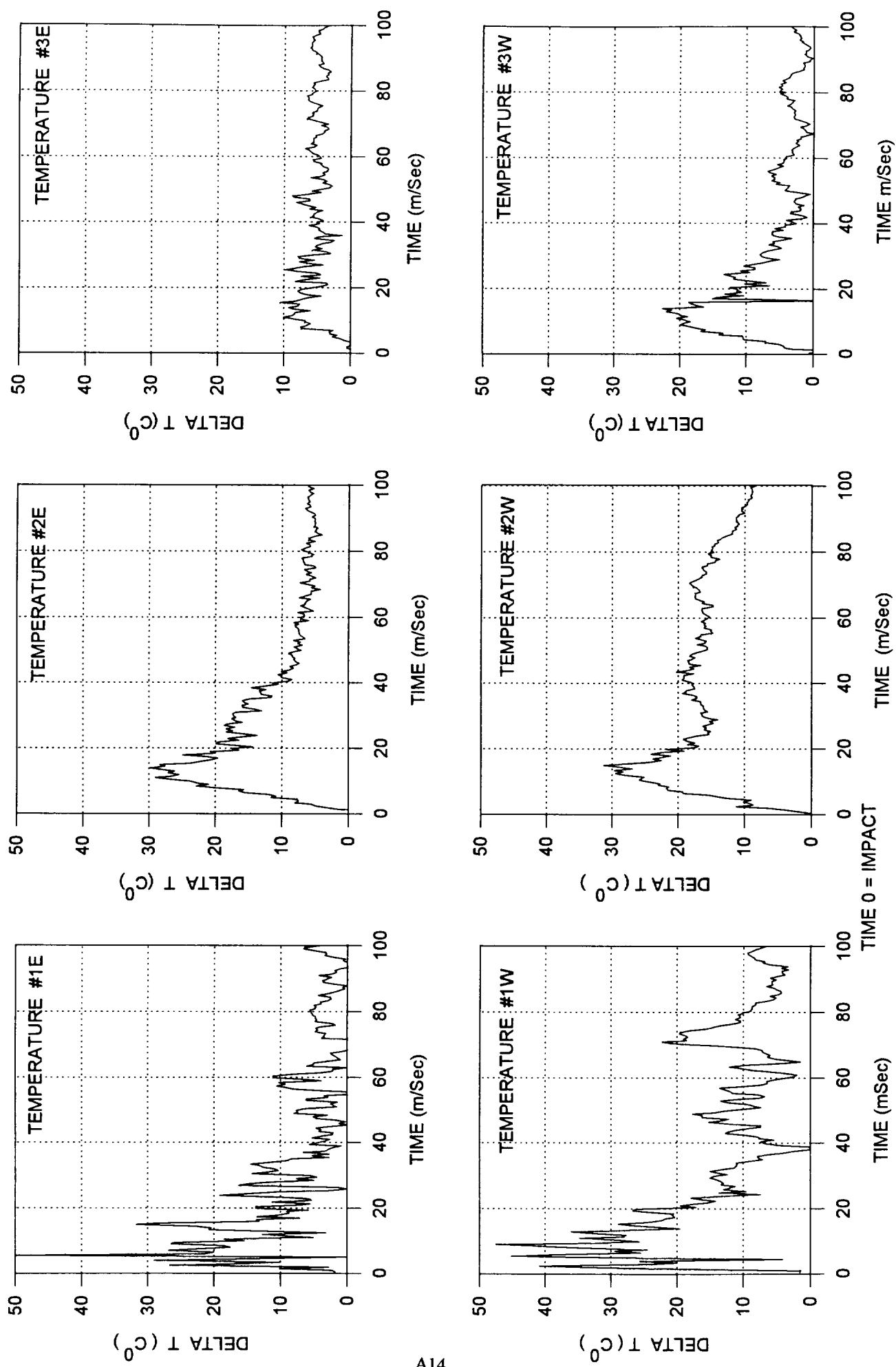


Figure A14 Temperature Profiles - Test #5

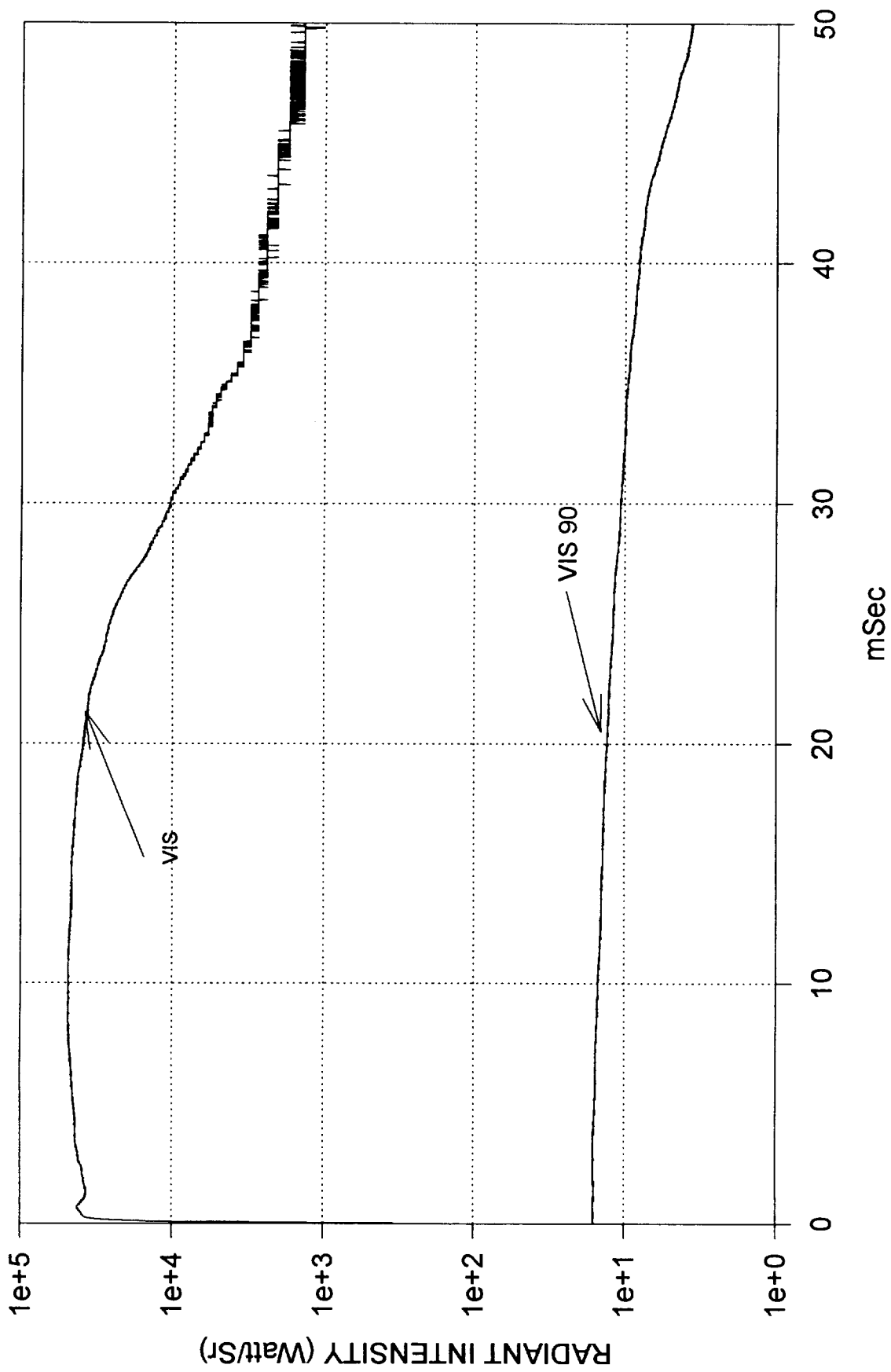
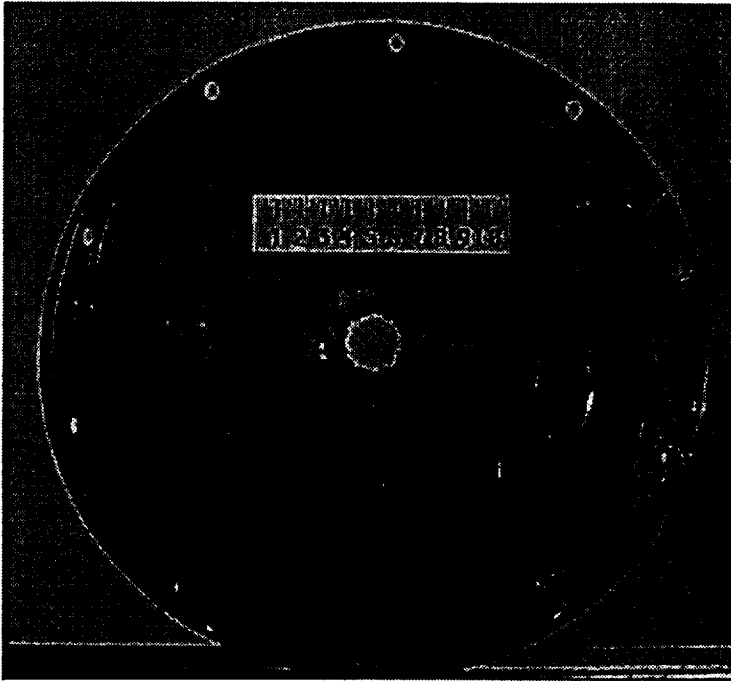
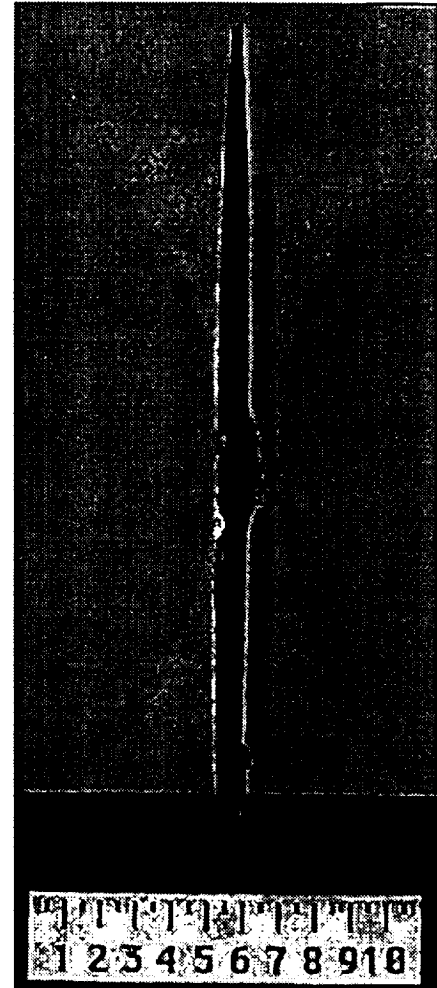


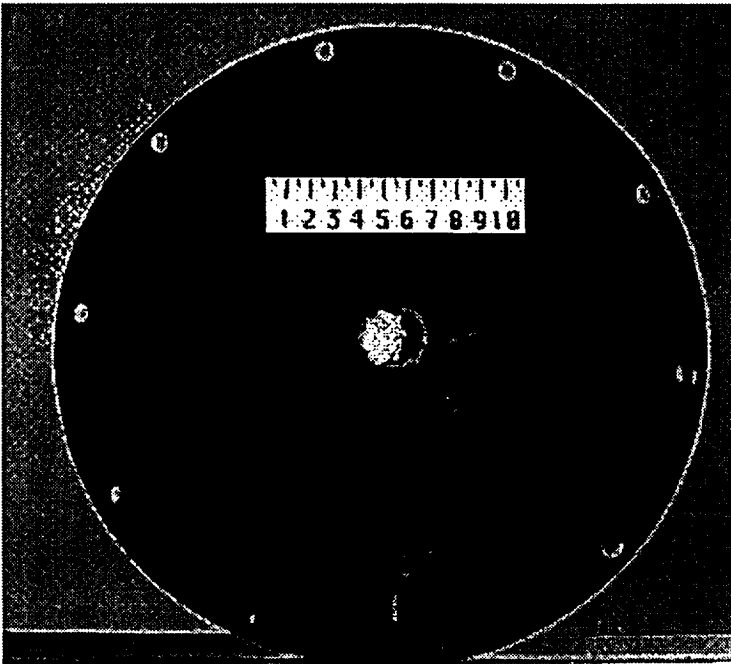
Figure A15 Radiometric Data - Test #5



Target Plate Front



Target Plate Side



Target Plate Back

Figure A16 Target Plate Photographs - Test #6

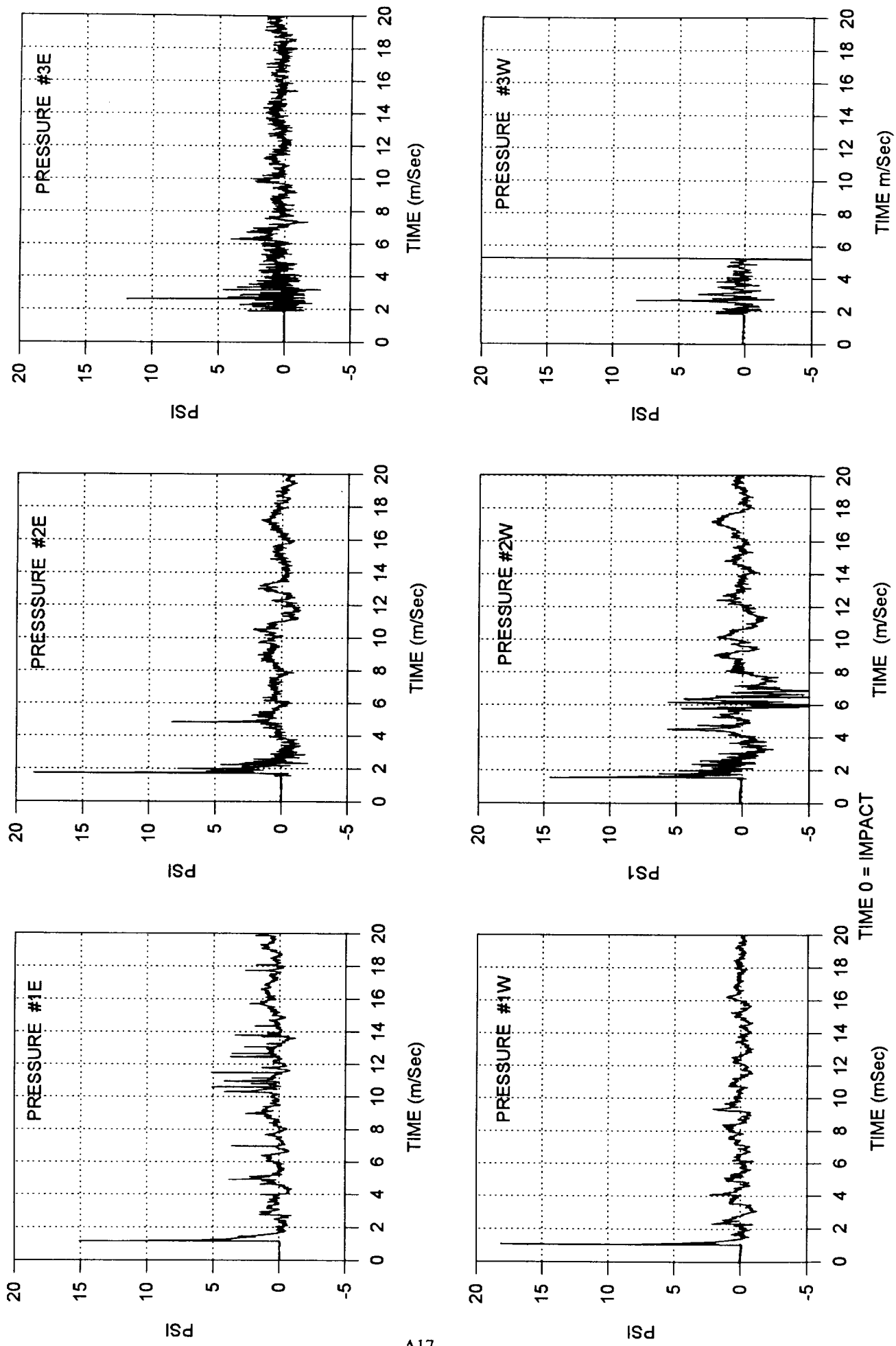


Figure A17 Pressure Profiles - Test #6

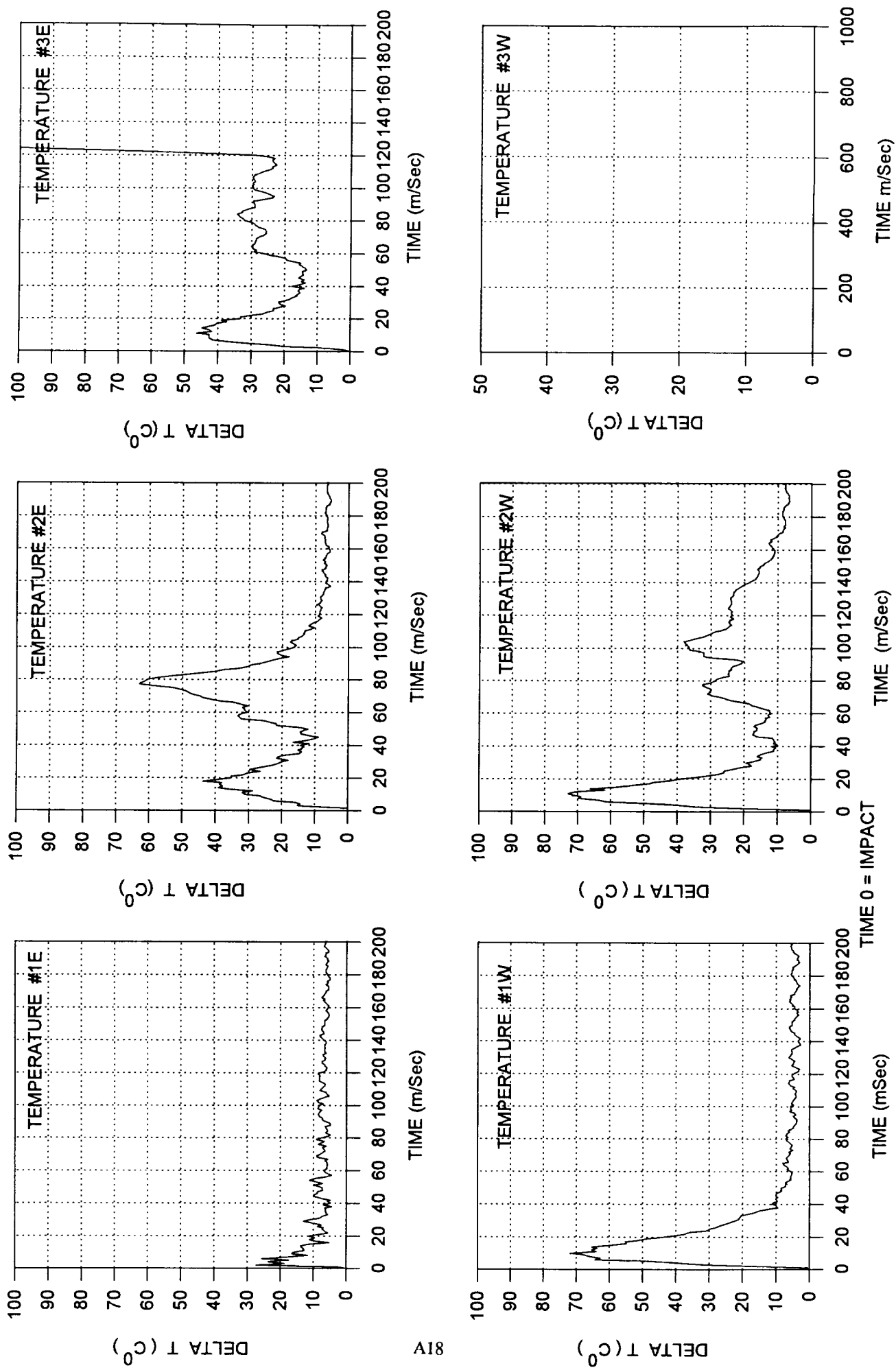


Figure A18 Temperature Profiles - Test #6

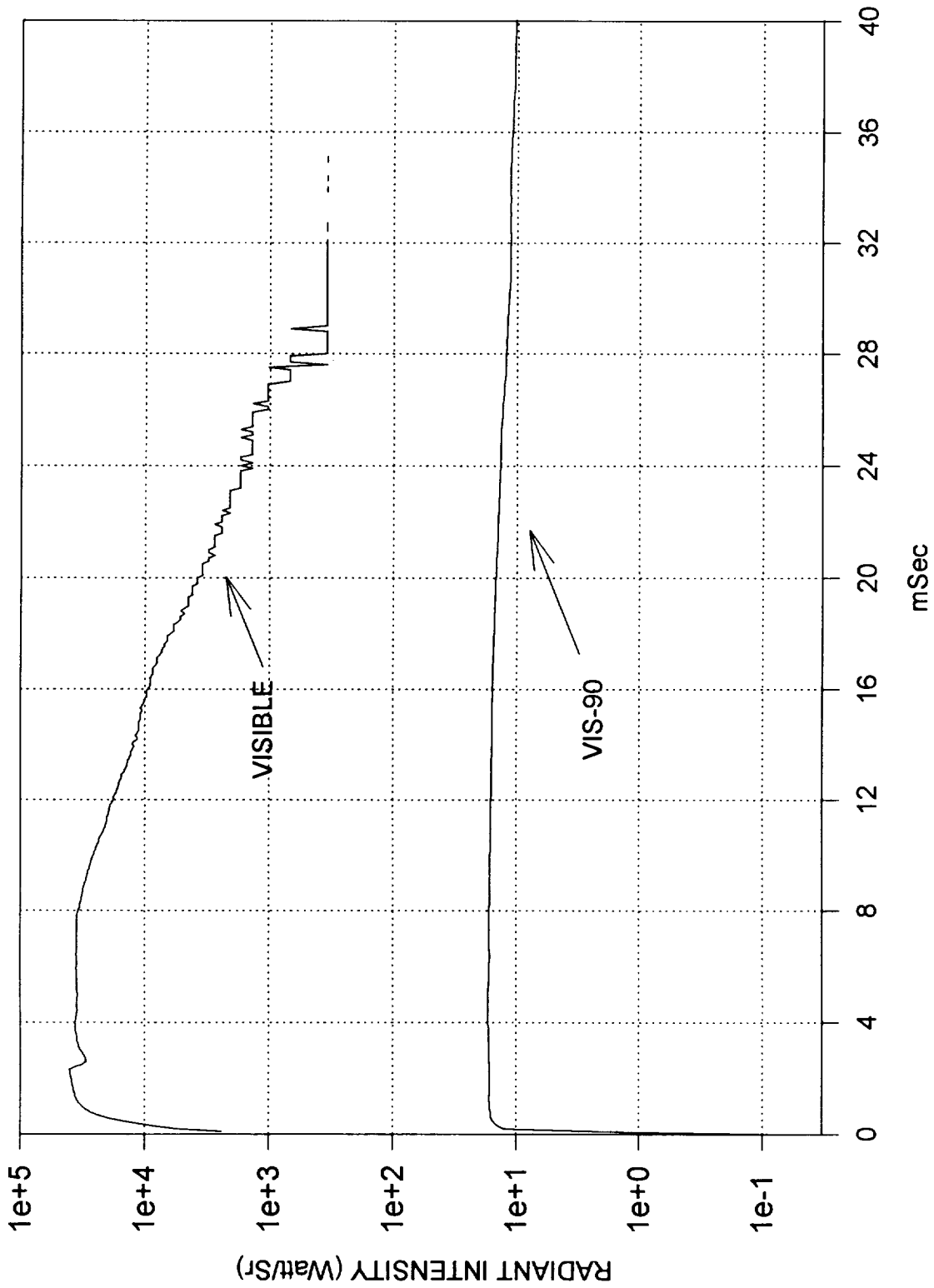
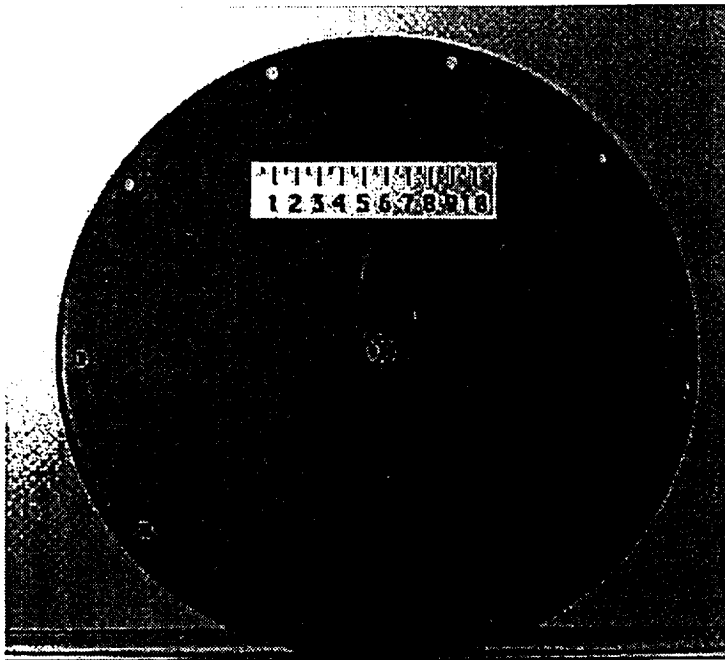
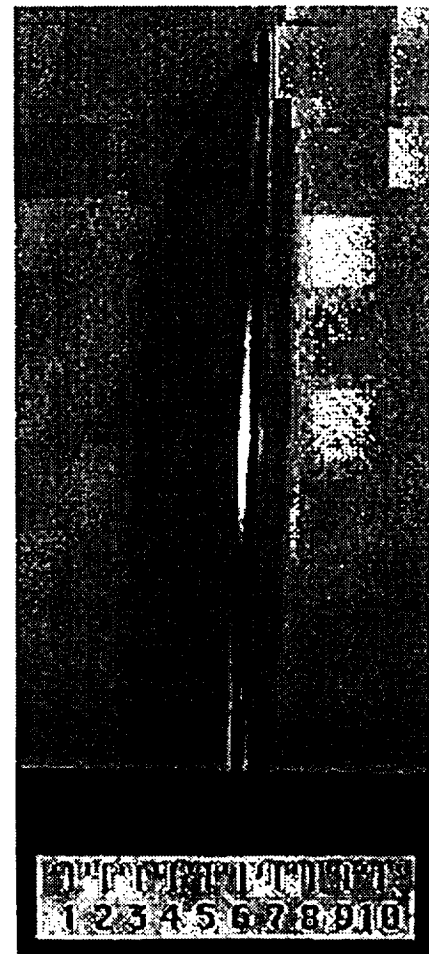


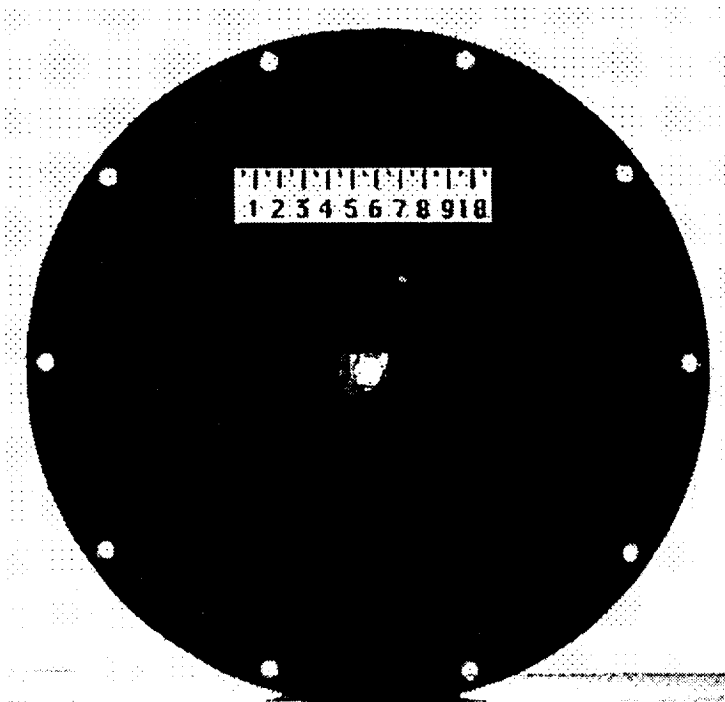
Figure A19 Radiometric Data - Test #6



Target Plate Front



Target Plate Side



Target Plate Back

Figure A20 Target Plate Photographs - Test #8

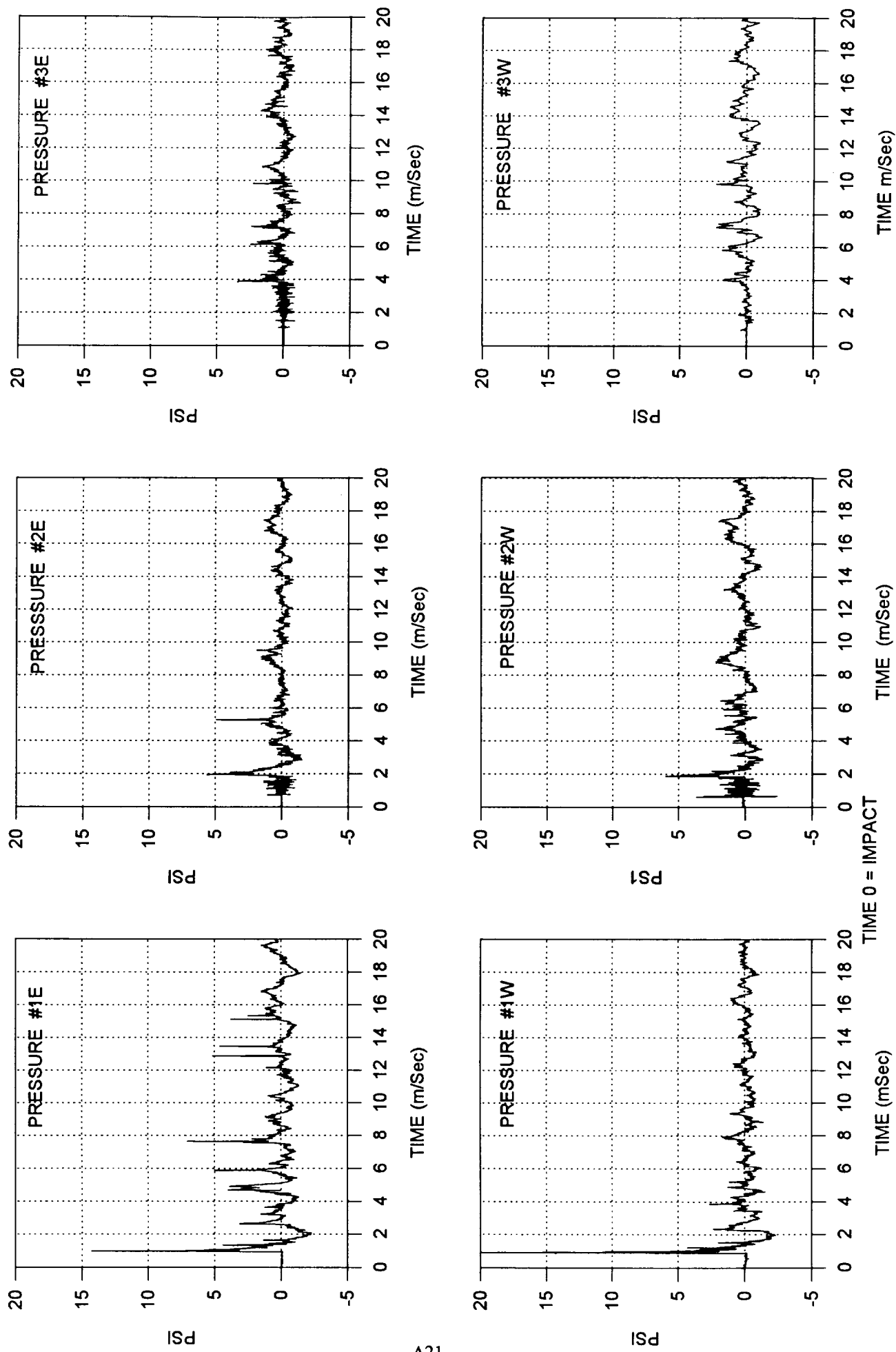


Figure A21 Pressure Profiles - Test #8

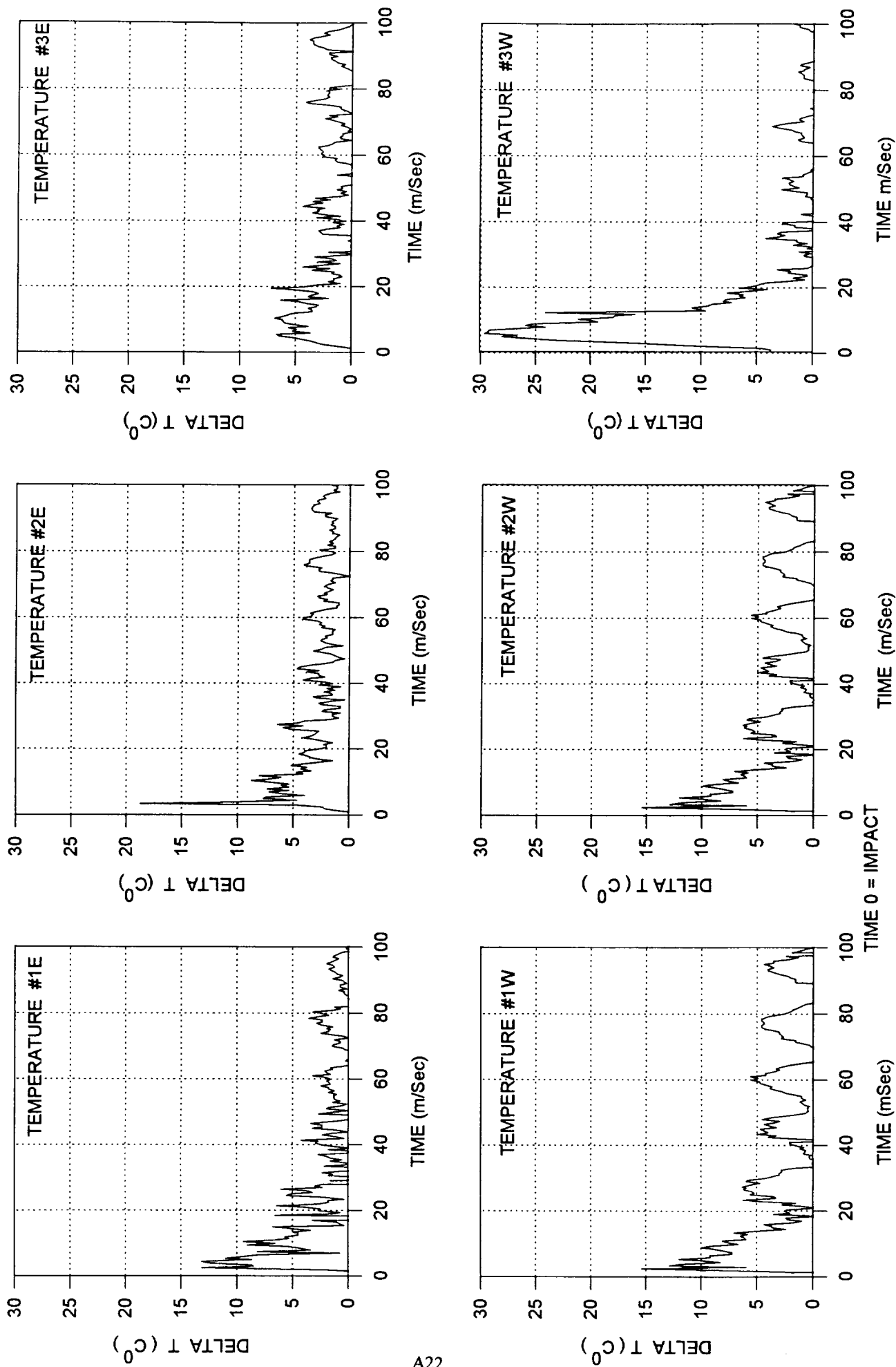


Figure A22 Temperature Profiles - Test #8

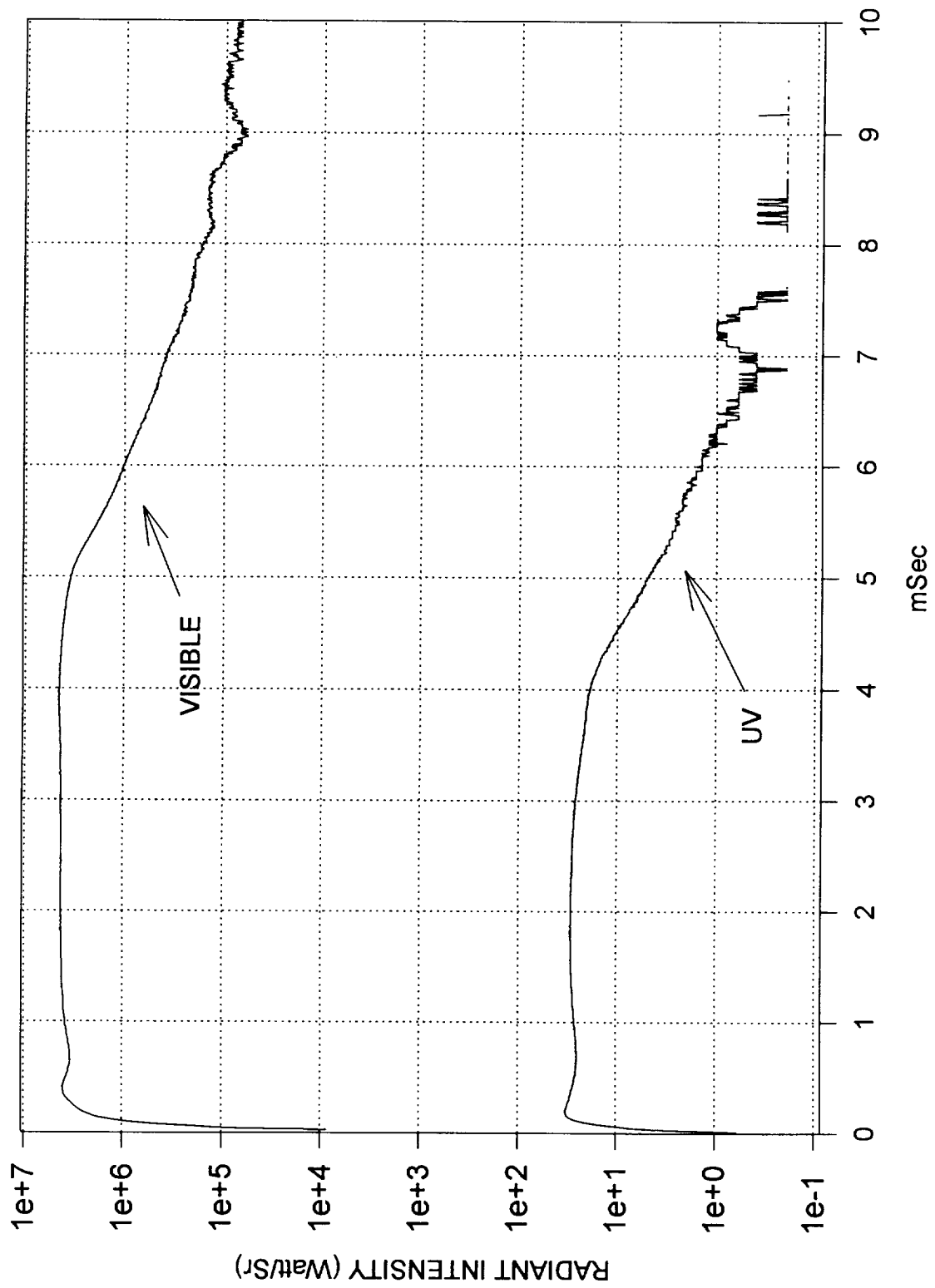
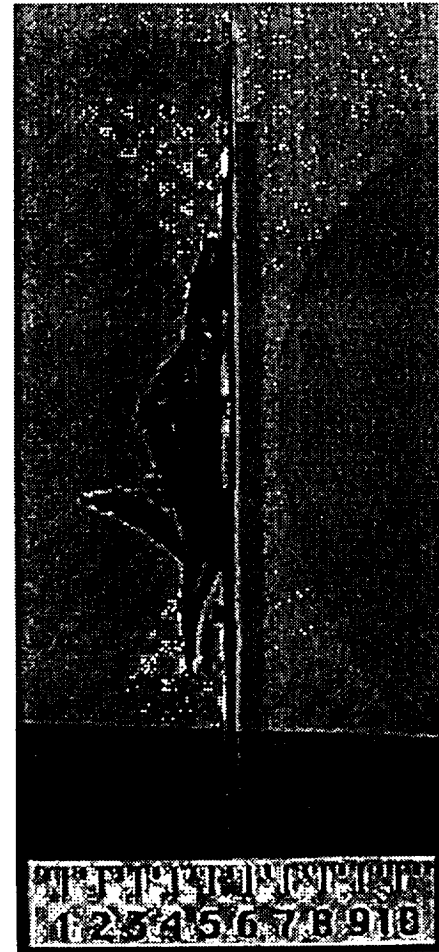


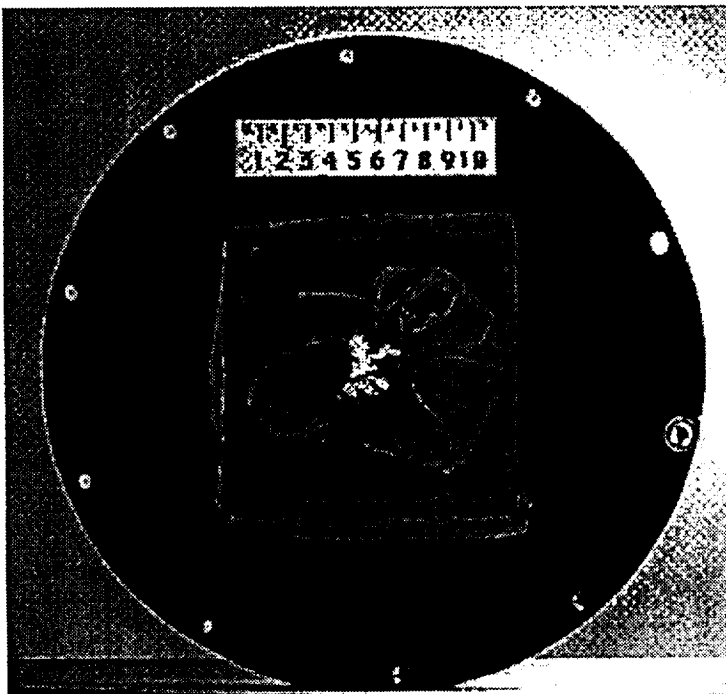
Figure A23 Radiometric Data - Test #8



Target Plate Front



Target Plate Side



Target Plate Back

Figure A24 Target Plate Photographs - Test #9

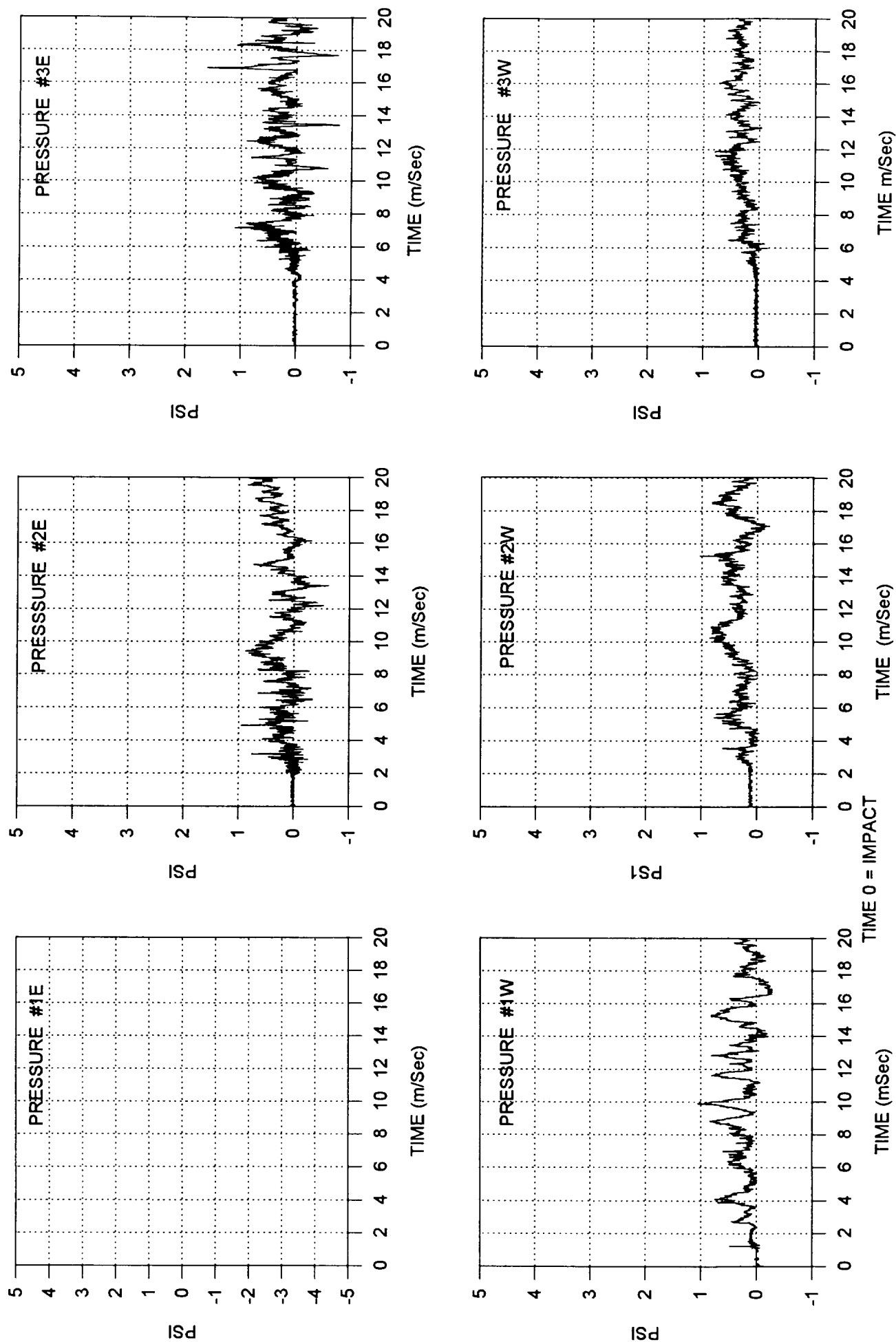


Figure A25 Pressure Profiles - Test #9

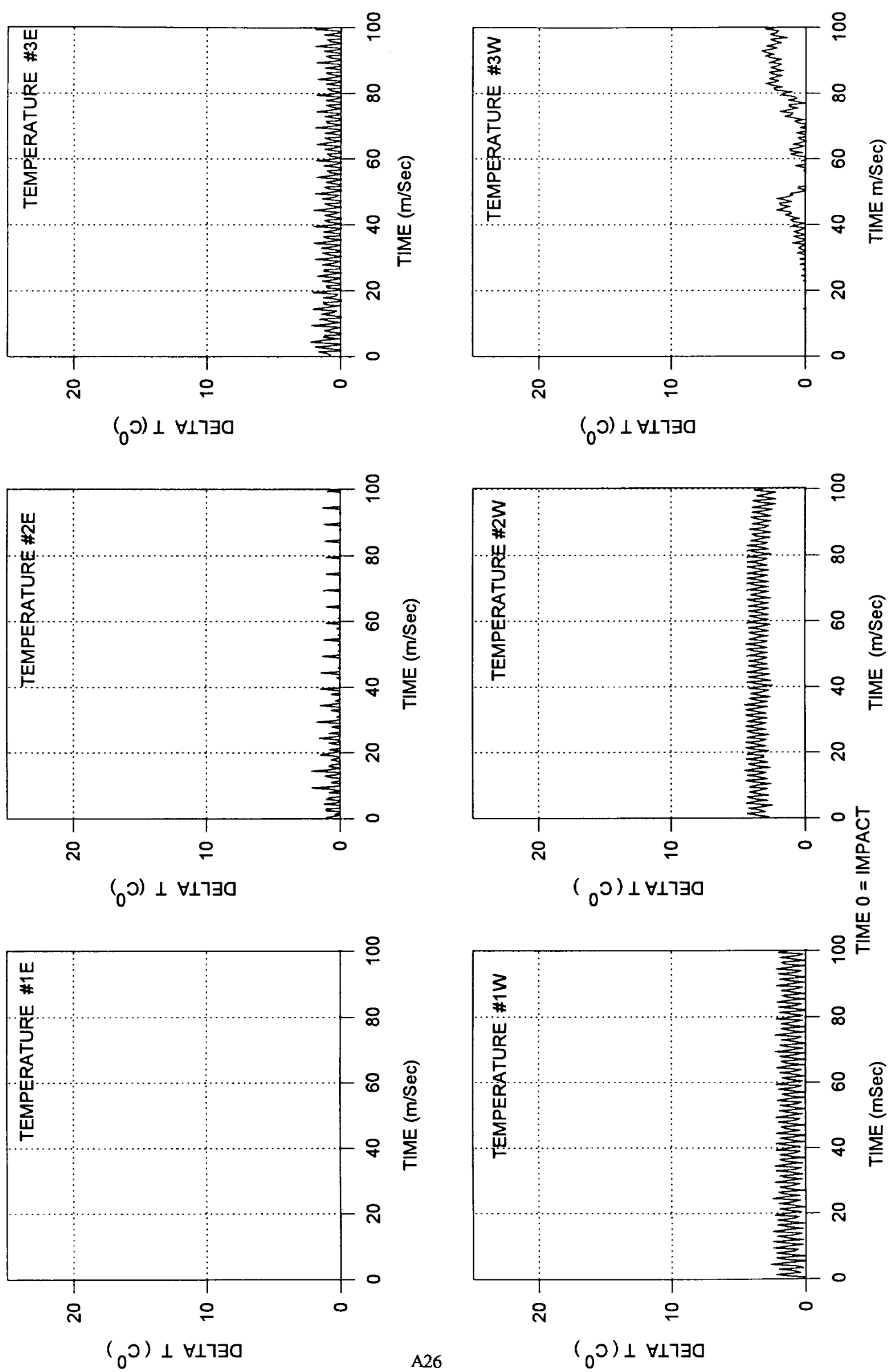


Figure A26 Temperature Profiles - Test #9

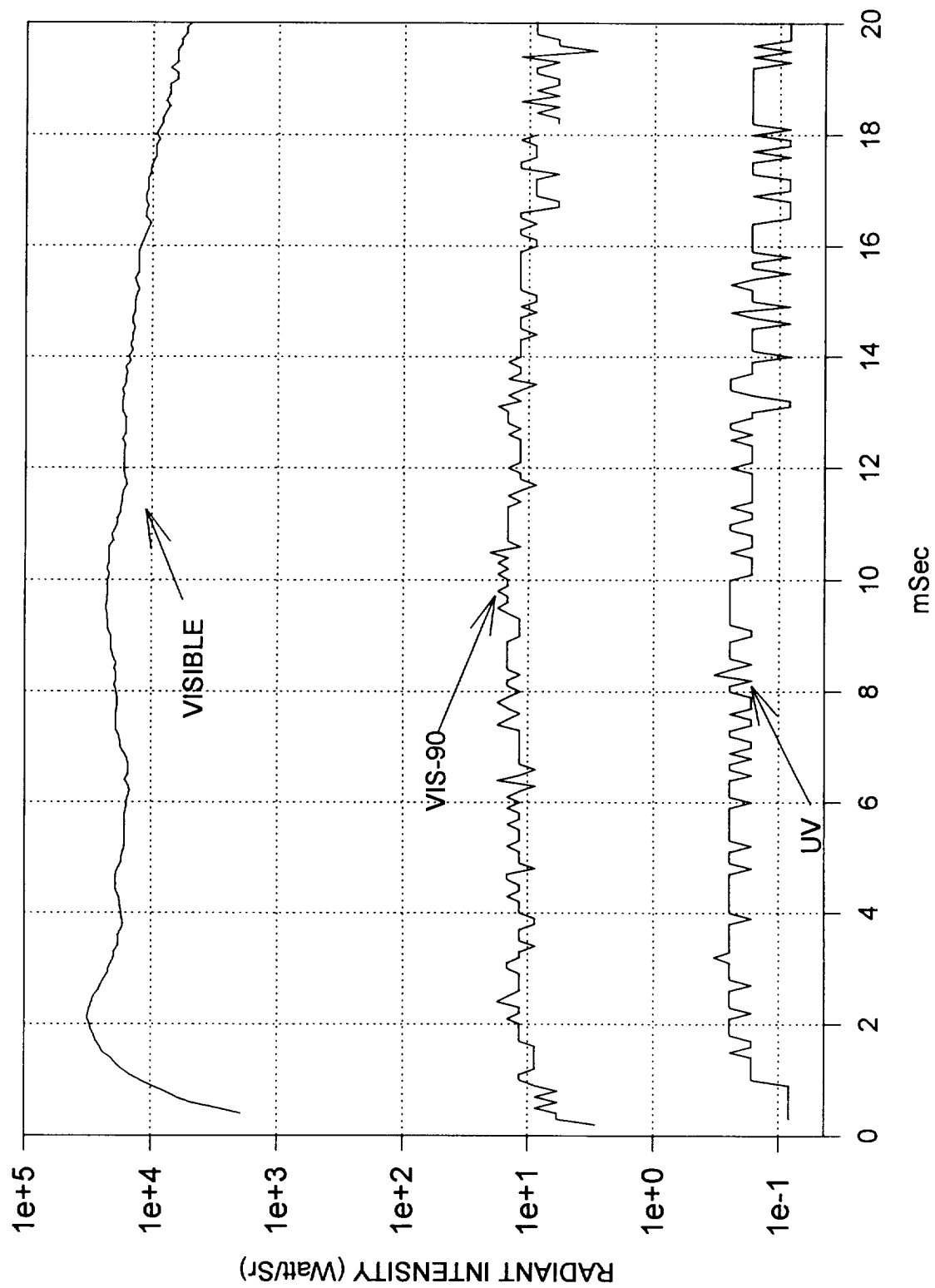
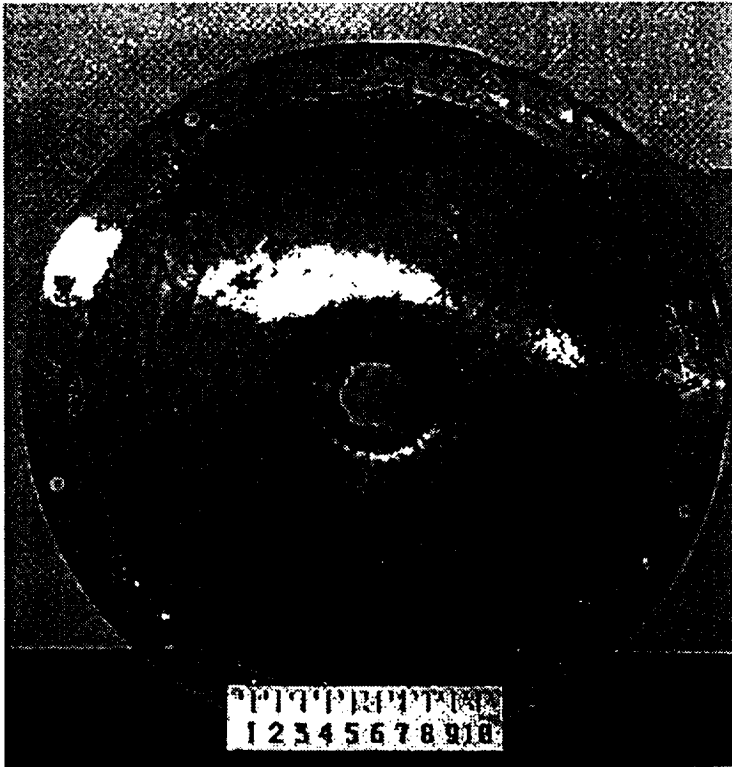
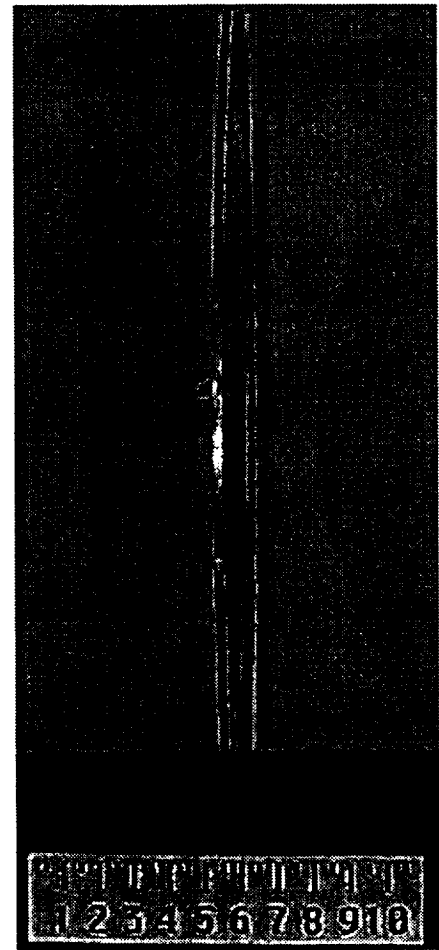


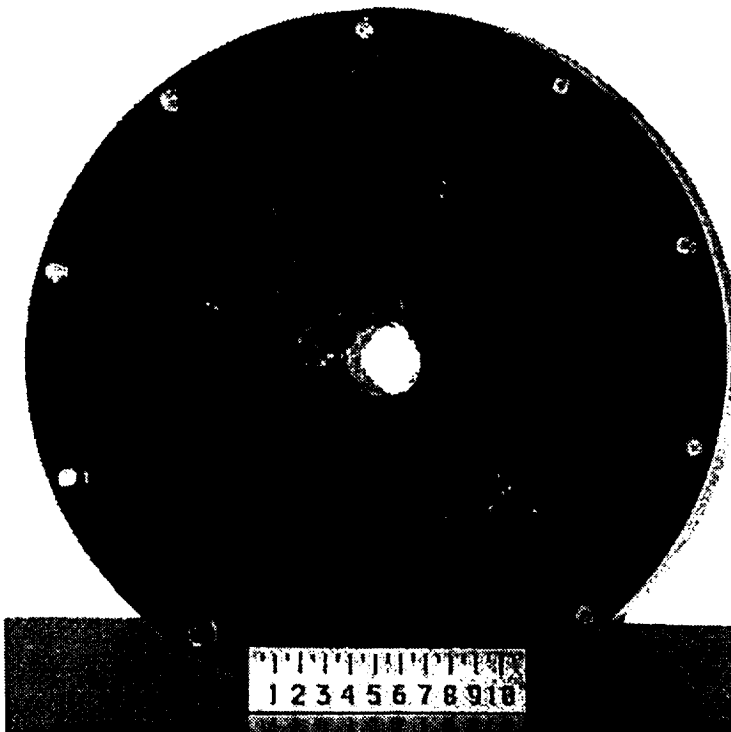
Figure A27 Radiometric Data - Test #9



Target Plate Front

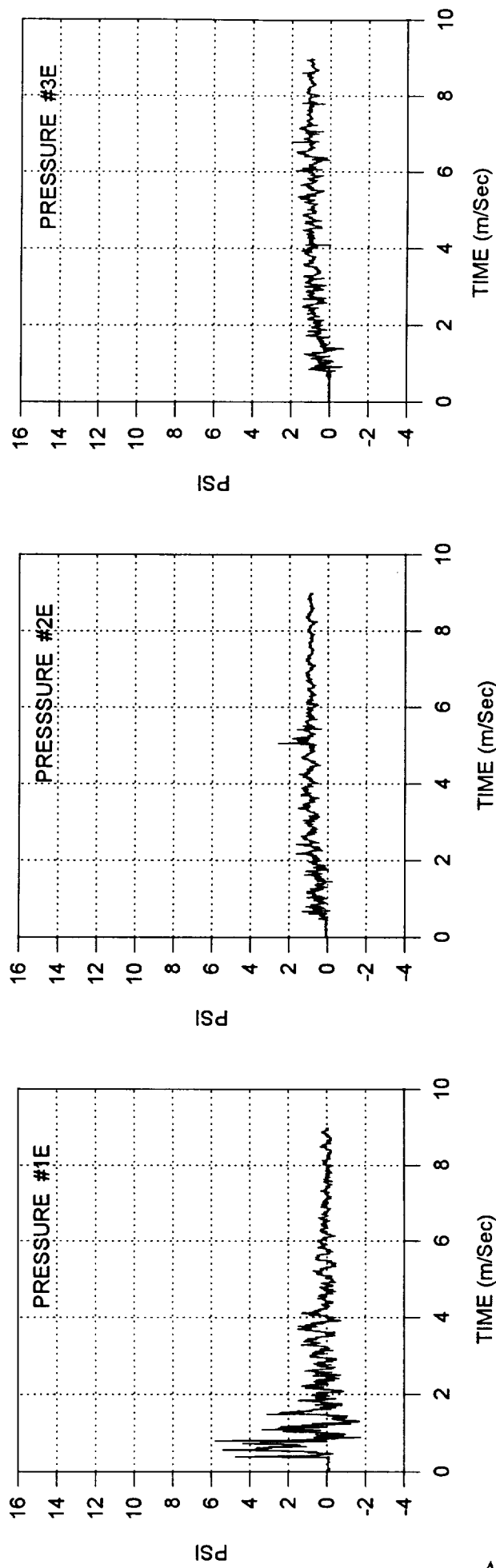


Target Plate Side



Target Plate Back

Figure A28 Target Plate Photographs - Test #10



A29

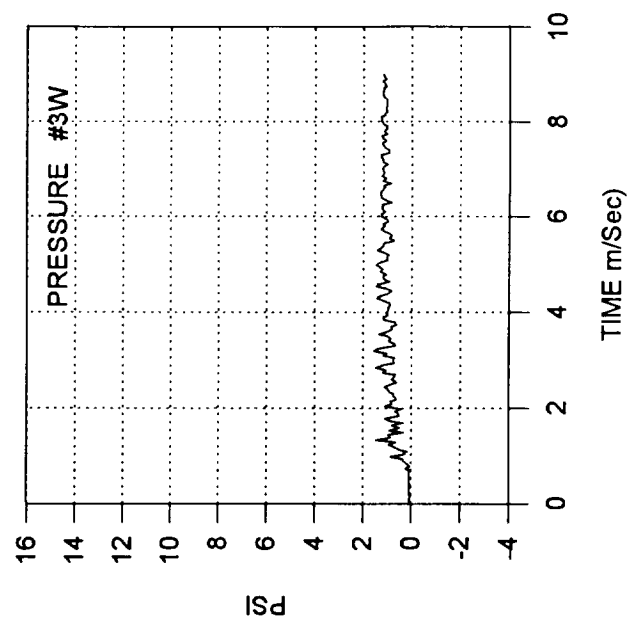
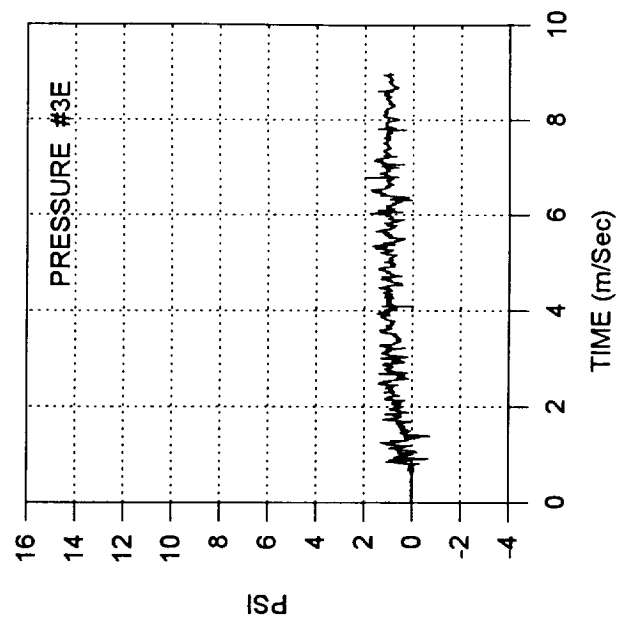
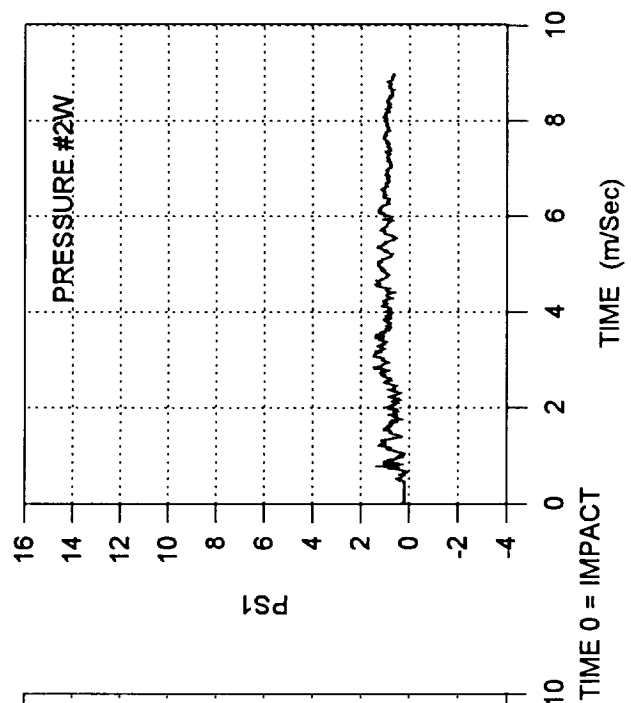
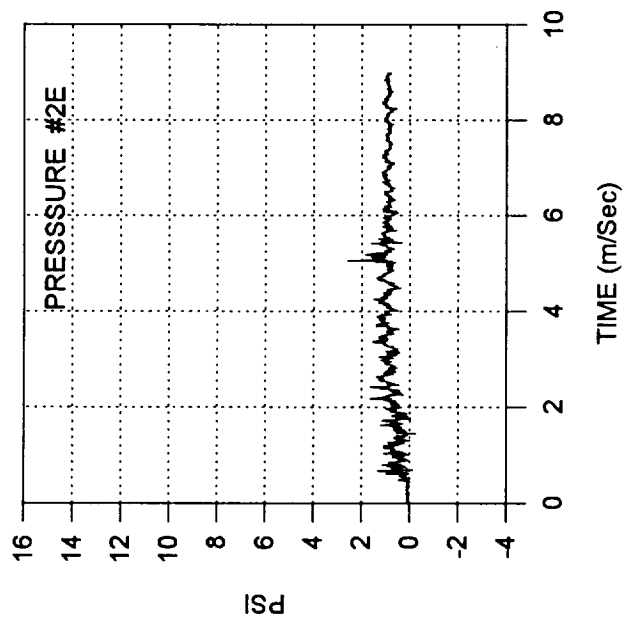
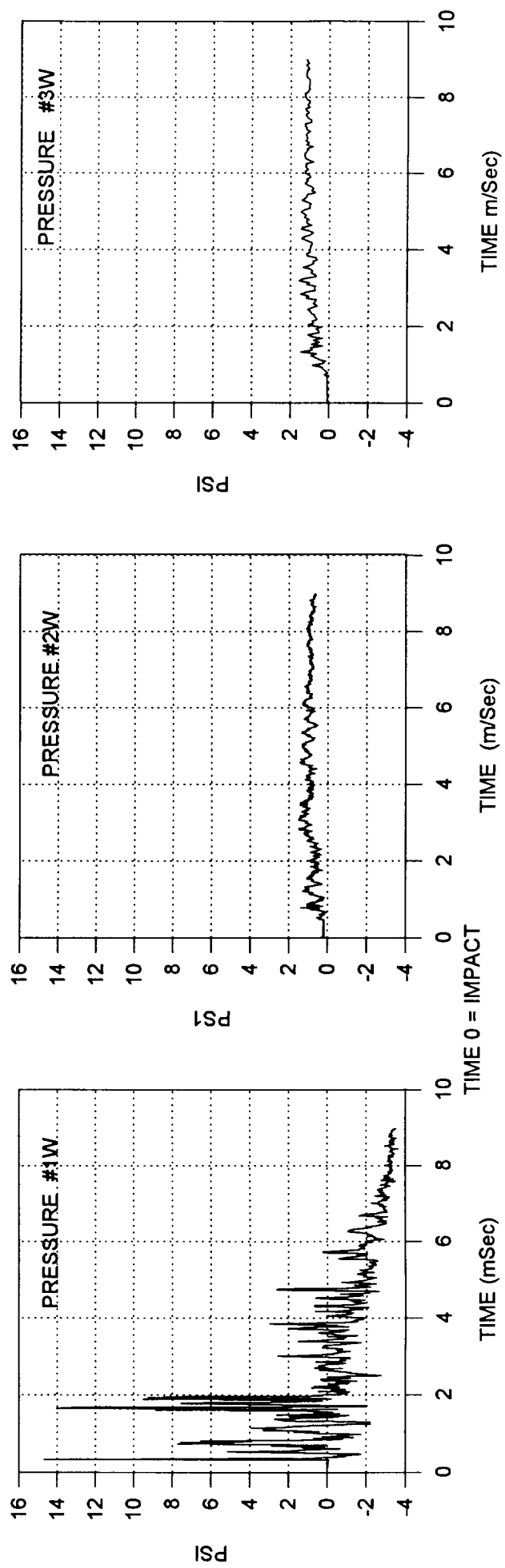


Figure A29 Pressure Profiles - Test #10

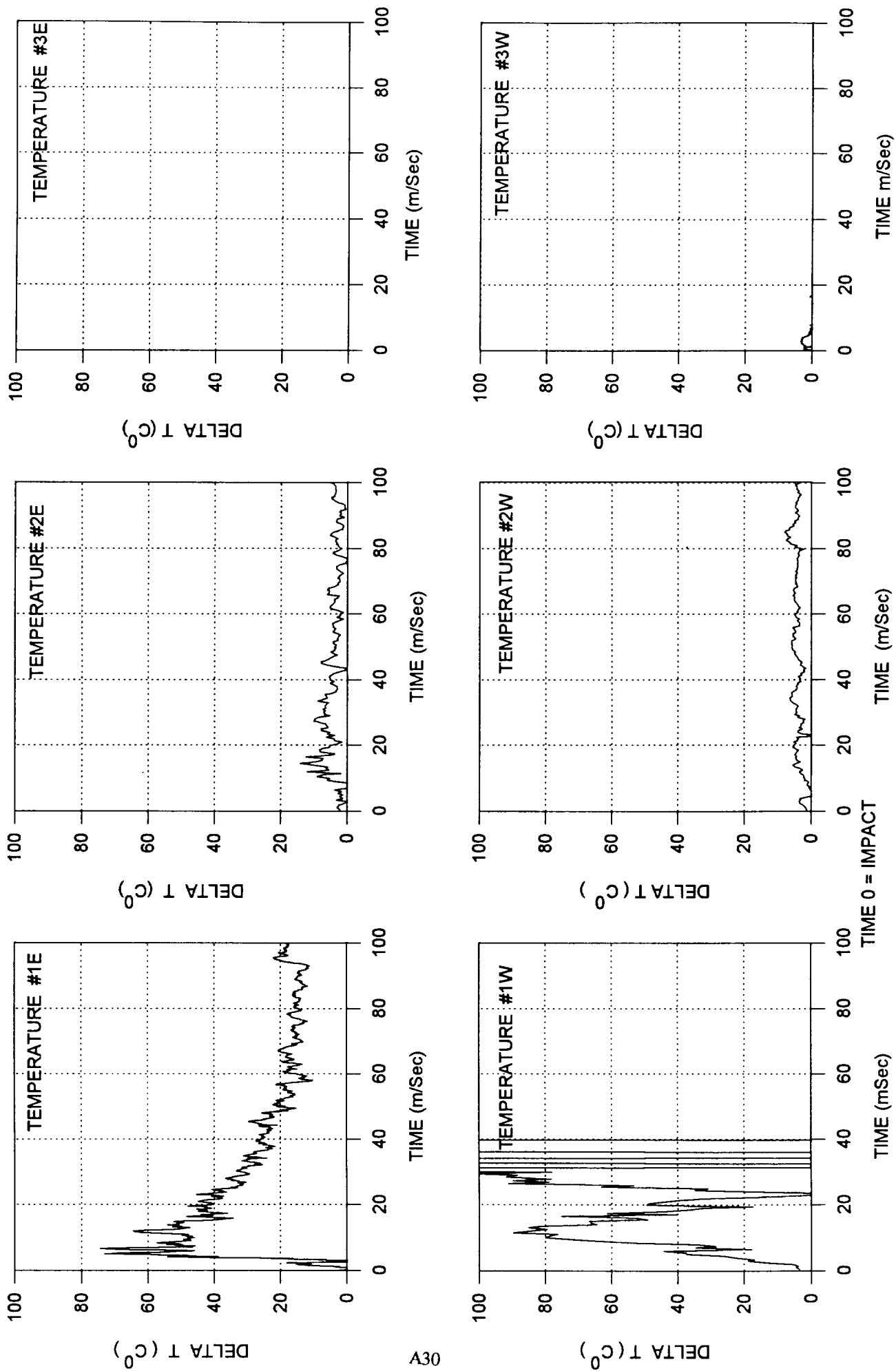


Figure A30 Temperature Profiles - Test #10

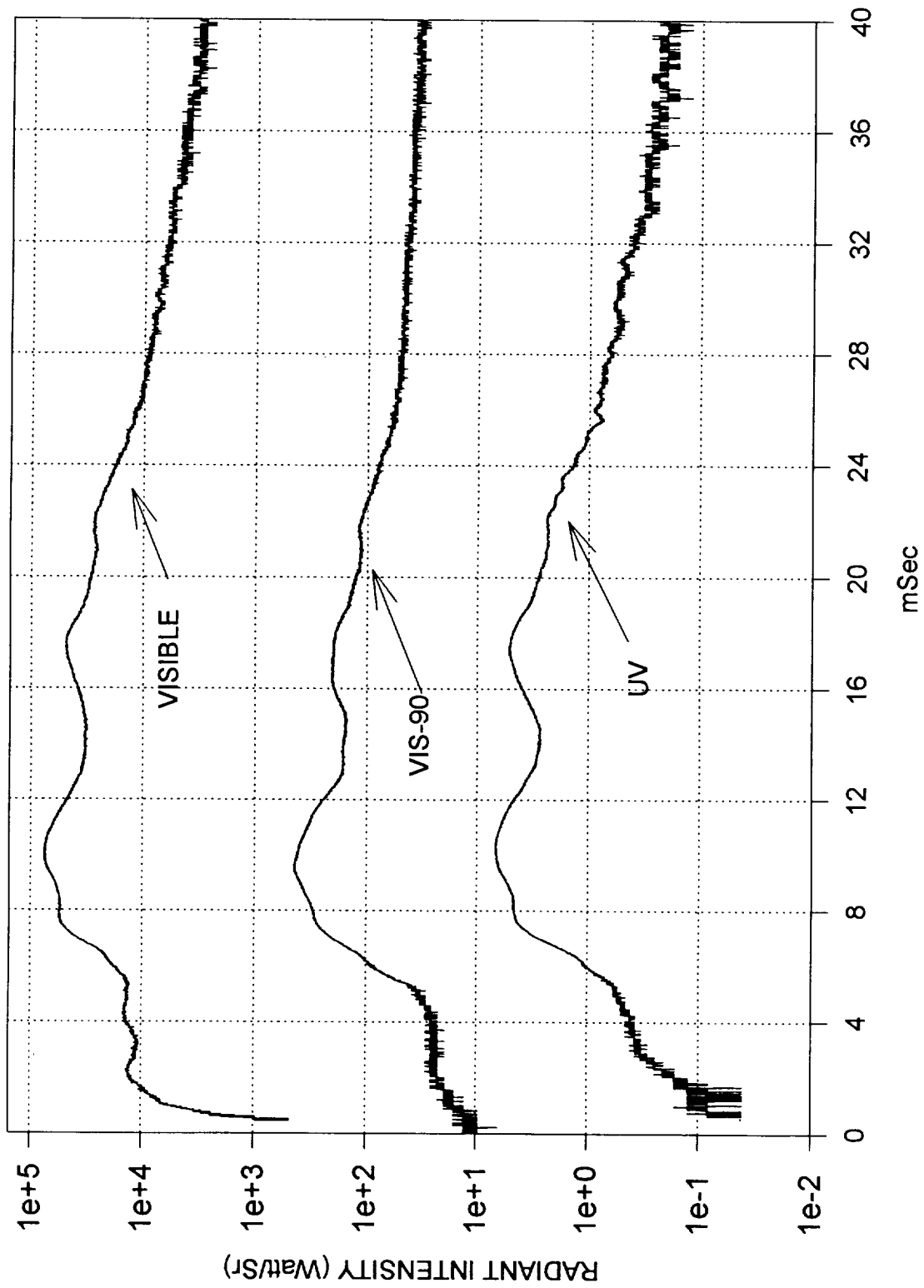
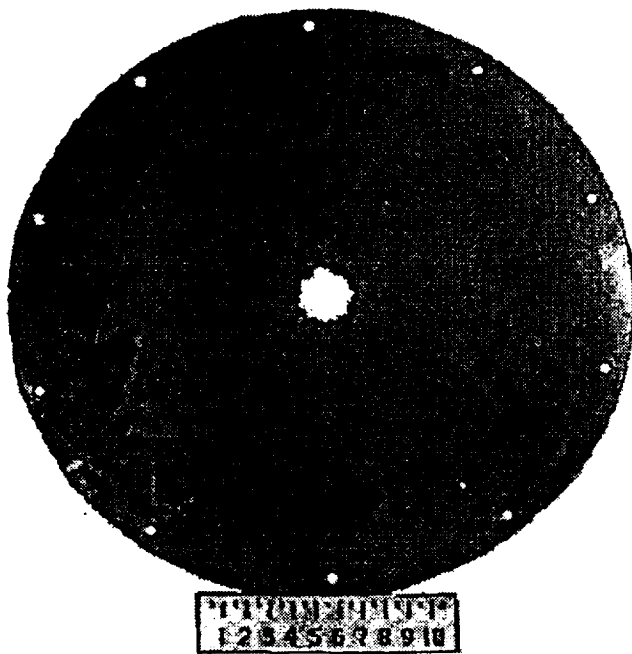
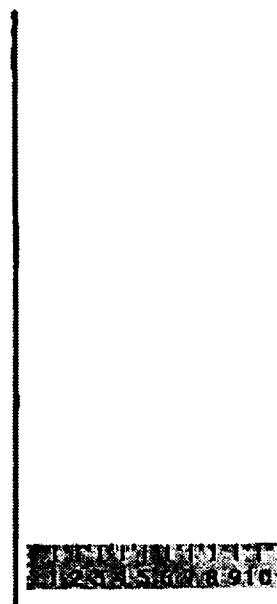


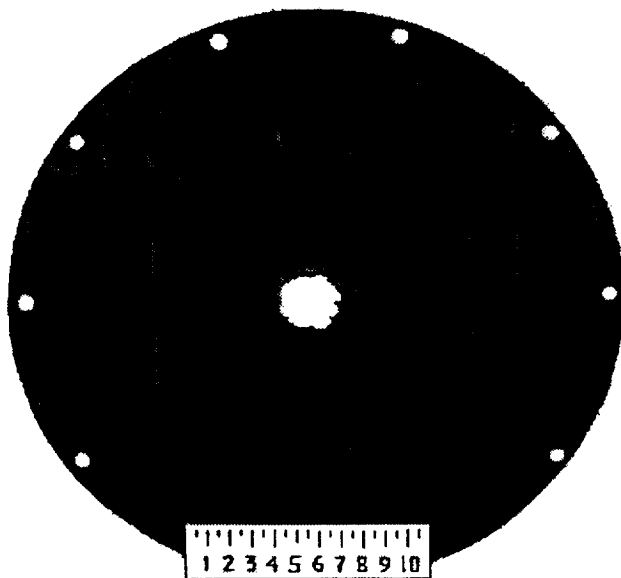
Figure A31 Radiometric Data - Test #10



Target Plate Front



Target Plate Side



Target Plate Back

Figure A32 Target Plate Photographs - Test #11

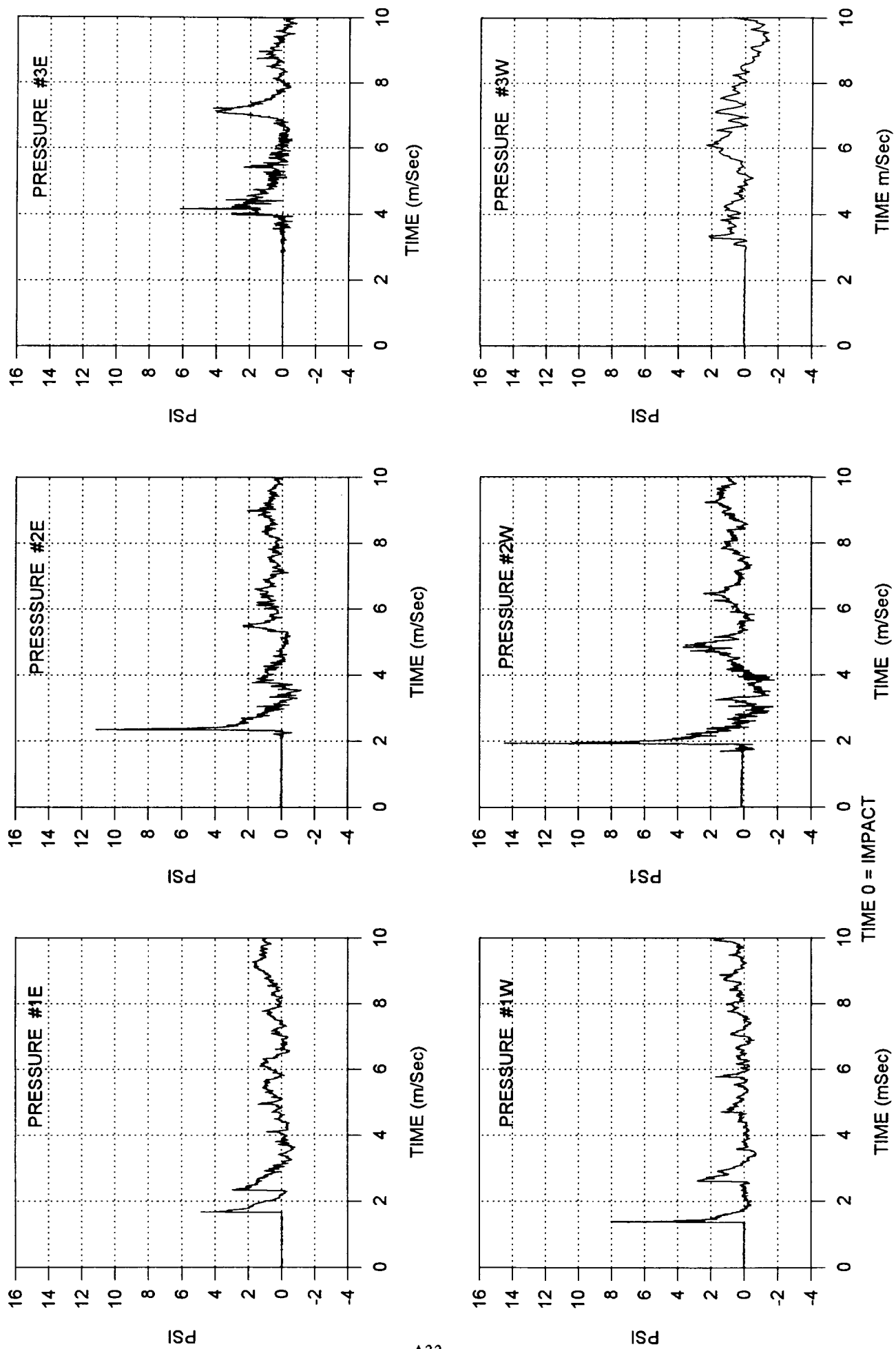


Figure A33 Pressure Profiles - Test #11

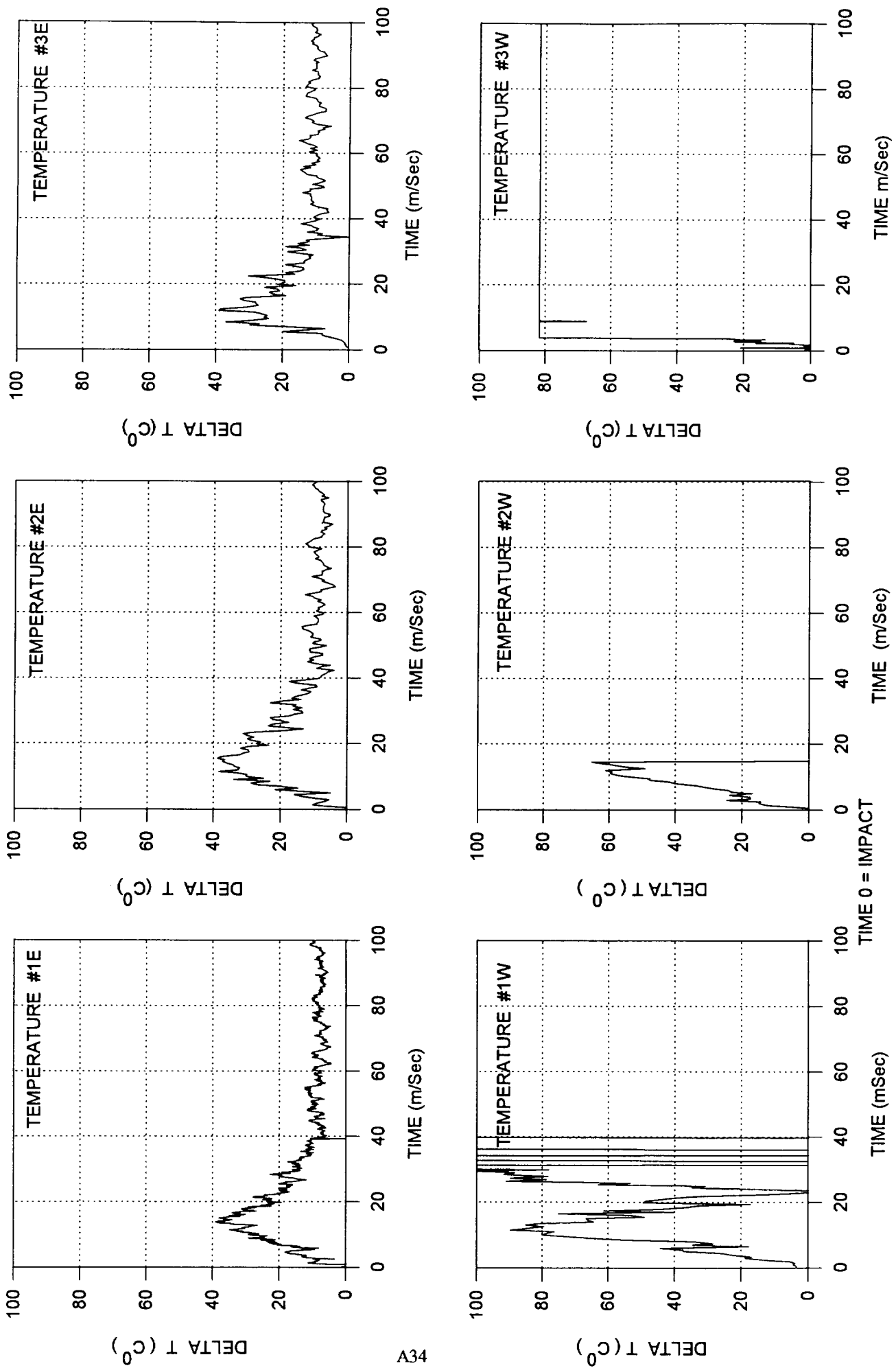


Figure A34 Temperature Profiles - Test #11

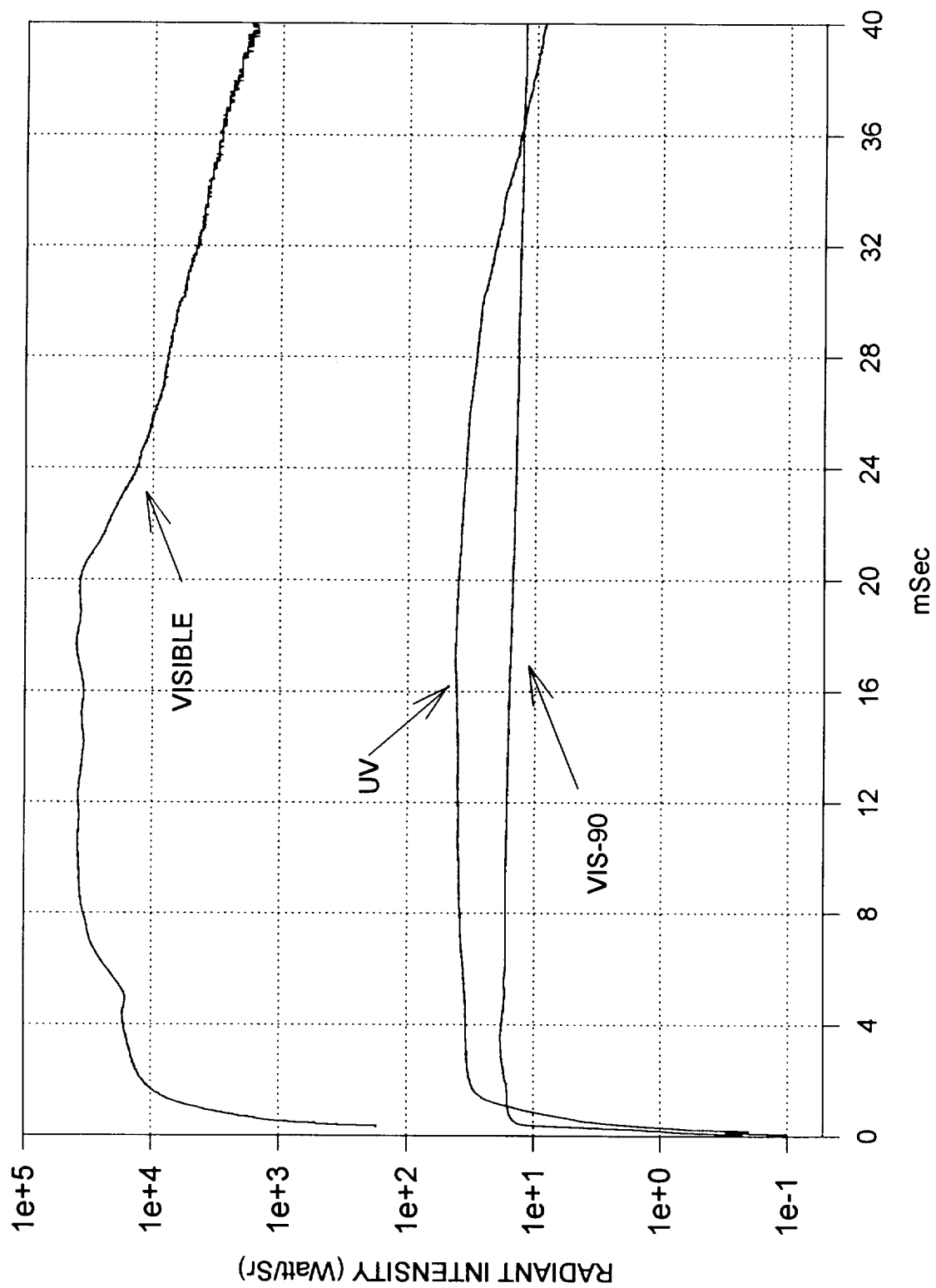
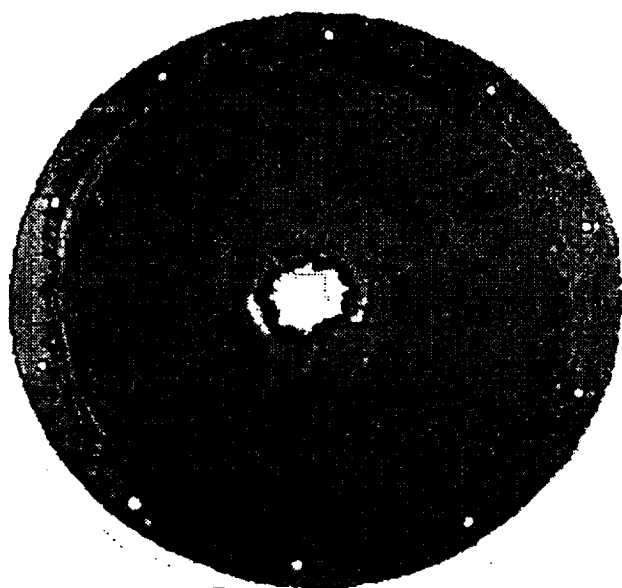


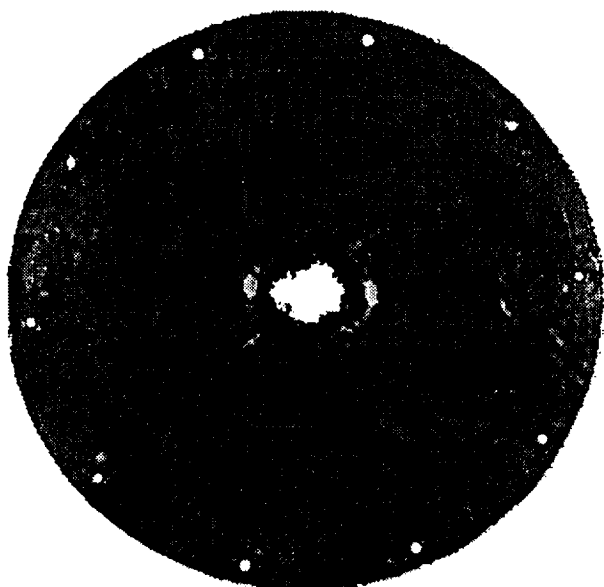
Figure A35 Radiometric Data - Test #11



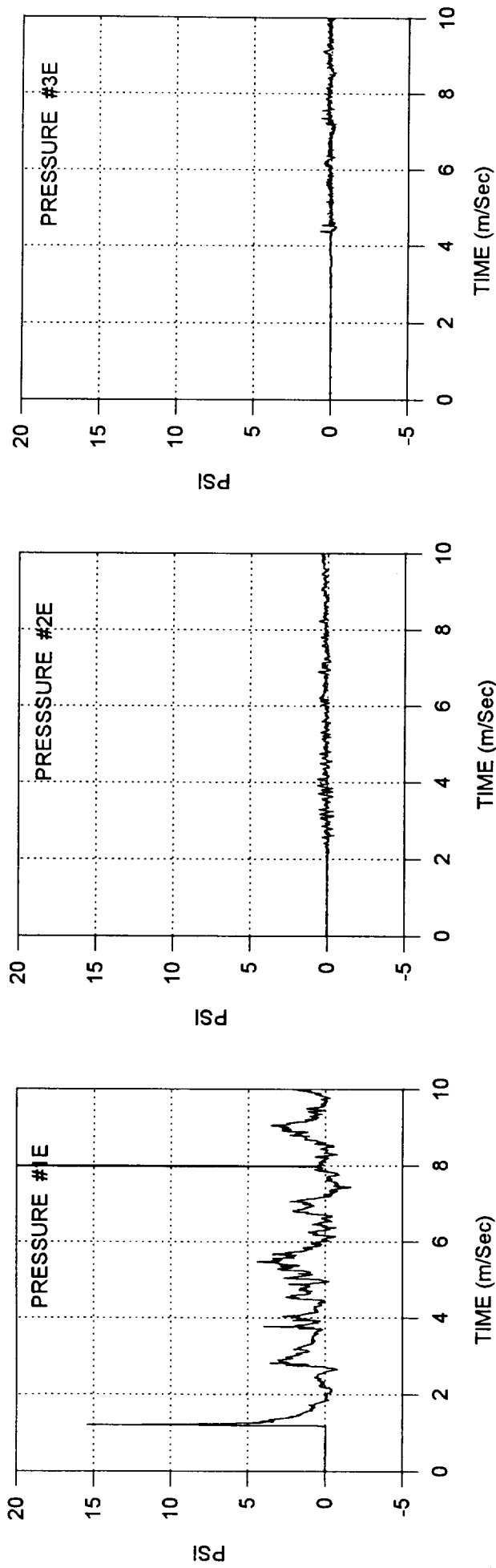
Target Plate Front



Target Plate Side



Target Plate Back



A37

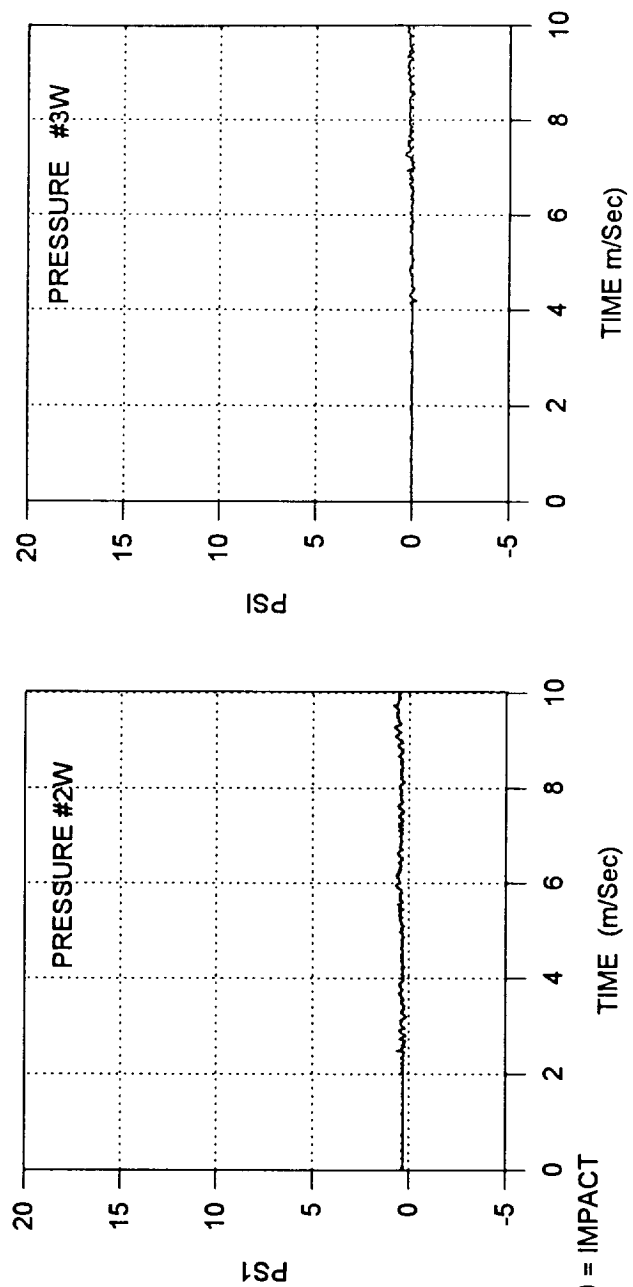
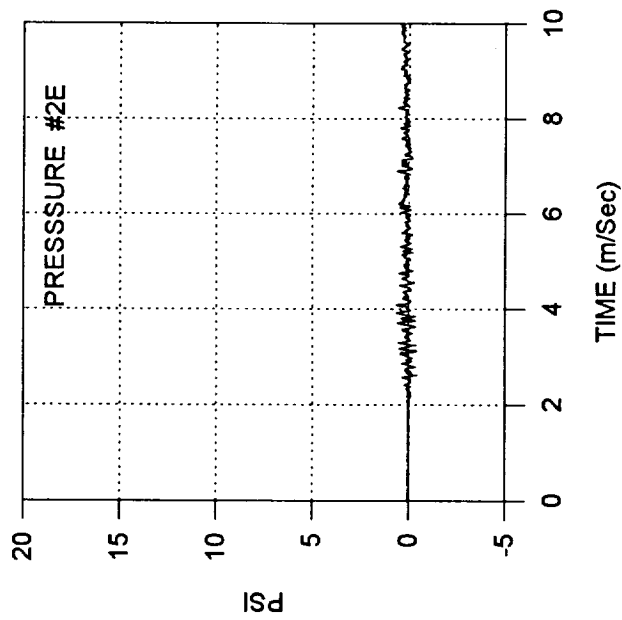
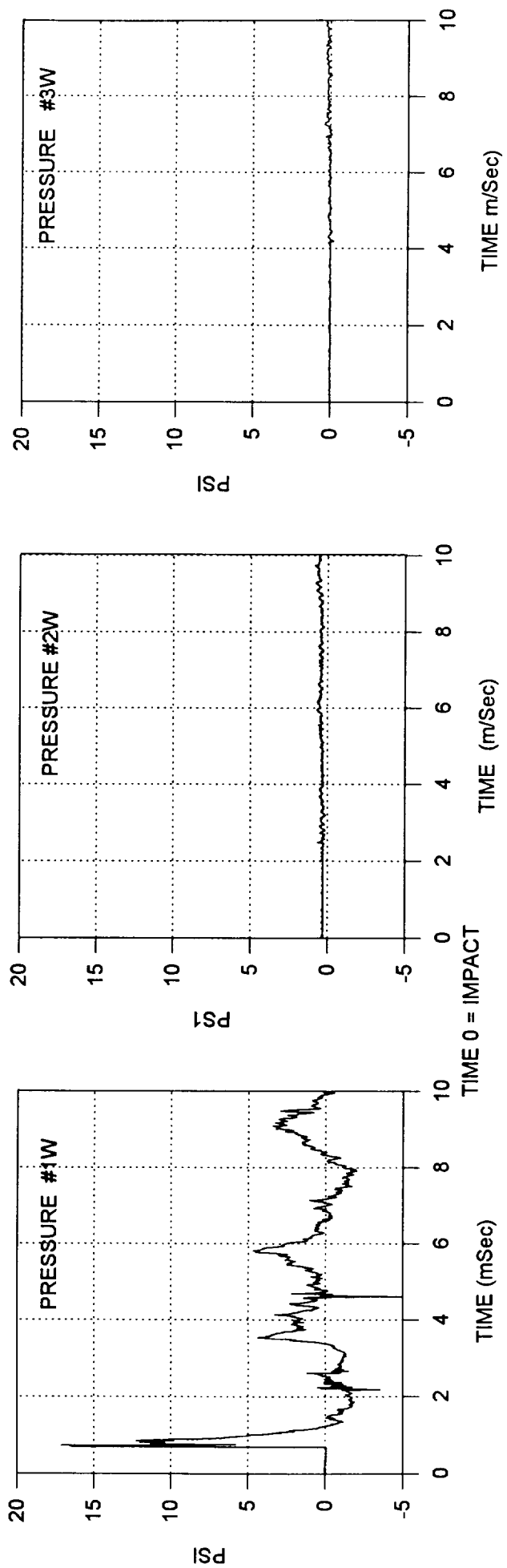


Figure A37 Pressure Profiles - Test #13

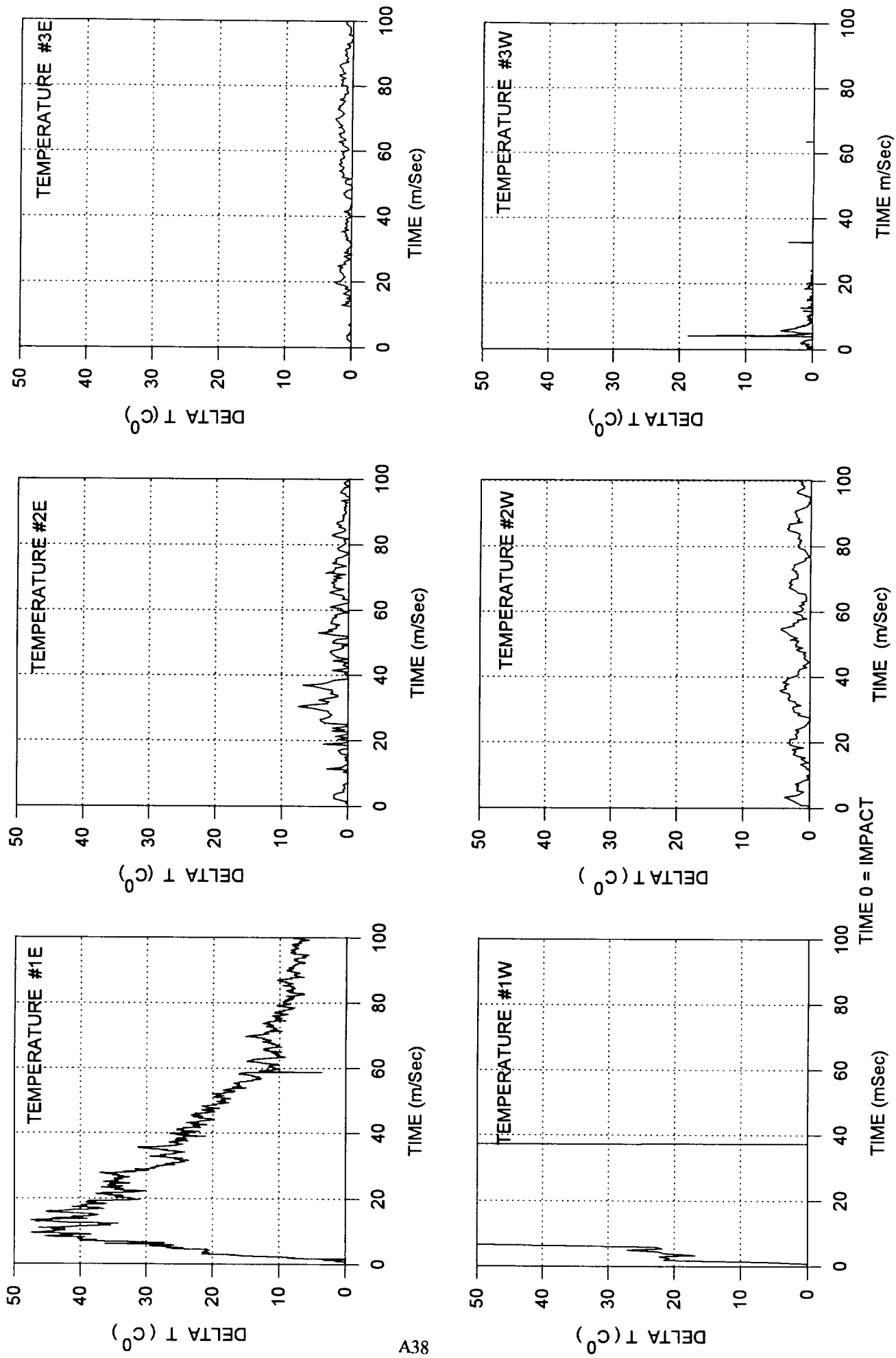


Figure A38 Temperature Profiles - Test #13

Pressure Plate Movement with Atmospheric Change

17 ghz Radar

@ Time=0 Chamber at atmosphere

@ Time=80000 uSec Chamber at 10 tor

360 Degrees = .345 inches

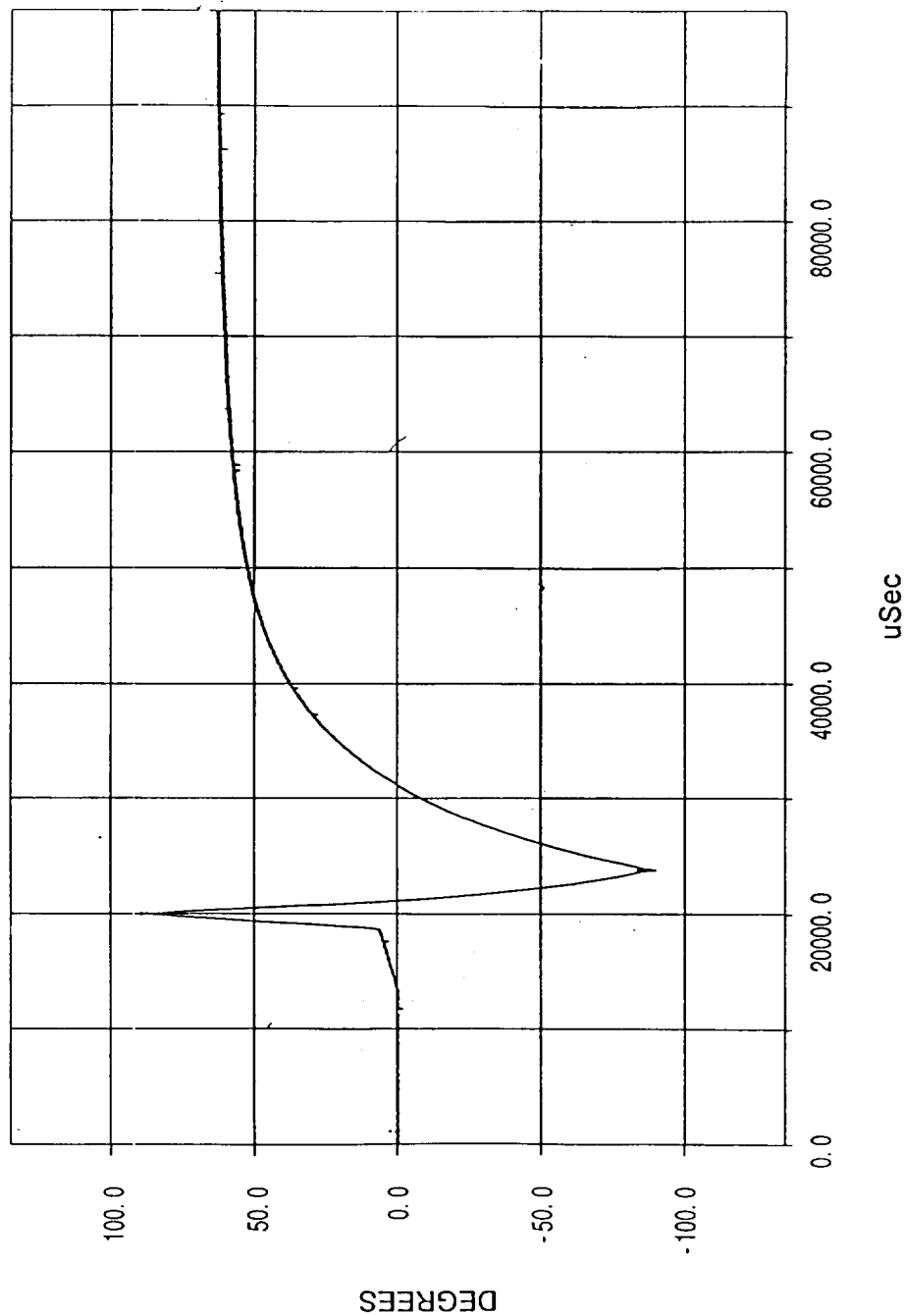
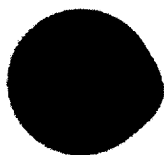


Figure A39 Pressure Plate Movement

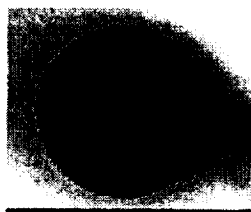
From: Calibration Negative One



extreme correction



light print

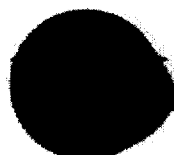


dark print

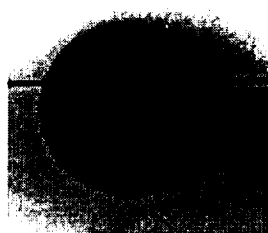
From: Calibration Negative Two



extreme correction



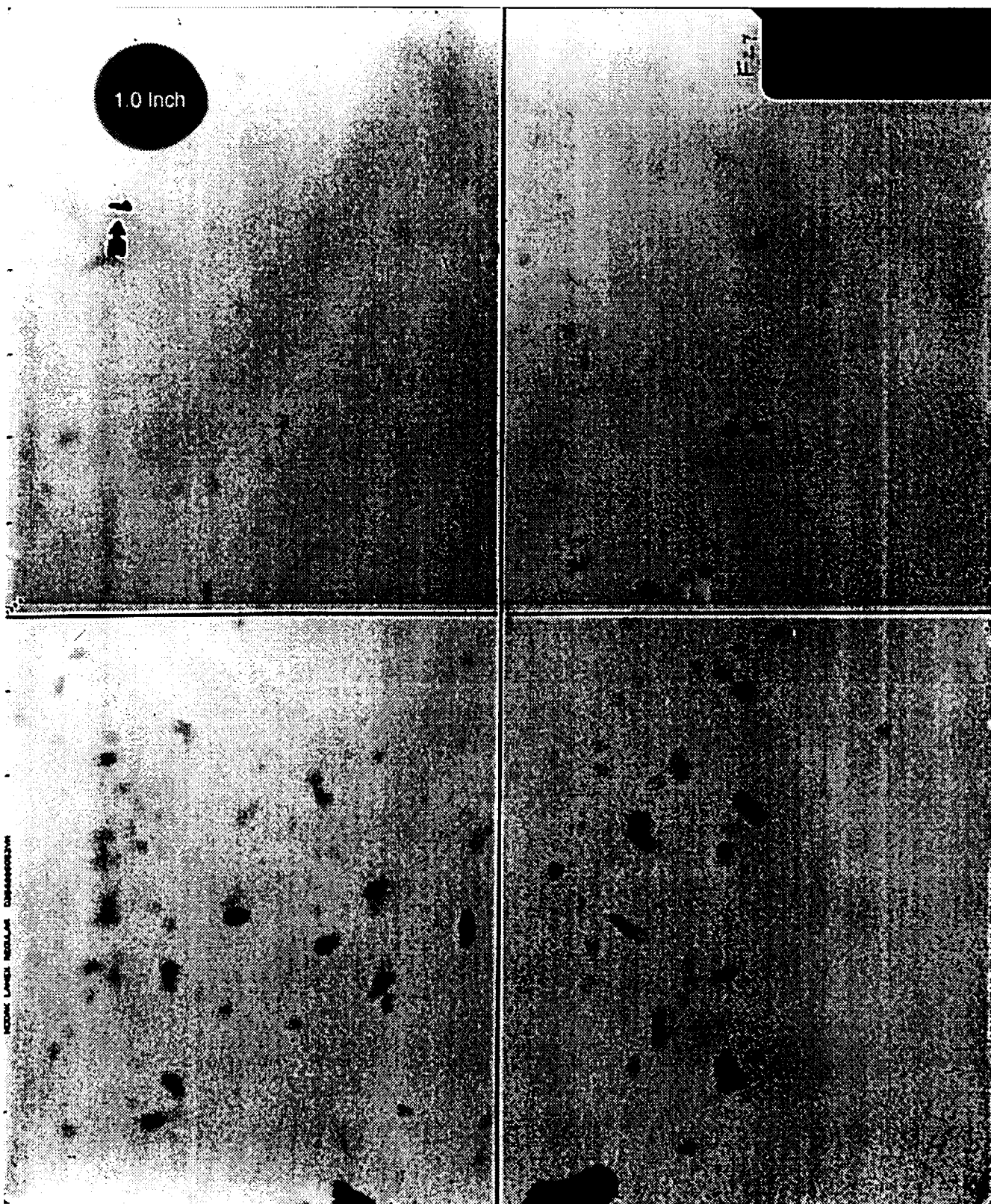
light print



dark print

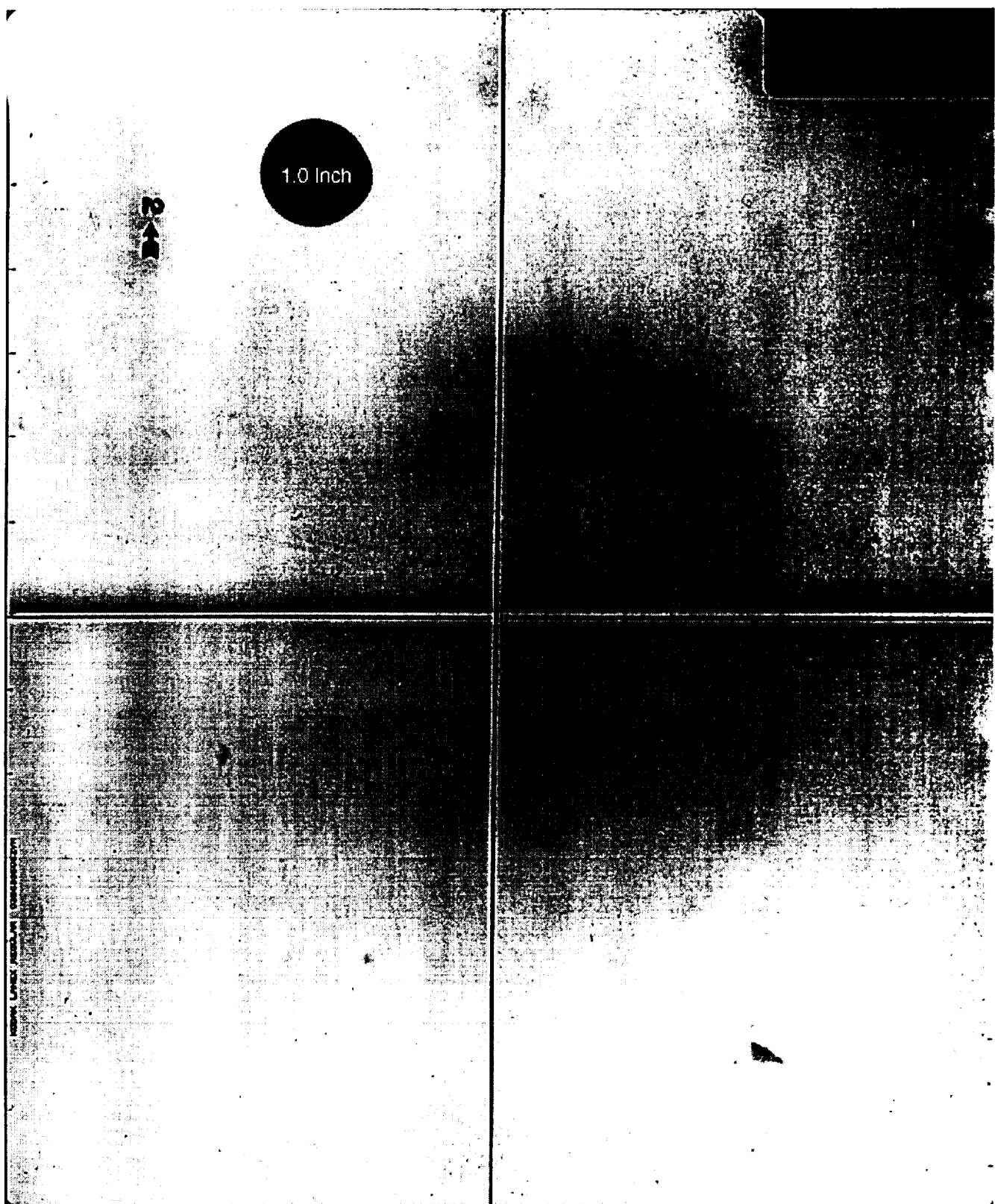
Images of a one inch calibration sphere placed in the target center.
The variation of size is due to several factors
inherent to the image manipulation process.

Figure B1 X-Ray Photograph Size Calibration



Flash X-Ray of Debris Cloud: UAH 94-26: Print One

Figure B2 X-Ray Photograph of Debris Cloud, Test # 01 X-Ray #1



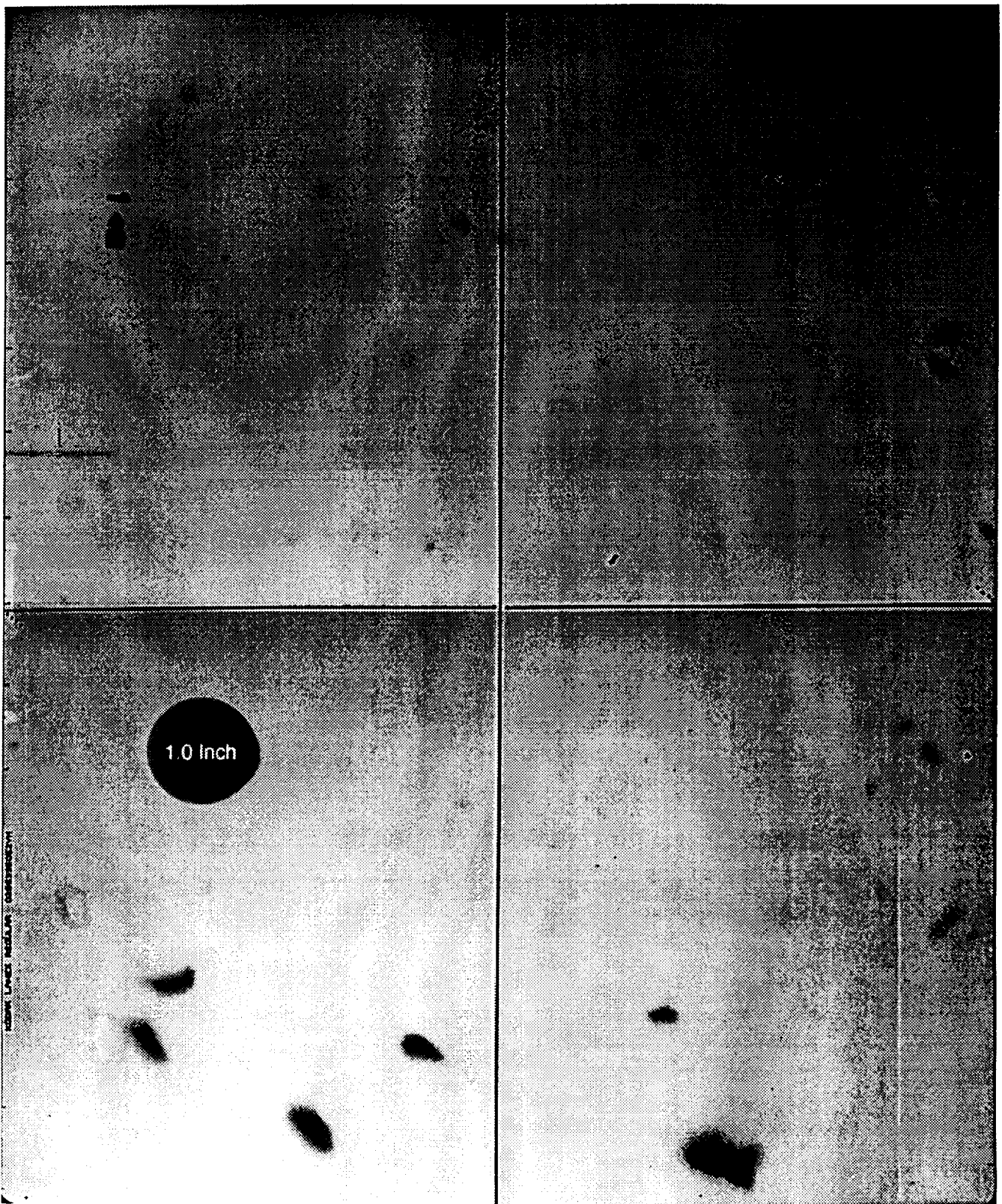
Flash X-Ray of Debris Cloud: UAH 94-26; Print Two

Figure B3 X-Ray Photograph of Debris Cloud, Test # 01 X-Ray #2



Flash X-Ray of Debris Cloud: UAH 94-30

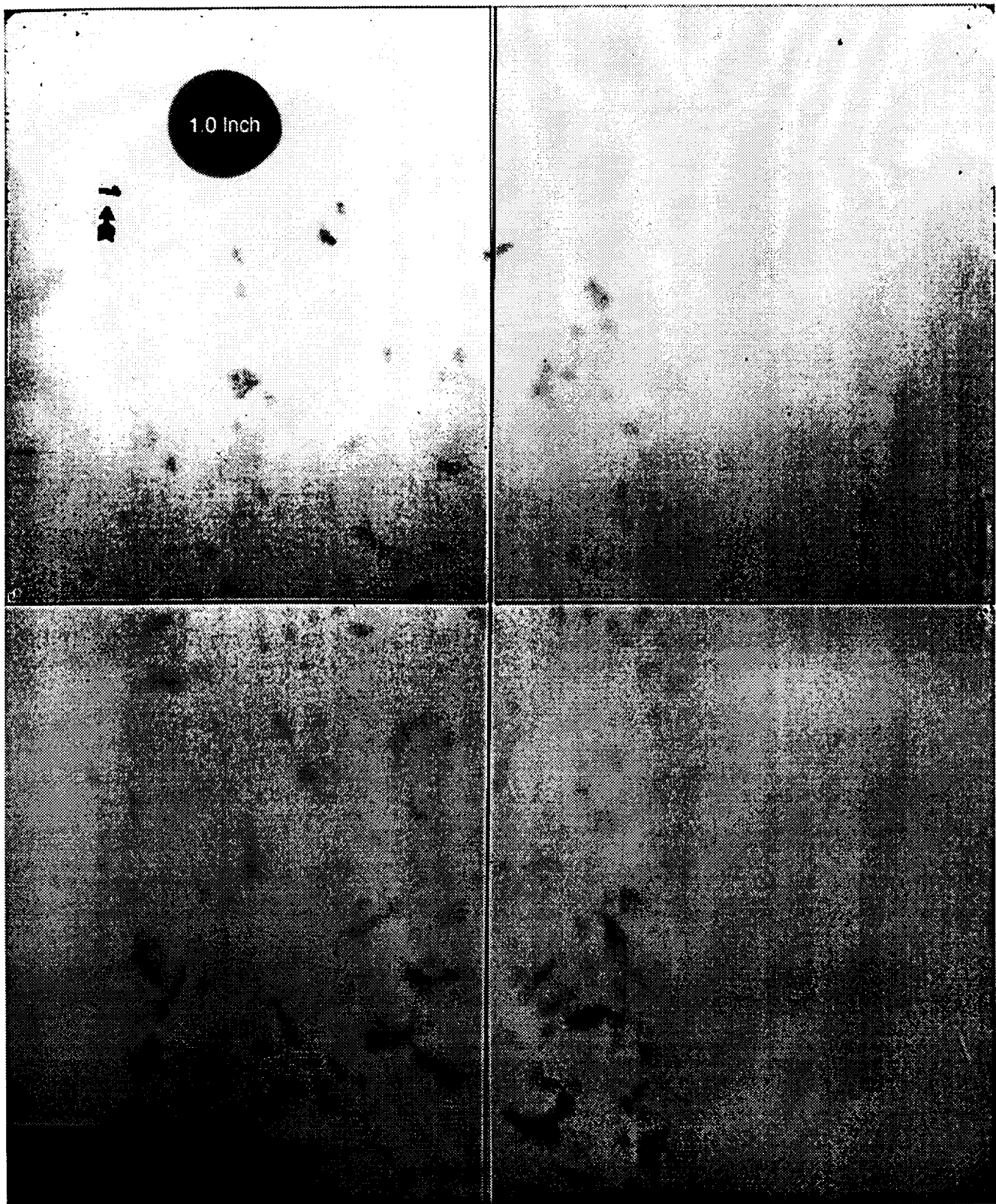
Figure B4 X-Ray Photograph of Debris Cloud, Test # 03 X-Ray #1



Flash X-Ray of Debris Cloud: UAH 94-33

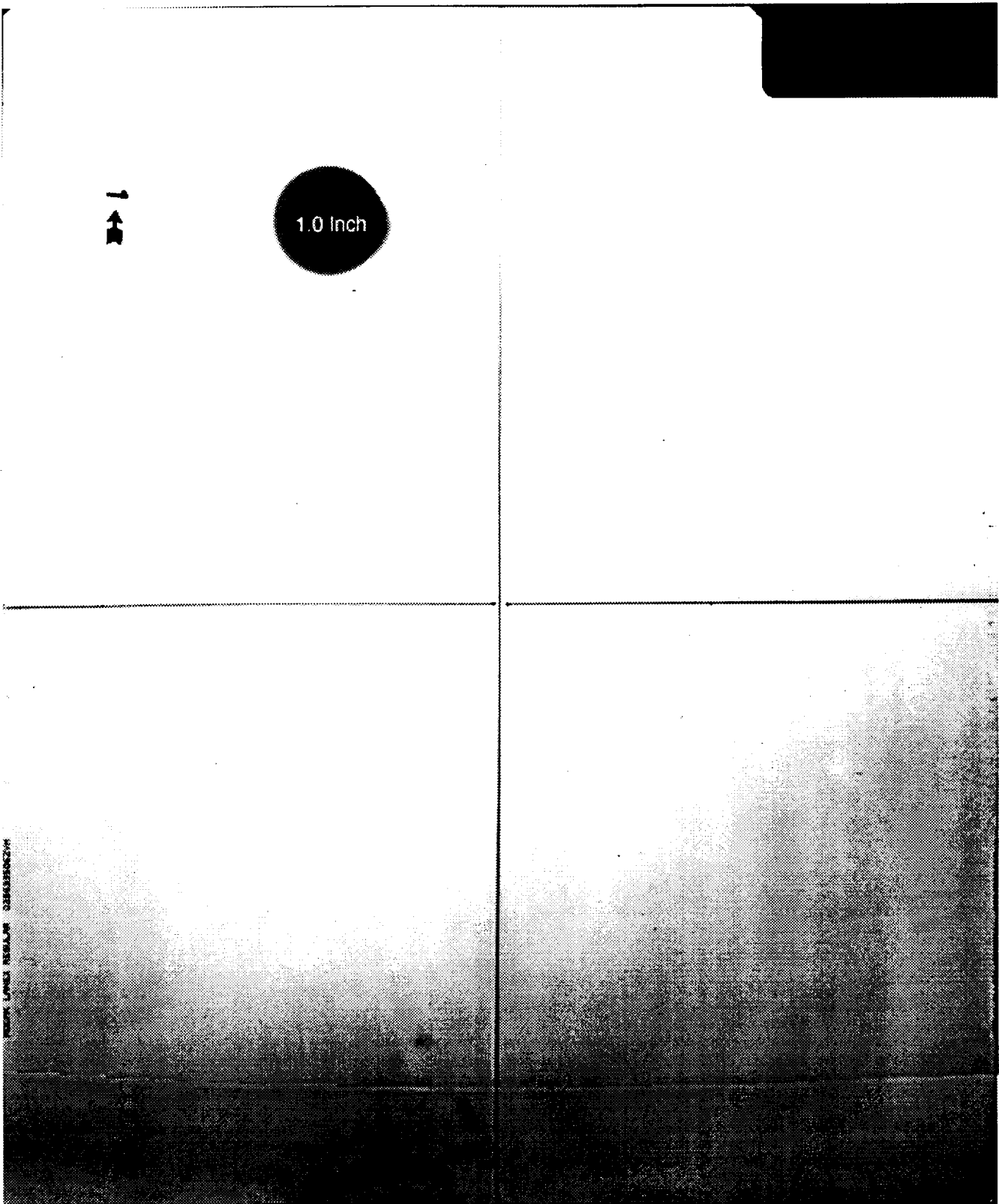
Figure B5

X-Ray Photograph of Debris Cloud, Test # 05 X-Ray #1



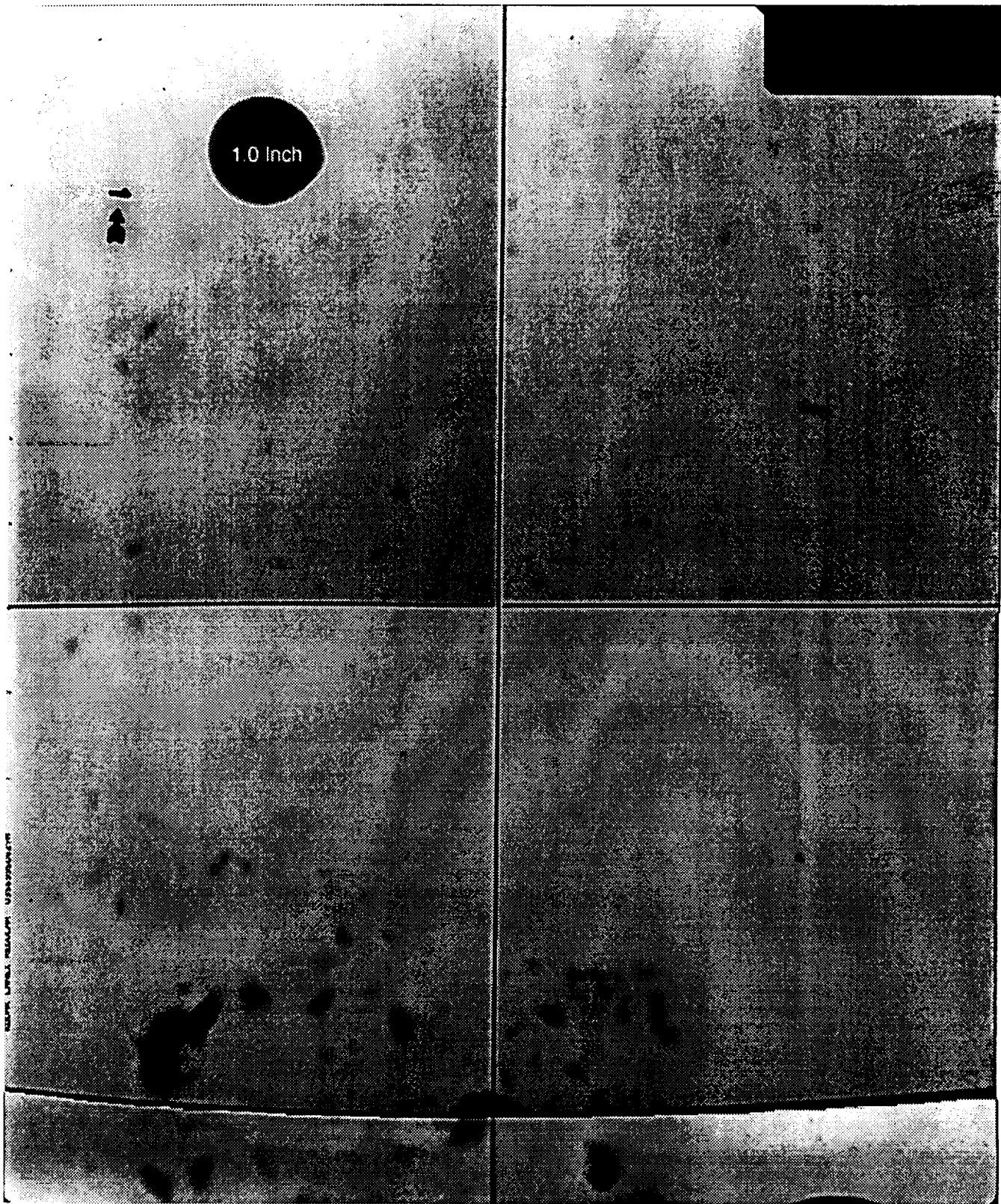
Flash X-Ray of Debris Cloud: UAH 94-42

Figure B6 X-Ray Photograph of Debris Cloud, Test # 06 X-Ray #1



Flash X-Ray of Debris Cloud: UAH 94-56

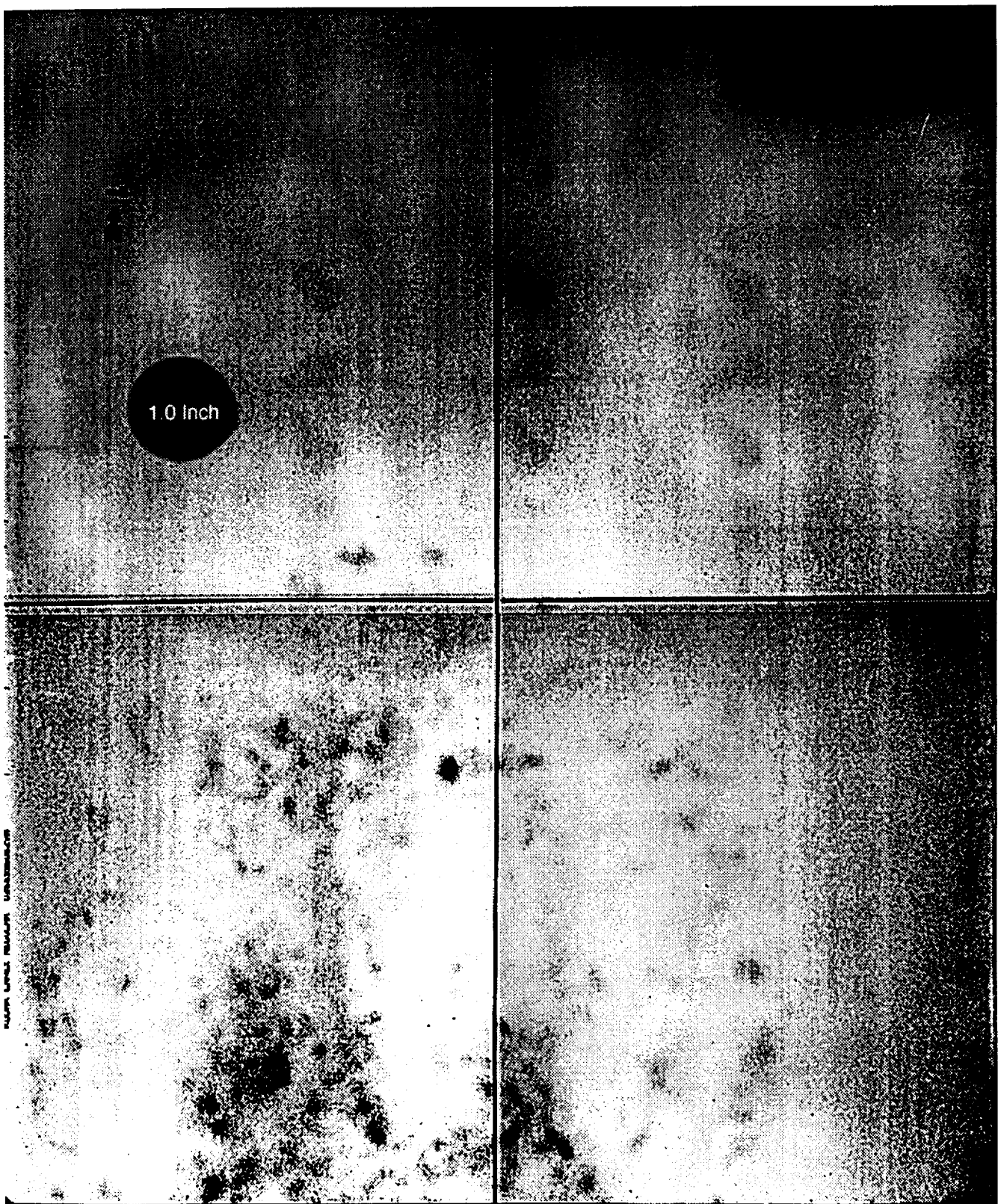
Figure B7 X-Ray Photograph of Debris Cloud, Test # 09 X-Ray #1



Flash X-Ray of Debris Cloud: UAH 94-57

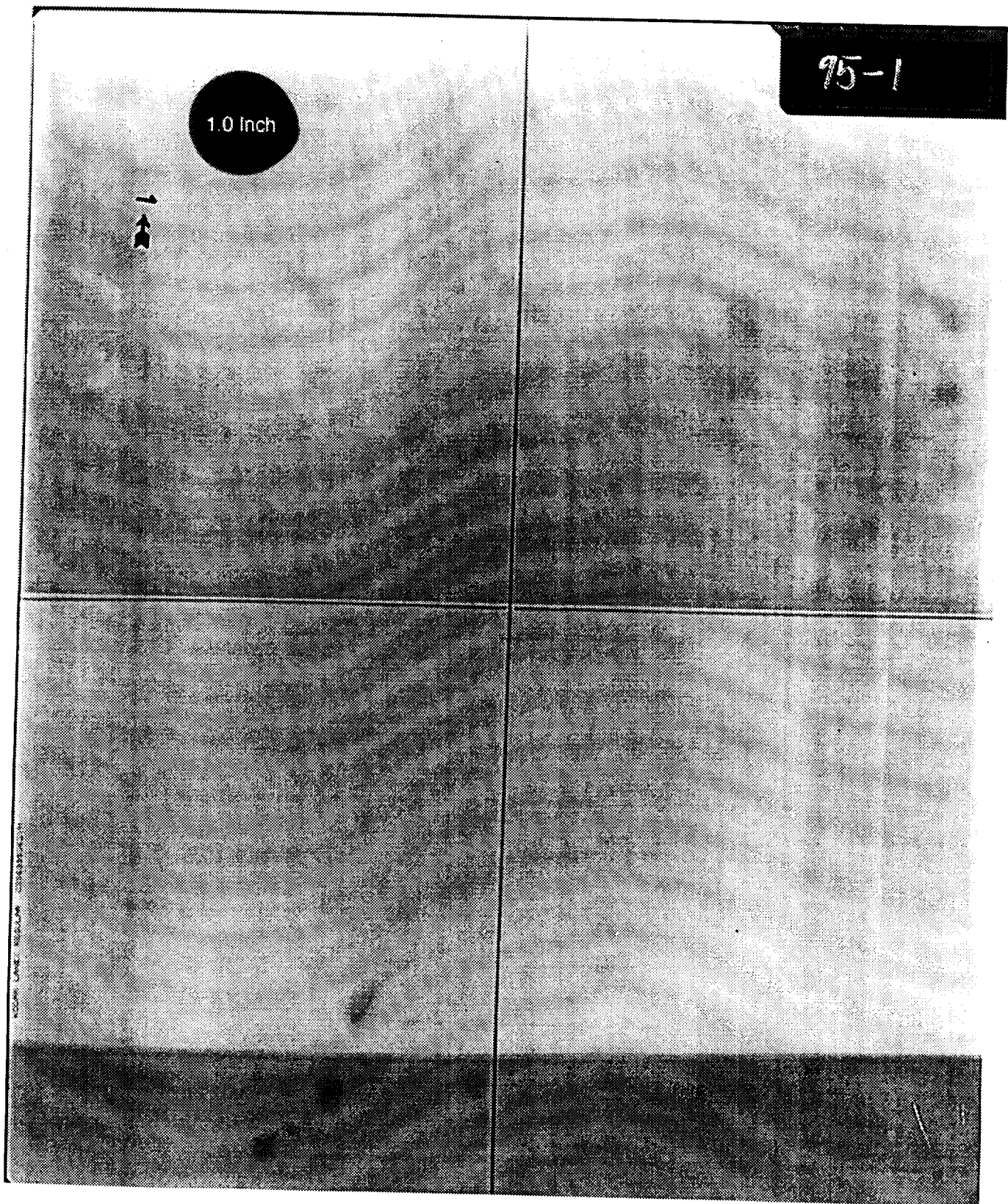
Figure B8

X-Ray Photograph of Debris Cloud, Test # 10 X-Ray #1



Flash X-Ray of Debris Cloud: UAH 94-61

Figure B9 X-Ray Photograph of Debris Cloud, Test # 11 X-Ray #1



Flash X-Ray of Debris Cloud: UAH 95-01

Figure B10 X-Ray Photograph of Debris Cloud, Test # 13 X-Ray #1

DISTRIBUTION LIST

Commander
U. S. Army Missile Command
ATTN: AMSMI-RA-EH-RM-SA (Gregory Calvert)
Redstone Arsenal, AL 35898-5340

Commander
U. S. Army Missile Command
ATTN: AMSMI-RD-ST-WF (Chuck Vessels)
Redstone Arsenal, AL 35898-5247

Deputy Commander
U. S. Army Space & Strategic Command
P.O. Box 1500
Huntsville, AL 35807-3801
ATTN: CSSD SD-M (Kathy Carpenter)

Director
U. S. Army Redstone Technical Test Center
ATTN: STERT-TE-E-EM (Jeffery D. Craven)
Redstone Arsenal, AL 35898-8052

Director
U. S. Army Redstone Technical Test Center
ATTN: STERT-TE-M-ST (Mike Liles)
Redstone Arsenal, AL 35898-8052

Hughes Missile Systems
Bldg. 805 MS M3
1151 E. Herman Road
Tucson, AZ 85734
ATTN: Leonard Vance

Lockheed Missile & Space Company
P.O. Box 070017
Huntsville, AL 35758
ATTN: S. Kursius

MIT Lincoln Laboratories
Radar Measurements Division
244 Wood Avenue
Lexington, MA 02173-0073
ATTN: Richard Spitzberg

Nichols Research Corporation
4040 Memorial Parkway, SW
Huntsville, AL 35802
ATTN: R. Herschberger

Rockwell International
Rocketdyne Division, MC EB58
6633 Canoga Avenue
Canoga Park, CA 91309-7922

Titan Corporation-CRT
5117 Johnson Drive
Pleasanton, CA 94588
ATTN: Dennis Orphal